

Studies of Halide Perovskites CsPbX_3 , RbPbX_3 ($\text{X}=\text{Cl}^-$, Br^- , I^-), and Their Solid
Solutions

Thesis

Presented in Partial Fulfillment of the Requirements for the Degree Master of Science in
the Graduate School of The Ohio State University

By

Matthew Ronald Linaburg, Bachelor of Science

Graduate Program in Chemistry

The Ohio State University

2015

Thesis Examination Committee:

Patrick M. Woodward, Advisor

Anne Co

Copyright by

Matthew Ronald Linaburg

2015

Abstract

Halide perovskites have garnered much attention in recent years as a potential material for photovoltaics, semiconductors, transparent conductors, thermistors, and electromagnetic radiation detectors. Lead halide perovskites with the formula APbX₃, where A = Cs⁺ and X = Cl⁻, Br⁻, or I⁻ have been shown to adopt a distorted perovskite structure (space group *Pnma*) with desirable band gaps and electronic properties for photovoltaic and detector applications. Experiments were conducted herein to better understand the stability limit of the lead halide perovskite structure through A-site substitution with a smaller Rb⁺ ion. Variable X-ray powder diffraction measurements were used to identify and characterize perovskite phase transitions at elevated temperatures for RbPbCl₃, RbPbBr₃, and RbPbI₃, all of which form non-perovskite compounds at room temperature. Solid solutions Rb_(x)Cs_(1-x)PbCl₃ and Rb_(x)Cs_(1-x)PbBr₃ were synthesized as a means to stabilize the high temperature perovskite phases observed in the variable temperature experiments, and to further study the effects of octahedral tilting on the band gap of the compound.

The RbPbX₃ (X = Cl⁻, Br⁻, and I⁻) phases do not form as perovskites at room temperature, but RbPbCl₃ and RbPbBr₃ undergo phase transitions to perovskite structures at higher temperature. RbPbCl₃ transitions first at 320 °C to a tetragonally distorted

perovskite structure (space group $P4/mbm$) then to the cubic perovskite structure (space group $Pm\bar{3}m$) at 340 °C. RbPbBr_3 also undergoes two phase transitions, first to an orthorhombically distorted perovskite structure (space group $Pnma$) at 250 °C then to a tetragonally distorted perovskite structure (space group $P4/mbm$) at 350 °C. Solid solutions of $\text{Rb}_{(x)}\text{Cs}_{(1-x)}\text{PbCl}_3$ and $\text{Rb}_{(x)}\text{Cs}_{(1-x)}\text{PbBr}_3$ resulted in a orthorhombic perovskite structure (space group $Pnma$) at room temperature. The orthorhombic distortion increased as the Rb^+ content increased, due to increased tilting of the lead-centered octahedra. For the Cl^- solid solution, the perovskite structure was retained for Rb^+ substitution up to a value of $x = 0.9$, while for the Br^- solid solutions a perovskite structure could be obtained up to $x = 0.6$. As the Rb^+ substitution increases, the band gap of the compound increases. The band gap of the $\text{Rb}_{(x)}\text{Cs}_{(1-x)}\text{PbCl}_3$ ($x = 0 - 0.6$) solid solution increases from 2.97 eV to 3.08 eV, while the $\text{Rb}_{(x)}\text{Cs}_{(1-x)}\text{PbBr}_3$ solid solutions increases from 2.13 eV to 2.30 eV across the same $x = 0 - 0.6$ range. The increase is a result of greater octahedral distortions, which were characterized by measuring the $\text{Pb}-\text{X}-\text{Pb}$ bond angles.

Dedication

Dedicated to my family, friends, and students at The Ohio State University

Acknowledgements

I would first and foremost like to thank my brilliant advisor, Dr. Patrick Woodward. Never have I had the pleasure of working with someone who would so willingly stop what they were doing to answer a question or to help with a problem. His kindness is only matched by his patience, which I am sure I tested by knocking on his office door on multiple stressed out occasions. I truly cannot thank him enough for the time that he has selflessly given me, whether it be discussing projects, science, or my future.

I would also like to thank my current and former group members Jie Xiong, Ryan Morrow, Eric McClure, Drew Adkins, Phoung Tran, Jackson Majher, David Merz, Andrew Shartis, Spencer Porter, and Alejandra Morales. During my first year in lab Andrew, Jie, Spencer, and Ryan would willingly share with me their knowledge of solid-state synthesis, gloveboxes, XRD, refinement programs, and general knowledge of how things get done in the chemistry department; it was the kindness of these individuals that allowed me to adapt to the lab and solid-state atmosphere. I would also like to thank Eric for always being there to talk science, eat food, get beers, and for being a wall for me to bounce ideas off of.

Finally, I would like to thank my girlfriend of 5 years, Laura DeGeer. Her support of me through this entire process has been unwavering. There were many months of little sleep, short tempers, and lots and lots of stress but she was always right there believing in me when I did not. She truly prevented mental breakdowns on multiple occasions and I am blessed to have her in my life.

Vita

2004 – 2009 Mt. Lebanon High school
2009 – 2013 B.S. Chemistry, Syracuse University
2013 – 2015 M.S. Inorganic Chemistry Graduate
Research Student, The Ohio State
University

Publications

Adhikari, A. a.; Shah, J. P.; Howard, K. T.; Russo, C. M.; Wallach, D. R.; Linaburg, M.R.; Chisholm, J. D. Convenient Formation of Diphenylmethyl Esters Using Diphenylmethyl Trichloroacetimidate. *Synlett* **2014**, 25 (2), 283–287.

Field of Study

Major Field: Chemistry

Table of Contents

Abstract.....	ii
Acknowledgements.....	v
Vita.....	vii
Field of Study.....	vii
List of Tables	xi
List of Figures.....	xiii
List of Symbols.....	xviii
Chapter 1	1
Introduction.....	1
1.1 General Motivation	1
1.2 The Perovskite Structure	2
1.3 Glazer Notation and Perovskite Tilt Systems	4
1.4 Tolerance Factor.....	9
Chapter 2	11

Variable Temperature Studies of RbPbX₃ (X = Br⁻, Cl⁻, and I⁻)	11
2.1 Introduction.....	11
2.1.1 <i>Review of Relevant Literature</i>	12
2.2 Experimental Section	16
2.2.1 <i>Characterization</i>	17
2.3 Results	18
2.3.1 <i>The structure of CsPbCl₃</i>	18
2.3.2 <i>RbPbCl₃</i>	22
2.3.3 <i>RbPbBr₃</i>	31
2.3.4 <i>RbPbI₃</i>	43
2.3.5 <i>Compound Colors</i>	44
2.4 Discussion	46
Chapter 3	53
Driving Octahedral Tilting in the Perovskite Structure Through A-site Substitution	
Using Solid Solutions Rb_(y)Cs_(1-y)PbX₃ (X = Cl⁻,Br⁻).....	53
3.1 Introduction	53
3.2 Experimental Section	54
3.3 Results	56
3.3.1 <i>Moisture Sensitivity of solid solutions with high Rb⁺ ratios.</i> 56	
3.3.2 <i>Pnma (a⁻b⁺a⁻) symmetry perovskites from solid solutions..</i> 57	
3.3.3 <i>Octahedral tilting with increased Rb⁺ substitution</i> 64	
3.3.4 <i>Pb-X-Pb (X = Cl⁻ and Br⁻) bond angles</i> 67	

3.3.5 Band gaps of Rb_(x)Cs_(1-x)PbX₃ compounds (X = Cl⁻ and Br⁻) 69

3.4 Discussion	74
3.5 Conclusion	80
Bibliography	83

List of Tables

	Page
Table 2.1: Refined structural information for room temp orthorhombic CsPbCl ₃	20
Table 2.2: Refined lattice parameters for room temp Rb ₆ Pb ₅ Cl ₁₆	25
Table 2.3: Refined lattice parameters and structural information for room temp RbPb ₂ Cl ₅	25
Table 2.4: Refined lattice parameters and structural information for high temp tetragonal phase RbPbCl ₃	27
Table 2.5: Refined lattice parameters and structural information for high temp cubic phase RbPbCl ₃	30
Table 2.6: Refined lattice parameters and structural information for room temp non-perovskite RbPbBr ₃	35
Table 2.7: Refined lattice parameters and structural information for RbPb ₂ Br ₅ 50°C.....	36
Table 2.8: Refined lattice parameters and structural information for high temp orthorhombic perovskite phase RbPbBr ₃	39
Table 2.9: Refined lattice parameters and structural information for high temp tetragonal perovskite phase RbPbBr ₃	42
Table 3.1: Refined structural information and lattice parameters for room temp orthorhombic Rb ₆ Cs ₄ PbCl ₃	59
Table 3.2: Refined structural information and lattice parameters for room temperature orthorhombic Rb ₄ Cs ₆ PbBr ₃	60

Table 3.3:	Derived band gaps using the Tauc method for $\text{Rb}_{(x)}\text{Cs}_{(1-x)}\text{PbCl}_3$ solid solution.....	72
Table 3.4:	Derived band gaps using the Tauc method for $\text{Rb}_{(x)}\text{Cs}_{(1-x)}\text{PbBr}_3$ solid solutions.....	74
Table 3.5:	Band gaps and bond angles for $X=0$ and $X=0.6$, Cl^- and Br^- solid solutions compared to the same properties of similar perovskite structures with different formulas. (t) is absent for the methyl ammonium perovskites as an accurate value cannot be obtained due to the organic A-site cation.....	77

List of Figures

	Page
Figure 1.1: Ideal Perovskite Structure space group $Pm\bar{3}m$ (left). Expanded view illustrating the corner sharing octahedral network (right)	3
Figure 1.2: Schematic diagram indicating the group-subgroup relationships among the 15 space groups tabulated by Howard and Stokes. Dashed lines connecting a group with its subgroup indicates that the corresponding phase transition is required by Landau theory to be first order. ¹	5
Figure 1.3: Examples of perovskite octahedral tilting from lower to higher symmetry space groups, with subsequent Glazer notation for associated tilt.....	6
Figure 1.4: Pattern of peak splitting observed in the tetragonal distorted perovskite with the tilt system $a^0a^0c^+$. Ideal cubic perovskite reflections split in a characteristic manner when the perovskites octahedra become distorted. Distorted structures were modeled on the Crystal Maker program using $CsPbBr_3$	7
Figure 1.5: Peak splitting from the ideal perovskite reflections are observed for the distorted orthorhombic perovskite structure with tilt system $a^-b^+a^-$. Ideal cubic perovskite reflections split in a characteristic manner when the perovskites octahedra become distorted. Distorted structures were modeled on the Crystal Maker program using $CsPbBr_3$	8
Figure 2.1: Phase diagram of $RbCl/ PbCl_2$. Taken from ref 17.....	14
Figure 2.2: Refined synchrotron diffractogram of $CsPbCl_3$ obtained from the 11-BM beamline at APS.....	19
Figure 2.3: Select 2θ range to illustrate superstructure reflections. Labeled hkl reflections correspond to the observed reflections on a $2a_p \times 2a_p \times 2a_p$ cell.....	19

Figure 2.4:	Rietveld refined XRD of RbPbCl ₃ at room temperature showing the two phase mixture. Markers at the bottom (green) correspond to RbPb ₂ Cl ₅ <i>P2₁/c</i> symmetry. Top markers (blue) correspond to Rb ₆ Pb ₅ Cl ₁₆ <i>P4/mbm</i> symmetry.....	23
Figure 2.5:	Select variable temperature diffraction patterns for RbPbCl ₃ . Numbers correspond to phases present at that temperature. 1 = Rb ₆ Pb ₅ Cl ₁₆ , 2 = RbPb ₂ Cl ₅ , 3 = RbPbCl ₃ with tetragonal symmetry (space group <i>P4/mbm</i>), 4 = RbPbCl ₃ with cubic symmetry (space group <i>Pm</i> $\bar{3}m$). Black <i>hkl</i> ticks illustrate reflections from phase 2 (RT) and phase 3 (310 °C)	24
Figure 2.6:	The structures of Rb ₆ Pb ₅ Cl ₁₆ (left) and RbPb ₂ Cl ₅ (right). The Cl ⁻ , Pb ²⁺ , and Rb ⁺ ions are represented with green, gray, and magenta spheres, respectively.....	26
Figure 2.7:	Rietveld refined XRD of tetragonal perovskite RbPbCl ₃ at 320 °C. Blue markers correspond to RbPbCl ₃ perovskite with <i>P4/mbm</i> symmetry. Green markers correspond to RbPb ₂ Cl ₅ <i>P2₁/c</i> symmetry. Purple markers correspond to Rb ₆ Pb ₅ Cl ₁₆ <i>P4/mbm</i> symmetry.....	27
Figure 2.8:	The structure of tetragonal RbPbCl ₃ <i>P4/mbm</i> orientated down the crystallographic c-axis (left) and b-axis (right). The Cl ⁻ , Pb ²⁺ , and Rb ⁺ ions are represented with green, gray, and magenta spheres, respectively.....	28
Figure 2.9:	Rietveld refined XRD of tetragonal perovskite RbPbCl ₃ at 350 °C. Blue markers correspond to RbPbCl ₃ perovskite with <i>Pm</i> $\bar{3}m$ symmetry..	29
Figure 2.10:	Structure of high temperature cubic perovskite (space group <i>Pm</i> $\bar{3}m) RbPbCl3. The Cl-, Pb2+, and Rb+ ions are represented with green, gray, and magenta spheres, respectively.....$	30
Figure 2.11:	Select variable temperature diffractograms of RbPbBr ₃ . Numbers correspond to phases present at that temperature. 1 = RbPbBr ₃ non-perovskite with NH ₄ CdCl ₃ structure (space group <i>Pnma</i>), 2 = RbPb ₂ Br ₅ , 3 = RbPbBr ₃ distorted perovskite with orthorhombic symmetry (space group <i>Pnma</i>), 4 = RbPbBr ₃ distorted perovskite with tetragonal symmetry (space group <i>P4/mbm</i>).....	32

Figure 2.12: Rietveld refined XRD of RbPbBr_3 at room temperature showing the two phase mixture. Markers at the bottom (green) correspond to RbPb_2Br_5 . Top markers (blue) correspond to RbPbBr_3 with the NH_4CdCl_3 structure.....	34
Figure 2.13: Orthorhombic non-perovskite RbPbBr_3 with Pnma symmetry. The Br^- , Pb^{2+} , and Rb^+ ions are represented with brown, gray, and magenta spheres, respectively.....	35
Figure 2.14: Structure of room temperature RbPb_2Br_5 non-perovskite tetragonal phase (space group $P4/mbm$). The Br^- , Pb^{2+} , and Rb^+ ions are represented with brown, gray, and magenta spheres, respectively.....	37
Figure 2.15: Rietveld refined XRD of tetragonal perovskite RbPbBr_3 at 260 °C. Blue markers correspond to RbPbBr_3 perovskite with Pnma symmetry. Green markers (bottom) correspond to RbPb_2Br_5 with $I4/mcm$ symmetry.....	39
Figure 2.16: Structure of high temperature orthorhombic distorted perovskite RbPbBr_3 (space group Pnma). The Br^- , Pb^{2+} , and Rb^+ ions are represented with brown, gray, and magenta spheres, respectively.....	40
Figure 2.17: Rietveld refined XRD of tetragonal perovskite RbPbBr_3 at 350 °C. Blue markers correspond to RbPbBr_3 perovskite with $P4/mbm$ symmetry.....	41
Figure 2.18: Structure of high temperature tetragonal distorted perovskite RbPbBr_3 (space group $P4/mbm$). The Br^- , Pb^{2+} , and Rb^+ ions are represented with brown, gray, and magenta spheres, respectively.....	42
Figure 2.19: Collected diffractograms from the RbPbI_3 variable temperature experiment.....	43
Figure 2.20: Observed colors at room and high temperature for halide compounds, which exist as a non-perovskite at room temperature and transition to a perovskite at high temperature. RbPbI_3 shows no phase transition.....	45
Figure 2.21: Temperature vs. Tolerance factor for compounds CsPbX_3 and RbPbX_3 ($\text{X}=\text{Cl}^-$, Br^- , I^-).....	46
Figure 2.22: Branching of the lattice parameters for RbPbCl_3 ; observed as a function of temperature.....	49

Figure 2.23:	Branching of the perovskite lattice parameters for RbPbBr_3 as a function of temperature. Points at 350 °C correspond to distorted perovskite (space group $P4/\text{mbm}$) while all other points correspond to the distorted perovskite (space group $Pnma$).....	51
Figure 3.1:	Rietveld refined XRD of the room temperature perovskite $\text{Rb}_{0.6}\text{Cs}_{0.4}\text{PbCl}_3$. Bottom tick marks correspond to the orthorhombic distorted perovskite phase, space group $Pnma$ ($a^-b^+a^-$).....	58
Figure 3.2:	Rietveld refined XRD of the room temperature perovskite $\text{Rb}_{0.6}\text{Cs}_{0.4}\text{PbBr}_3$. Bottom tick marks correspond to the orthorhombic distorted perovskite phase, space group $Pnma$ ($a^-b^+a^-$).....	59
Figure 3.3:	Cell volume vs. solid solution for $\text{Rb}_{(x)}\text{Cs}_{(1-x)}\text{PbCl}_3$ (left) and $\text{Rb}_{(x)}\text{Cs}_{(1-x)}\text{PbBr}_3$ (right). Error bars are too small to be observed on the graphs.....	61
Figure 3.4:	Pseudocubic lattice parameters vs. tolerance factor (t) for $\text{Rb}_x\text{Cs}_{(1-x)}\text{PbCl}_3$ $x = 0$ to 0.9 in 0.1 intervals.....	62
Figure 3.5:	Pseudocubic lattice parameters vs. tolerance factor (t) for $\text{Rb}_x\text{Cs}_{(1-x)}\text{PbBr}_3$ $x = 0$ to 0.6 in 0.1 intervals.....	63
Figure 3.6:	X-ray powder diffraction patterns of samples in the $\text{Rb}_{(x)}\text{Cs}_{(1-x)}\text{PbCl}_3$ solid solution. The green markers indicate the reflection positions for the $x=0.8$ phase.....	64
Figure 3.7:	Select 20 ranges from $\text{Rb}_{(x)}\text{Cs}_{(1-x)}\text{PbCl}_3$ diffraction patterns to better illustrate octahedral tilting and subsequent peak splitting as the Rb^+ content increases.....	65
Figure 3.8:	X-ray powder diffraction patterns of samples in the $\text{Rb}_{(x)}\text{Cs}_{(1-x)}\text{PbBr}_3$ solid solution. The green markers indicate the reflection positions for the $x = 0.6$ phase.....	65
Figure 3.9:	Select 20 ranges from $\text{Rb}_{(x)}\text{Cs}_{(1-x)}\text{PbBr}_3$ diffraction patterns to better illustrate octahedral tilting and subsequent peak splitting as the amount of Rb^+ is increased.....	66
Figure 3.10:	Average bond angle vs. Tolerance factor for $\text{Rb}_{(x)}\text{Cs}_{(1-x)}\text{PbX}_3$ ($\text{X} = \text{Cl}^-$ and Br^-) solid solution. $x = 0$ to 0.9 for Cl^- and $x = 0$ to 0.6 for Br^- Some error bars are smaller than symbols.....	68

Figure 3.11: Average Pb–X bond distance vs. Tolerance factor for $\text{Rb}_{(x)}\text{Cs}_{(1-x)}\text{PbX}_3$ ($X = \text{Cl}^-$ and Br^-) solid solution. $x = 0$ to 0.9 for Cl^- and $x = 0$ to 0.6 for Br^- . Some error bars are smaller than symbols.....	68
Figure 3.12: Diffuse reflectance overlay for the $\text{Rb}_{(x)}\text{Cs}_{(1-x)}\text{PbCl}_3$ series.....	71
Figure 3.13: $\text{Rb}_{(x)}\text{Cs}_{(1-x)}\text{PbCl}_3$ Tauc Plot. Diffuse reflectance data for the solid solution Cl^- series treated with the Tauc method. A linear fit was applied and extrapolated to the x -axis to elucidate the compounds band gap.....	71
Figure 3.14: Diffuse reflectance overlay for the $\text{Rb}_{(x)}\text{Cs}_{(1-x)}\text{PbBr}_3$ series.....	73
Figure 3.15: $\text{Rb}_{(x)}\text{Cs}_{(1-x)}\text{PbBr}_3$ Tauc Plot. Diffuse reflectance data for the solid solution Br^- series treated with the Tauc method. A linear fit was applied and extrapolated to the x -axis to elucidate the compounds band gap.....	73
Figure 3.16: Structural representations of the crystal structures of select $\text{Rb}_{(x)}\text{Cs}_{(1-x)}\text{PbCl}_3$ solid solutions to illustrate increased octahedral distortion with increased Rb^+ substitution.....	75
Figure 3.17: Structural representations of the crystal structures of select $\text{Rb}_{(x)}\text{Cs}_{(1-x)}\text{PbBr}_3$ solid solutions to illustrate increased octahedral distortion with increased Rb^+ substitution.....	76
Figure 3.18: Temperature vs. Tolerance factor for compounds CsPbX_3 and RbPbX_3 ($X = \text{Cl}^-, \text{Br}^-, \Gamma$). Markers were added for all of the room temperature perovskites formed from solid solutions of Cl^- and Br^- . Last two points in the Br^- solid solution series ($x = 0.7$ and 0.8) are unstable and only exist in ambient conditions for about a minute.....	81

List of Symbols

Å: Angstrom

°C: degrees Celsius

XRD: X-ray Diffraction

(*t*): Tolerance factor

VSD: Vertical Sample displacement

Chapter 1

Introduction

1.1 General Motivation

While a large amount of research has been done regarding oxide perovskites with the general formula AMO_3 , the same cannot be said of their halide counterparts. The perovskite structure is an extremely versatile class of compounds that boasts a wide range of bandgaps and good charge carrier mobility due to its connected network of corner sharing octahedra. Given their useful intrinsic properties, perovskites have recently become a hot topic in the photovoltaic and electronics community for their potential use in solar cells, non-linear optics, and thermistors; to name a few. With a reported direct band gap of 1.52 eV² for $\text{CH}_3\text{NH}_3\text{PbI}_3$ and 2.25 eV³ for CsPbBr_3 , the lead halide perovskite class of compounds has desirable band gaps for use as a solar absorber in photovoltaic devices. While the ideal perovskite structure typically has the lowest band gap and highest electron mobility, distortions from the ideal symmetry (space group $Pm\bar{3}m$) have an impact on the band gap and electronic transport properties. The amount

of distortion from the ideal structure typically governs the amount by which the intrinsic properties of the structure change. Understanding how the electronic and optical properties of the perovskite structure can be tuned chemically through atomic substitutions is a necessary step in optimizing their properties for use in solar cells and radiation detectors. This research was conducted in order to further our knowledge of the lead halide perovskite structure and its susceptibility to substitution and the resulting effect those substitutions have on the electronic and optical properties.

1.2 The Perovskite Structure

Since the mineral perovskite was discovered in 1839 by Gustav Rose, the perovskite class of compounds has been drawing considerable attention due to the many desirable intrinsic properties of the crystalline structure. They can have impressive magnetic and electronic properties in addition to being highly versatile in the sense that many elements from all over the periodic table may be incorporated into the structure without breakdown of the intrinsic perovskite framework.

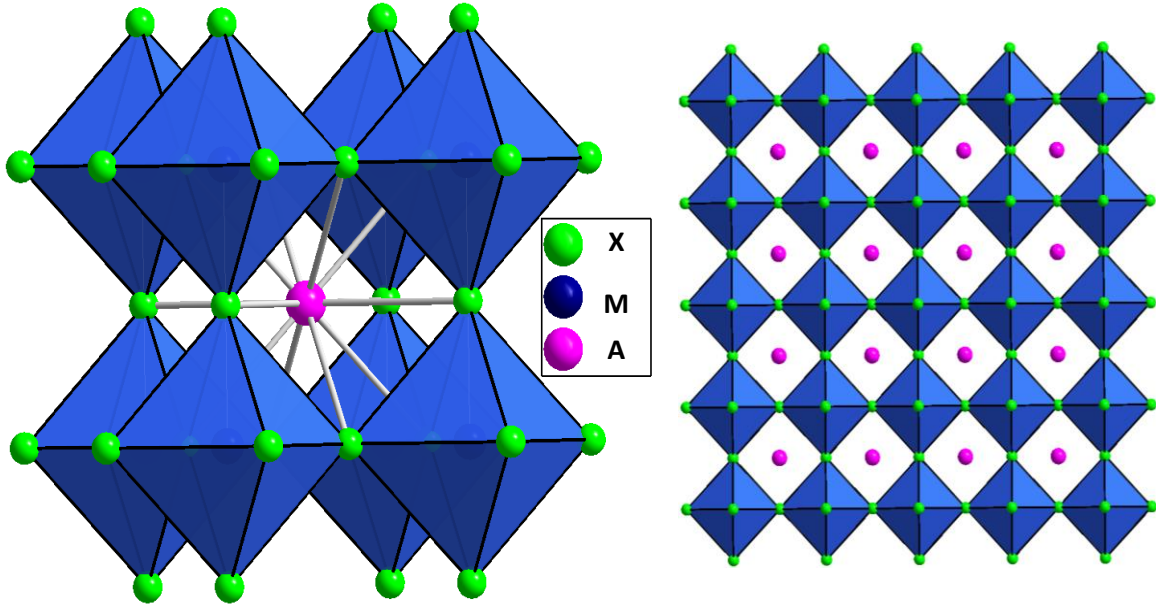


Figure 1.1: Ideal Perovskite Structure space group $Pm\bar{3}m$ (left). Expanded view illustrating the corner sharing octahedral network (right).

The perovskite structure has a general formula of AMX_3 , where “A” and “M” are cations and “X” is an anion. For the research conducted herein, the A and M site are mono and divalent cations respectively, and X is a halide ion (Cl^- , Br^- , or I^-). The perovskite structure is defined by a network of corner sharing MX_6 octahedra with the typically larger A-site cation sitting within the cuboctahedral holes generated by the MX_6 octahedral framework. The M-site cation is located at the center of an octahedron of X anions. The ideal perovskite structure, adopting a cubic symmetry (space group $Pm\bar{3}m$) is shown in Figure 1.1. When speaking in terms of space groups as a means to classify a compound, it is important to differentiate between those that are perovskite (containing corner sharing octahedral network) and those that are not (which do not contain the network of corner sharing octahedra), as both perovskite and non-perovskite can adopt identical space group symmetry.

1.3 Glazer Notation and Perovskite Tilt Systems

In order to make sense of latter results, it will be important to introduce the concept of octahedral tilting which is a means for the perovskite structure to distort in order to accommodate size mismatches between atoms while maintaining the perovskite octahedral network. This task will be simplified by first understanding how the octahedra tilt with respect to the ideal perovskite structure; this can be simply stated using a notation defined by A.M. Glazer in 1972. Glazer used a series of symbols of the type $a^\#b^\#c^\#$ to describe the tilting of the octahedra. The letters (in order) correspond to the magnitude of rotations about the x , y , and z Cartesian axis, and superscripts adopt a 0, +, or - to signify no tilting around an axis, successive tilting of the octahedra in the same direction from one layer to the next (in-phase tilting), or tilting in opposite directions from one layer to the next (out-of-phase tilting). Glazer defined 23 different types of tilting distortions of the octahedra, to which Howard and Stokes used a group theory based approach to illustrate that of the 23 distortions Glazer defined, there are just 15 truly unique patterns of octahedral tilting distortions, as shown in Figure 1.2.^{1,4}

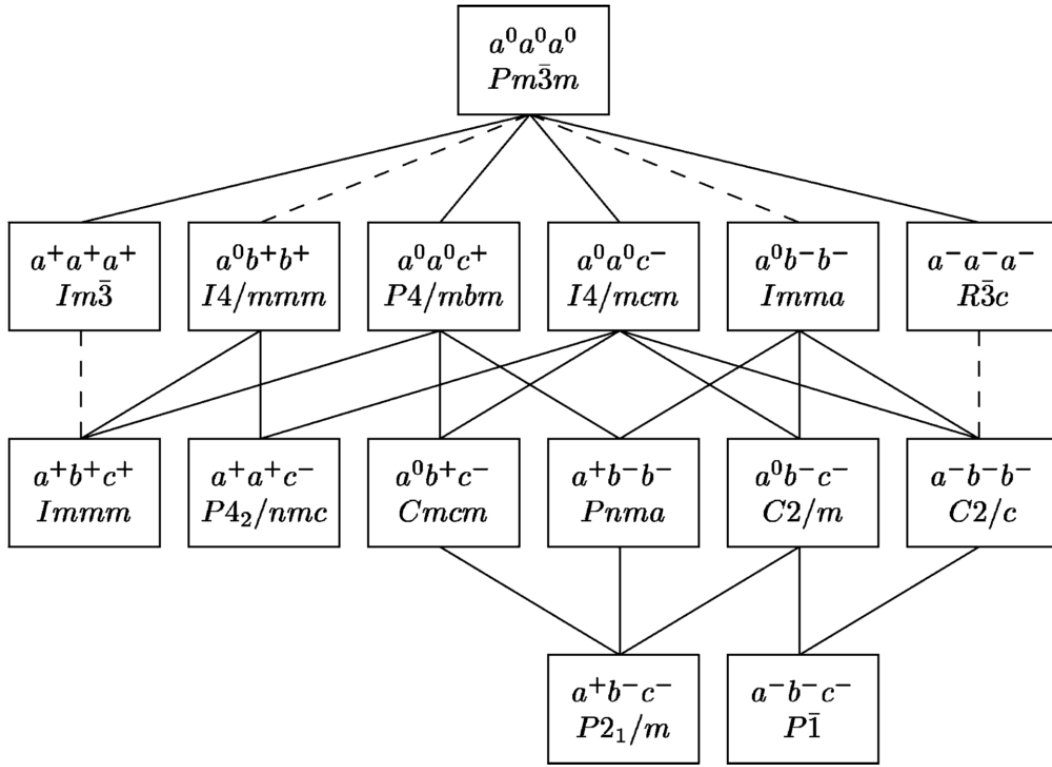


Figure 1.2: Schematic diagram indicating the group-subgroup relationships among the 15 space groups tabulated by Howard and Stokes. Dashed lines connecting a group with its subgroup indicates that the corresponding phase transition is required by Landau theory to be first order.¹

To simplify this characterization further, the research that has been completed herein will only deal with a select number of tilt systems, which include the ideal cubic perovskite $Pm\bar{3}m$ and perovskites that are distorted by one unique tilt ($I4/mcm$ and $P4/mbm$), and two unique tilts ($Pnma$). The tetragonal $P4/mbm$ structure arises when the rotations of the octahedra are in-phase about the c -axis, while the $I4/mcm$ symmetry is characterized by an out-of-phase rotation of the octahedra. The orthorhombic $Pnma$ structure occurs when there are out-of-phase tilts of equal magnitude about the a - and c -axis, and an in-phase tilt about the b -axis. The Glazer notation/tilt system for the ideal

perovskite is $a^0a^0a^0$, while the orthorhombic (space group *Pnma*) and tetragonal (space group *P4/mbm*) perovskites have $a^-b^+a^-$ and $a^0a^0c^+$ tilting respectively (Figure 1.3). Specifically the $a^-b^+a^-$ tilting is very common in perovskites, so much so that it is the most frequently observed distortion of the ideal perovskite structure accounting for over 50% of the AMX_3 perovskites.⁵

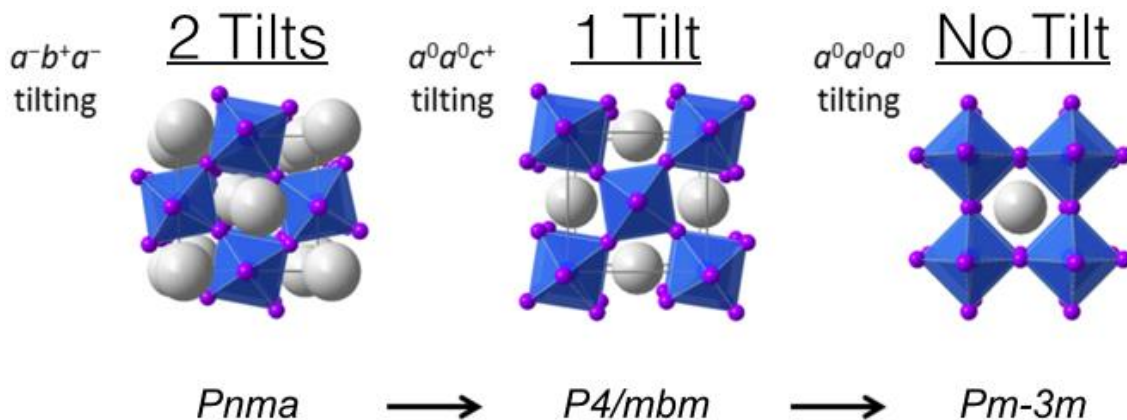


Figure 1.3: Examples of perovskite octahedral tilting from lower to higher symmetry space groups, with subsequent Glazer notation for associated tilt.

A sign of octahedral tilting is the appearance of peak splitting in the diffraction pattern. When identifying or characterizing a new perovskite, it is generally more useful to identify the crystal system first instead of the tilting scheme. This may seem counter intuitive as we know that it is the tilt scheme which ultimately governs the crystal system, however, splitting of the stronger reflections can more readily be resolved and characterized than the weak reflections used to characterize the tilt.⁶ When first inspecting

the diffraction patterns of perovskites, a good starting point is to characterize it using the splitting patterns of the most common perovskite tilt systems. In order to keep things simple and relevant to the current work, only the splitting patterns for the first four subcell reflections observed for the tilt systems $a^0a^0c^+$ (space group $P4/mbm$) and $a^-b^+a^-$ (space group $Pnma$) are illustrated in Figures 1.4 & 1.5 and shown in comparison to the parent ideal perovskite structure with no splitting. The reason for the appearance of additional peaks is attributed to the loss of translational and point symmetry that is present in the parent cubic structure.

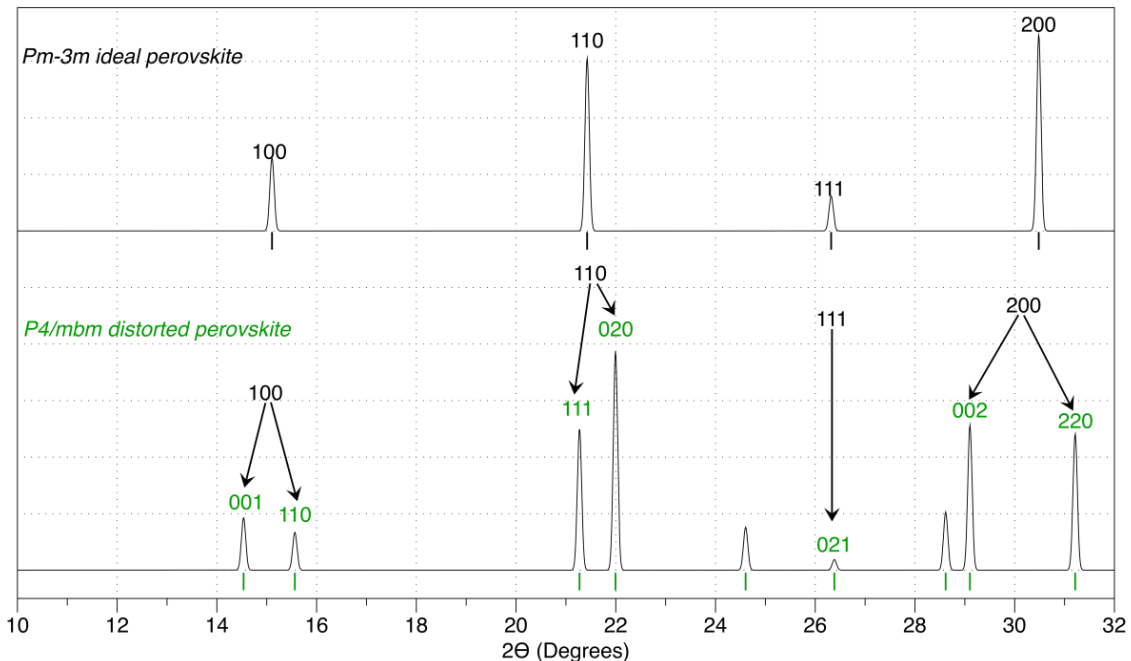


Figure 1.4: Pattern of peak splitting observed in the tetragonal distorted perovskite with the tilt system $a^0a^0c^+$. Ideal cubic perovskite reflections split in a characteristic manner when the perovskites octahedra become distorted. Distorted structures were modeled on the Crystal Maker program using CsPbBr_3 .

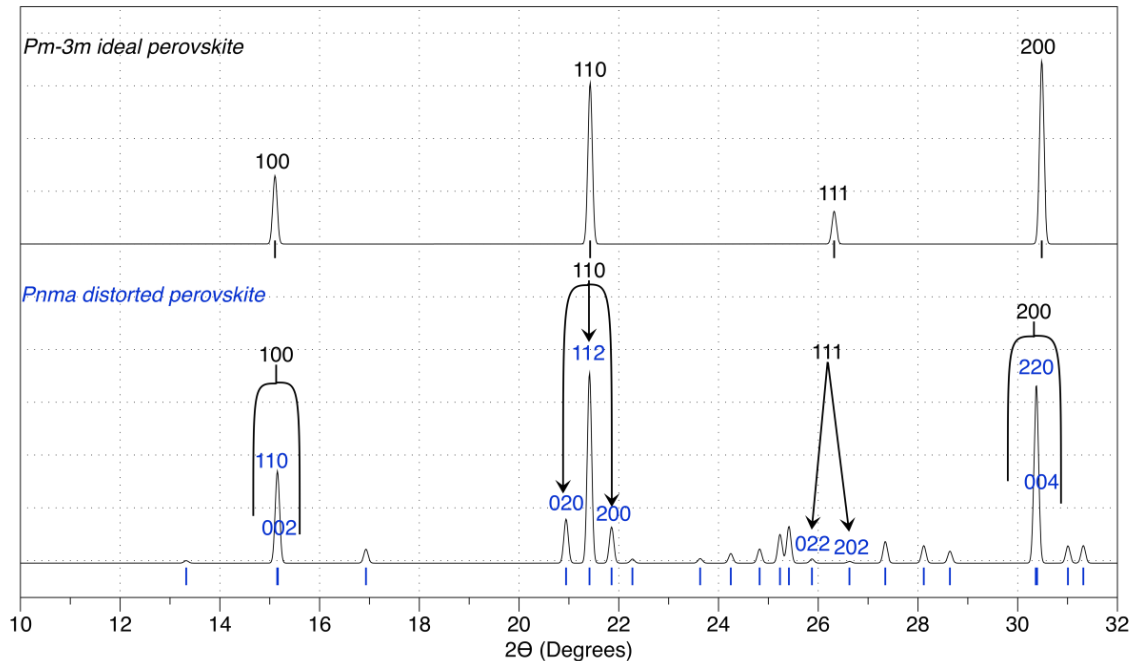


Figure 1.5: Peak splitting from the ideal perovskite reflections are observed for the distorted orthorhombic perovskite structure with tilt system $a^-b^+a^-$. Ideal cubic perovskite reflections split in a characteristic manner when the perovskites octahedra become distorted. Distorted structures were modeled on the Crystal Maker program using CsPbBr_3 .

As an example in Figure 5, the $Pm\bar{3}m$ (011) reflection splits into reflections (020 + 112 + 200) in the $Pnma$ distorted perovskite. There are more comprehensive tables in literature that characterize the splitting seen as a result of tilting for other common perovskite space groups.⁶ This process of characterizing the split peaks aids the process of properly identifying the crystal system. With proper identification of the crystal system, the diffraction pattern can be directly indexed using the appropriate unit cell parameters to that system. Once the approximate cell is identified, the final indexing and refinement of cell parameters and atomic positions is done using a Rietveld refinement program like TOPAS or GSAS.⁷

1.4 Tolerance Factor

The octahedral distortions previously described are driven by a mismatch in the size of the A-site cation compared to the cubo-octahedral cavities in the corner-sharing octahedral network. In 1926 V.M. Goldschmidt observed a relationship between atom size and overall stability of the perovskite structure. He observed, that in an ideal cubic perovskite constructed of rigid spheres, each of the cations in the AMX_3 formula were the perfect size for contact with the surrounding anions (X). From this relationship, the ions can then be related as shown in Equation 1:

$$R_A + R_X = \sqrt{2}(R_M + R_X) \quad (1)$$

Where R_A , R_M , and R_X are the ionic radii of the A and M-site cations as well as the X-site anion. Goldschmidt observed that with decreasing A-site cation size, there exists a point where it becomes too small and can no longer contact the anions in the ideal cubic structure. When this happens octahedral tilting can occur in the structure where the M-X-M bonds bend, tilting the M-site octahedra in order to bring the X anions into contact with the A-site.⁸ In order to allow for this distortion, a constant, t , is introduced and the above equation rearranged to solve for t , shown in equation 1.1:

$$t = \frac{R_A + R_X}{\sqrt{2}(R_M + R_X)} \quad (1.1)$$

(t) in the above equation is referred to as the tolerance factor, and its value serves as a measure of the fit of the A-site cation to the cubic corner connected network of MX_6 octahedra. Ionic radii were obtained from work published by Shannon, who investigated

how ionic size changed with different coordination environments.⁸ Through the years many oxide perovskite structures have been crystallographically characterized and their tolerance factors calculated. These investigations lead to the development of tolerance factor ranges that would predict the resulting crystal symmetry. It was determined that oxide perovskites form in the tolerance factor range of $1.05 > t > 0.78$.⁹ Work done by Woodward^{10,11} found that cubic perovskites typically exist above $t = 0.96$, below this value, down to $t = 0.87$, compounds would instead crystallize in the distorted orthorhombic perovskite structure with *Pnma* symmetry. For $t < 0.87$ the perovskite structure becomes unstable and other structure types, such as ilmenite, are typically observed. One goal of the completed work was to explore the relationship between tolerance factor and the stability of the cubic and distorted forms of the perovskite structure.

Chapter 2

Variable Temperature Studies of RbPbX₃ (X = Br⁻, Cl⁻, and I⁻)

2.1 Introduction

This research served to explore the stability of the perovskite structure for RbPbX₃ (X = Cl⁻, Br⁻, I⁻) compositions with small tolerance factors. Compounds such as CsPbCl₃, and CsPbBr₃ have already been shown to both crystallize in the distorted perovskite structure at room temperature and undergo phase transitions to higher symmetry phases with increasing temperature. To probe the stability of the perovskite phase, Cs⁺ was replaced with Rb⁺ in the A-site to lower the overall tolerance factor. Structure and phase changes of RbPbX₃ (X = Cl⁻, Br⁻, I⁻) will be the focus when comparing to the already known CsPbX₃ compounds in search for trends to help better understand and predict structural distortions and phase transitions of the perovskite structure in new compounds. In addition to observing phase changes, we hoped to get a better idea of how the atoms in the whole unit cell are changing through the transitions. To quantify this, we will address the bond distances between the Pb²⁺ and coordinating

halide to determine if successive perovskite phase transitions are accomplished by purely octahedral tilting, or if there is distortion of the bond distances that accompany the phase change.

2.1.1 Review of Relevant Literature

It is useful to first outline what has already been reported in existing literature regarding the CsPbX_3 and RbPbX_3 systems. The compounds CsPbCl_3 , CsPbBr_3^3 , and CsPbI_3^{12} have all been previously described in literature and serve as a means of comparison to the Rb^+ containing compounds. CsPbCl_3 and CsPbBr_3 crystallize in the orthorhombically distorted perovskite structure (space group *Pnma*) at room temperature and undergo phase changes to higher symmetry perovskite phases as the temperature increases.

CsPbCl_3 was initially reported by Moller¹³ in 1958 as a tetragonal phase (space group *P4mm*) which was later redetermined by K. Nitsch in 1995 who reported an orthorhombic perovskite structure with *Pmmm* symmetry.¹⁴ However, in 1971 Hirotsu *et al.* reported that CsPbCl_3 exists as an orthorhombic perovskite (like NaNbO_3) with *Pnma* symmetry below its orthorhombic/tetragonal transition temperature which starts at 37 °C and ends at 42 °C. The stability of the tetragonal structure is apparently short lived because a transition to the ideal cubic structure is reported on heating above 47 °C.¹⁵ Diffractograms were absent from the Nitsch paper, which lead to a questioning of validity

in the room temperature CsPbCl_3 assignment. In addition, it is apparent that there is confusion within the community regarding the proper assignment to this phase. This discrepancy needs to be addressed, as publications as recent as 2013¹⁶ have cited Moller when describing the room temperature behavior of CsPbCl_3 , which we believe to be inaccurate. To further investigate the room temperature phase, a sample of CsPbCl_3 was prepared and sent to the Advanced Photon Source to obtain an XRD of the material using their synchrotron source.

CsPbBr_3 underwent variable temperature diffraction studies performed by Stoumpos *et al.* where they identified two phase transitions through the application of heat from the room temperature distorted perovskite (space group *Pnma*). The successive transitions occur at 88 and 130 °C, transforming the perovskite crystal structure to tetragonal (space group *P4/mbm*) and then to the undistorted cubic phase (space group *Pm\bar{3}m*).³

In 2000 Monzel *et al.* conducted a redetermination of the phase diagram $\text{RbCl}/\text{PbCl}_2$ (Figure 2.1)¹⁷, which was first reported by K. Treis in 1914. Their redetermination lead to the discovery of two previously unknown phases with the formula $\text{Rb}_6\text{Pb}_5\text{Cl}_{16}$ and RbPb_2Cl_5 . $\text{Rb}_6\text{Pb}_5\text{Cl}_{16}$ goes on to peritectoidally degrade at 350 °C crystallizing into new structure types, while the RbPb_2Cl_5 phase persists until melting at 423 °C.

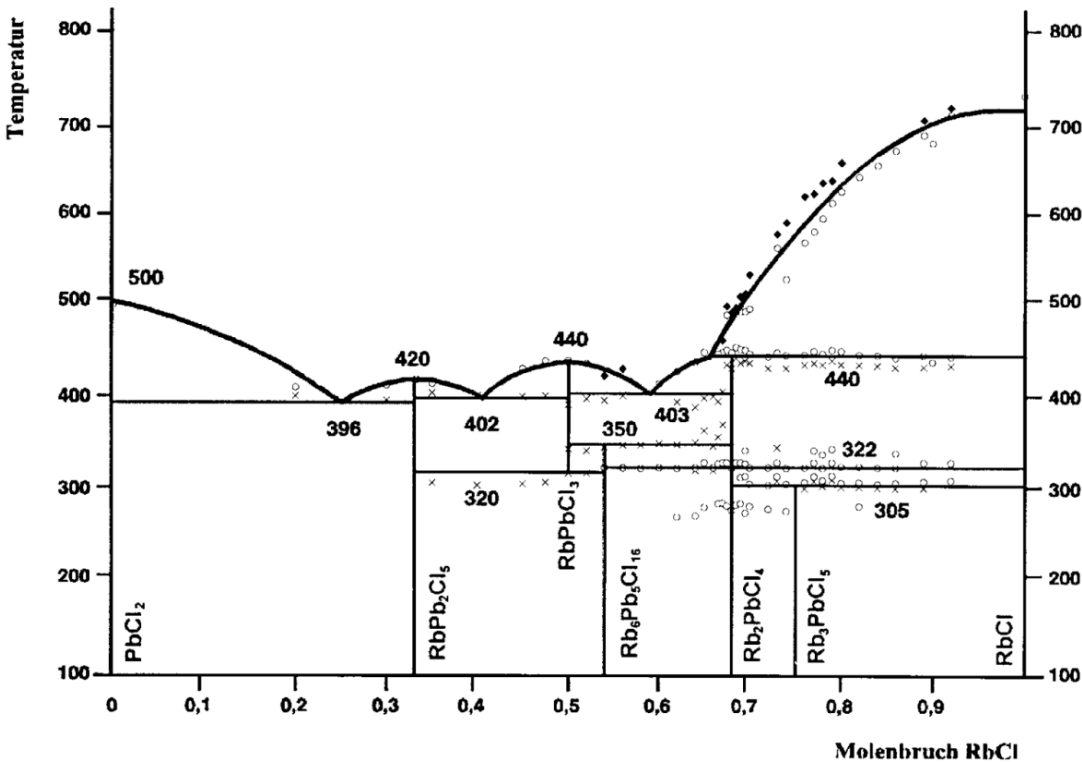


Figure 2.1: Phase diagram of RbCl/ PbCl₂. Taken from ref 17.

As seen in the phase diagram above, a 1:1 mixture (i.e. RbPbCl₃) will not form a single perovskite phase at room temperature but instead forms a two-phase mixture. The phases observed are Rb₆Pb₅Cl₁₆, which adopts a non-perovskite tetragonal structure (space group *P4/mbm*), and RbPb₂Cl₅ which has the monoclinic structure type of (NH₄)Pb₂Cl₅ (space group *P2₁/c*). Monzel *et al.* report that with the application of heat, a perovskite phase RbPbCl₃ (space group *Pm* $\bar{3}$ *m*) is observed at temperatures above 320 °C and, at 350 °C, the degradation of the Rb₆Pb₅Cl₁₆ phase gives rise to the appearance of reflections on the XRD pattern belonging to a new crystal structure of an unknown composition. The authors did not report a crystal structure for this new phase but rather

predicted its formula to be Rb_2PbCl_4 based on the presence of the RbPbCl_3 perovskite phase and the degradation of $\text{Rb}_6\text{Pb}_5\text{Cl}_{16}$. By conducting variable temperature measurements on RbPbCl_3 , we seek to identify a more precise onset of the perovskite phase, determine its symmetry and any structural phase transitions.

Unlike RbPbCl_3 , not much research has been done regarding RbPbBr_3 or its phase transitions. One non-perovskite room temperature phase has been previously described in literature by Powell.¹⁸ The phase identified was RbPb_2Br_5 and adopted the structure type of InSn_2I_5 (space group *I4/mcm*). The lack of information surrounding RbPbBr_3 was the main motivation to investigate whether a perovskite phase was possible at higher temperatures.

Trots and Mayagkota had previously conducted variable temperature diffraction studies on the compounds CsPbI_3 and RbPbI_3 in 2008.¹² Their findings concluded that both CsPbI_3 and RbPbI_3 were non-perovskites at room temperature adopting the structure type of NH_4PbCl_3 (space group *Pnma*). However, once the samples were heated, CsPbI_3 was observed to undergo a phase transition at 329 °C to the cubic perovskite structure (space group *Pm\bar{3}m*), while RbPbI_3 was observed to have no phase changes and simply melts at elevated temperatures.

2.2 Experimental Section

Powder crystalline samples of RbPbCl₃, RbPbBr₃, RbPbI₃, and CsPbI₃ were synthesized by solid state reactions at elevated temperatures. Reagents used were PbBr₂ (98+%, Alfa Aesar), PbCl₂ (99+%, J.T. Baker Chemical Co.), RbCl (99%, Alfa Aesar), RbBr (99.8%, Alfa Aesar), CsI (99.9%, Sigma Aldrich), PbI₂ (99.999+%, Sigma Aldrich). Reagents were combined in stoichiometric amounts and then ground using an agate mortar and pestle. Every gram of product equates to 15 minutes of grinding and scales up 15 min for every additional gram. After grinding, the mixture was transferred to a 25 ml alumina crucible and placed in a box furnace to react, in air, for 20 hours at 325 °C. If the resulting product was not phase pure at the end of the cycle, an additional program of grinding followed by heating was employed.

RbPbBr₃ was also synthesized via solution process by dissolving RbBr_(s) and PbBr_{2(s)} in concentrated HBr, resulting in immediate precipitation. However, this route yielded most RbPb₂Br₅ which is the non-perovskite tetragonal phase with *I4/mcm* symmetry, rather than the two phase mixture seen with solid state synthesis. Therefore, solid state grinding was used in the synthesis of all compounds.

2.2.1 Characterization

The phase purity of the sample was checked using both a Rigaku Miniflex tabletop diffractometer and Bruker D8 advance diffractometer (40 kV, 50 mA) equipped with a Lynx Eye position sensitive detector and a Ge 111 incident beam monochromator, which selects $K\alpha_1$ radiation. A scan range of 10–75° 2θ and a step size of 0.015 were used. Variable temperature experiments for RbPbCl₃, RbPbBr₃, and RbPbI₃ were also carried out using the Bruker D8 diffractometer equipped with a variable temperature HTK-1200 sample stage. The temperatures over which the data were acquired for RbPbCl₃ were 50, 150, 250, and 270–400 °C in 10 °C increments, while data sets were collected at 50, 150, 200, and 250–350 °C in 10 °C increments for both RbPbBr₃ and RbPbI₃. Ramp rates for all three compounds were 0.16 °C /s, a dwell time of 6.5 minutes was used before the start of each scan. Structure refinements were performed with the Rietveld method¹⁹ as implemented in the TOPAS software package.⁷

2.3 Results

2.3.1 The structure of CsPbCl₃

Earlier studies regarding the characterization of room temperature CsPbCl₃ are conflicting, with reports of *P4mm*, *Pmmm*, and *Pnma* symmetry. Group theory studies, as well as a large number of experimental studies of perovskites indicate that of these three the *Pnma* symmetry is an extremely common symmetry for perovskites to adopt, while the other symmetries previously reported are unusual symmetries for a perovskite.¹¹ In order to remove questions surrounding the structure, a sample of CsPbCl₃ was prepared using a solid state method and sent to the 11-BM beamline at the Advanced Photon Source (APS). The hope was that the improved signal-to-noise ratio from the synchrotron would allow for observation of weak superstructure reflections that can be used to confirm the *Pnma* symmetry previously reported by Hirotsu *et al.*¹⁵ The higher resolution would also allow us to resolve peak splitting that might otherwise be missed when using a laboratory diffractometer. A Rietveld refinement of the obtained diffractogram using an orthorhombic *Pnma* model, as well as refined parameters, are shown in Table 2 and Figures 2.2 and 2.3.

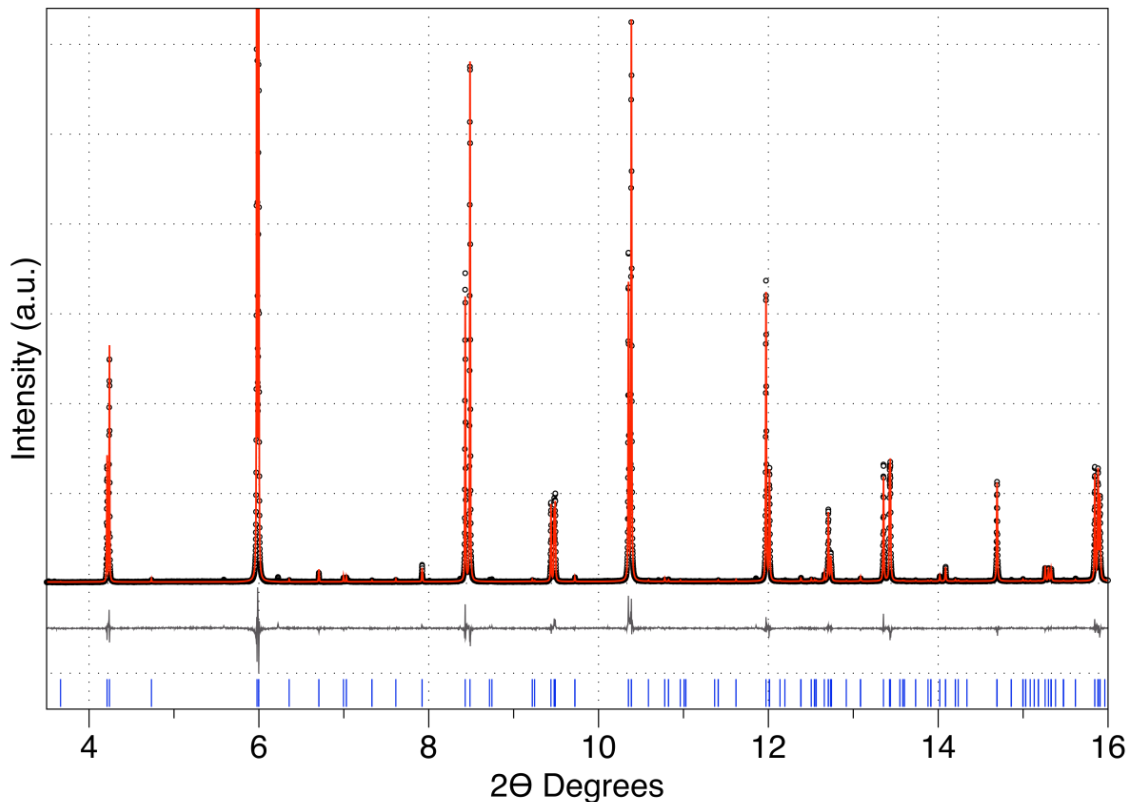


Figure 2.2: Refined synchrotron diffractogram of CsPbCl_3 obtained from the 11-BM beamline at APS.

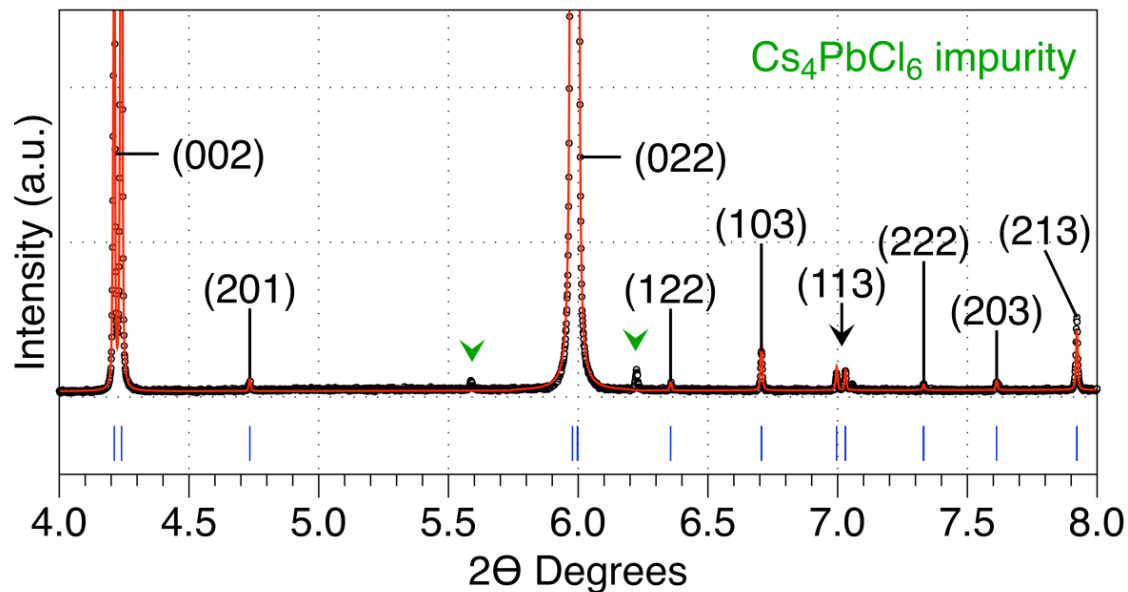


Figure 2.3: Select 2θ range to illustrate superstructure reflections. Labeled hkl reflections correspond to the observed reflections on a $2a_p \times 2a_p \times 2a_p$ cell.

Table 2.1: Refined structural information for room temp orthorhombic CsPbCl_3

Formula	CsPbCl_3				
Space group	<i>Pnma</i>				
Crystal System	Orthorhombic				
<i>Z</i>	4				
<i>a</i> (Å)	7.90201(2)				
<i>b</i> (Å)	11.24787(2)				
<i>c</i> (Å)	7.89935(2)				
<i>Volume</i> (Å ³)	702.100(2)				
<i>GOF</i>	1.59				
<i>Rwp</i>	8.637				
Site	Wyckoff	<i>x</i>	<i>y</i>	<i>z</i>	<i>U_{iso}</i>
Cs1	4c	0.5033(2)	0.25	0.50191(2)	0.0713(2)
Pb1	4b	0.5	0	0	0.02037(8)
Cl1	4c	-0.0378(5)	0.25	0.4715(5)	0.047(1)
Cl2	8d	0.2895(6)	0.0200(2)	0.7153(6)	0.0606(8)

From the synchrotron diffractograms, it becomes quite evident that there are more reflections present than are allowed in the tetragonal *P4mm* space group, and less reflections than there should be for the *Pmmm* space group assignment previously reported. Based on the previous work of Glazer in 1972⁴ and also discussed by Barnes, *et al.*²⁰, if the peaks in the diffraction pattern are indexed using the peaks from a doubled primitive cubic cell ($2a_p \times 2a_p \times 2a_p$), the Miller indices (*hkl*) can be classified into categories that provide information on the pattern of octahedral tilting. The presence of (odd, odd, odd) peaks indicates out-of-phase tilts, (odd, odd, even) peaks are associated with in-phase tilts, while (even, even, odd) peaks arise from A-site cation displacements. The presence of the (113) reflections, located at about 7.1°, correspond to an out-of-phase rotation of the Pb²⁺ octahedra while the odd, odd, even reflections (103) and (213) correspond to an in-phase rotation of the octahedra. Both in- and out-of-phase reflection

are consistent with an orthorhombic perovskite symmetry but forbidden in the primitive tetragonal symmetry that would result from the presence of only in-phase tilting. While the presence of the (113) reflection does not discount the space group *Pmmm* from being a possible match to the phase, the amount of observed reflections does. Reflections that are allowed for *Pmmm* symmetry but absent for *Pnma* symmetry are systematically absent in the observed diffractogram, leading to the assignment of the distorted perovskite orthorhombic symmetry (space group *Pnma*).

All fitted reflections observed in the diffractogram correspond to the space group *Pnma* ($a^-b^+a^-$), while all other reflections observed are accounted for by a trigonal Cs_4PbCl_6 impurity phase (space group $R\bar{3}c$) adopting the structure type of K_4CdCl_6 . The obtained results are in good agreement with the results previously reported by Hirotsu *et al.* in 1971 confirming the orthorhombic perovskite symmetry at room temperature. It is also useful to note the lattice parameters of the refined CsPbCl_3 phase. The fact that both *a* and *c* parameters are extremely close in value to one another shows that the orthorhombic unit cell is highly pseudo tetragonal making the peak splitting subtle and quite difficult to resolve on a laboratory diffractometer.

2.3.2 RbPbCl₃

Solid-state synthesis of RbPbCl₃ and RbPbBr₃ yielded two-phase mixtures of non-perovskite compounds at room temperature (Figure 2.4 for RbPbCl₃). Select variable temperature diffraction patterns for RbPbCl₃ are shown in Figure 2.5. Structural refinements of RbPbCl₃ confirm the presence of both a tetragonal Rb₆Pb₅Cl₁₆ phase (space group *P4/mbm*), and a monoclinic RbPb₂Cl₅ phase (space group *P2₁/c*) with the tetragonal phase making up 51 % (mole fraction) of the room temperature mixture, as calculated by TOPAS. Refinement data for room temperature phases are shown in Table 2.1 and 2.2. Crystal structures are shown in Figure 2.6. The structures of both room temperature phases had been previously reported in literature.^{14,17} The relative abundance of both phases is in disagreement with the phase diagram shown in Figure 2.1¹⁷ from which the lever rule gives an expected phase fraction of 80% Rb₆Pb₅Cl₁₆. The discrepancy may be due to errors in the estimate of the phase fraction in the Rietveld refinement, or the presence of an amorphous Rb-rich phase.

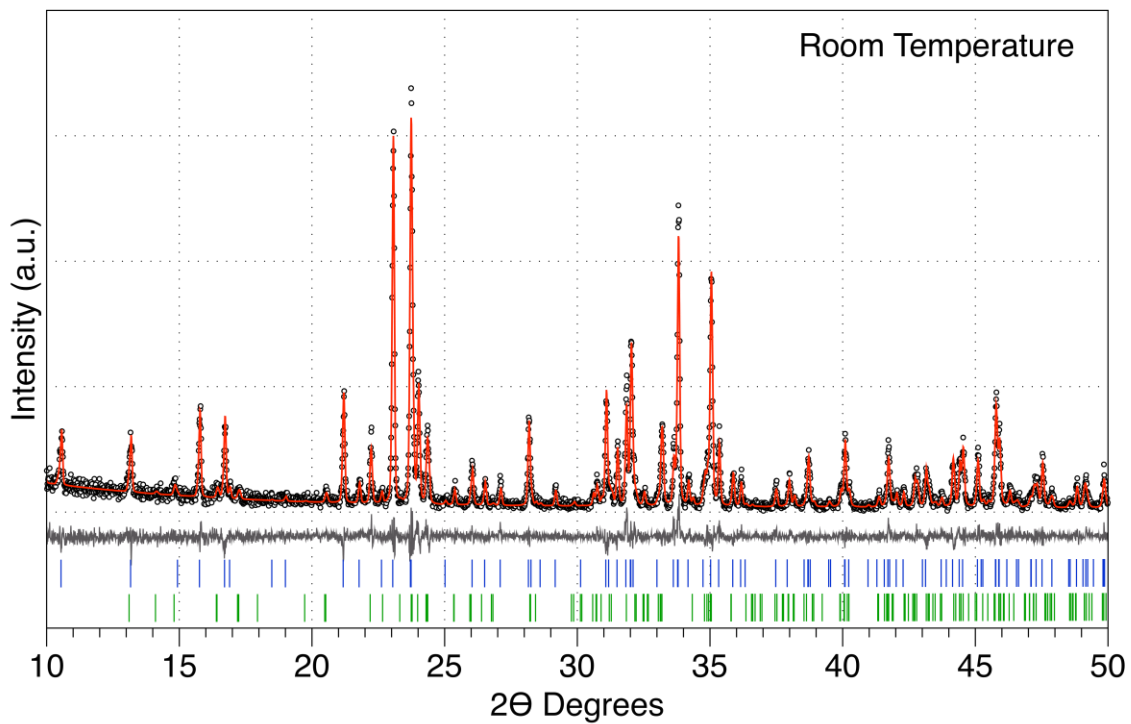


Figure 2.4: Rietveld refined XRD of RbPbCl₃ at room temperature showing the two-phase mixture. Markers at the bottom (green) correspond to RbPb₂Cl₅ $P2_1/c$ symmetry. Top markers (blue) correspond to Rb₆Pb₅Cl₁₆ $P4/mmb$ symmetry.

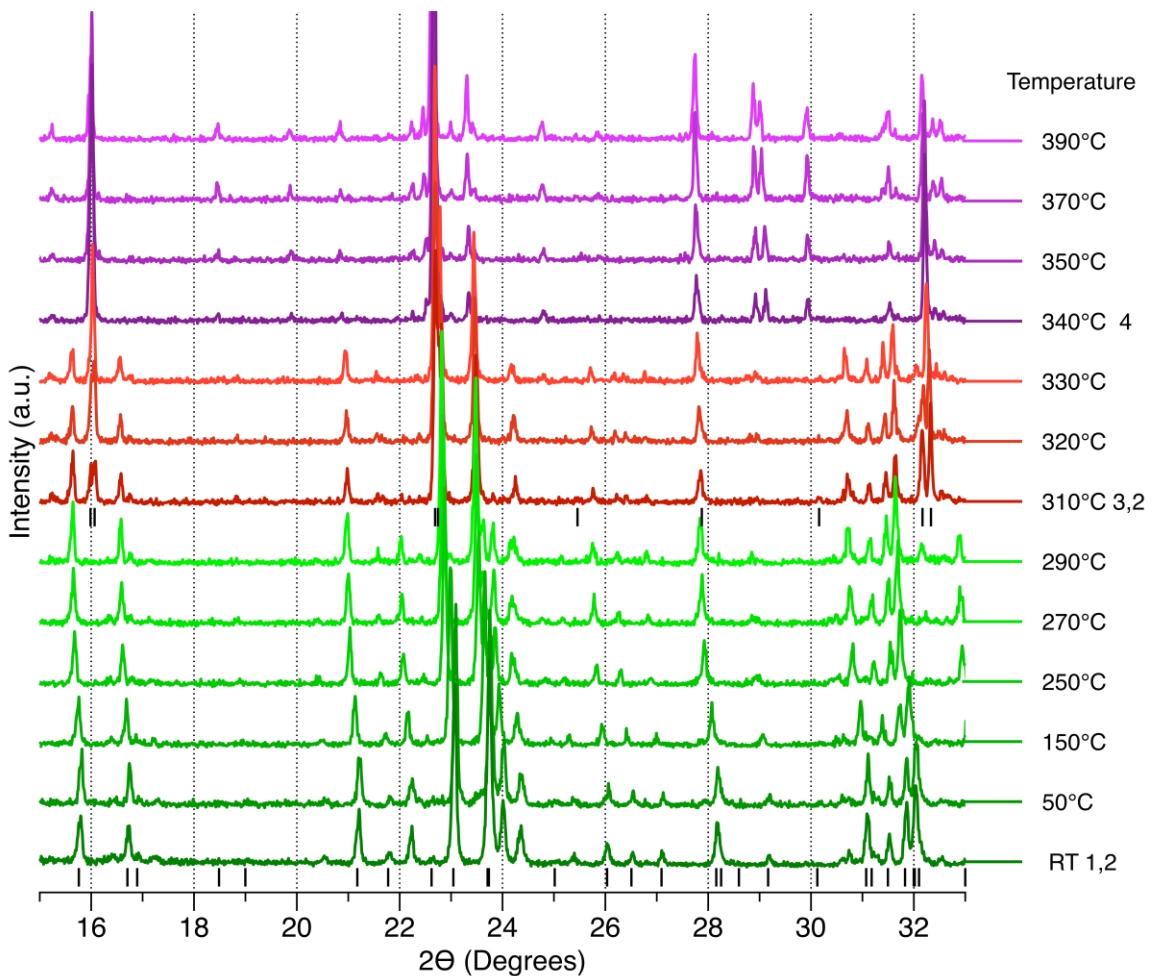


Figure 2.5: Select variable temperature diffraction patterns for RbPbCl_3 . Numbers correspond to phases present at that temperature. 1 = $\text{Rb}_6\text{Pb}_5\text{Cl}_{16}$, 2 = RbPb_2Cl_5 , 3 = RbPbCl_3 with tetragonal symmetry (space group $P4/mbm$), 4 = RbPbCl_3 with cubic symmetry (space group $Pm\bar{3}m$). Black hkl ticks illustrate reflections from phase 2 (RT) and phase 3 (310 °C).

Table 2.2: Refined lattice parameters for room temp $\text{Rb}_6\text{Pb}_5\text{Cl}_{16}$

Formula	$\text{Rb}_6\text{Pb}_5\text{Cl}_{16}$
Space Group	$P4/mbm$
Crystal System	Tetragonal
Z	4
$a(\text{\AA})$	11.8571(3)
$b(\text{\AA})$	11.8571(3)
$c(\text{\AA})$	11.2368(3)
Volume (\AA^3)	1579.87(8)
GOF	1.095
Rwp	19.941

Atomic positions were obtained from values previously reported in literature and were not refined further²¹

Table 2.3: Refined lattice parameters and structural information for room temp RbPb_2Cl_5

Formula	RbPb_2Cl_5				
Space Group	$P2_1/c$				
Crystal System	Monoclinic				
Z	4				
$a(\text{\AA}) / \alpha$	8.9937(5)				90
$b(\text{\AA}) / \beta$	8.0041(5)				90.141(5)
$c(\text{\AA}) / \gamma$	12.5492(7)				90
Volume (\AA^3)	902.93(9)				
GOF	1.095				
Rwp	19.941				
Site	Wyckoff	x	y	z	U_{iso}
Rb1	4e	0.012(4)	0.058(3)	0.831(2)	0.01(1)
Pb1	4e	0.494(2)	0.990(2)	0.174(1)	0.015(6)
Pb2	4e	0.247(2)	0.937(1)	0.498(2)	0.011(5)
Cl1	4e	0.031(8)	0.323(8)	0.079(5)	0.009(9)
Cl2	4e	0.451(8)	0.329(8)	0.092(5)	0.009(9)
Cl3	4e	0.229(8)	0.140(6)	0.304(5)	0.009(9)
Cl4	4e	0.259(7)	0.539(5)	0.519(5)	0.009(9)
Cl5	4e	0.292(8)	0.689(7)	0.213(5)	0.009(9)

Initial atomic positions were used from the reported parent structure $(\text{NH}_4)\text{Pb}_2\text{Cl}_5$.²²

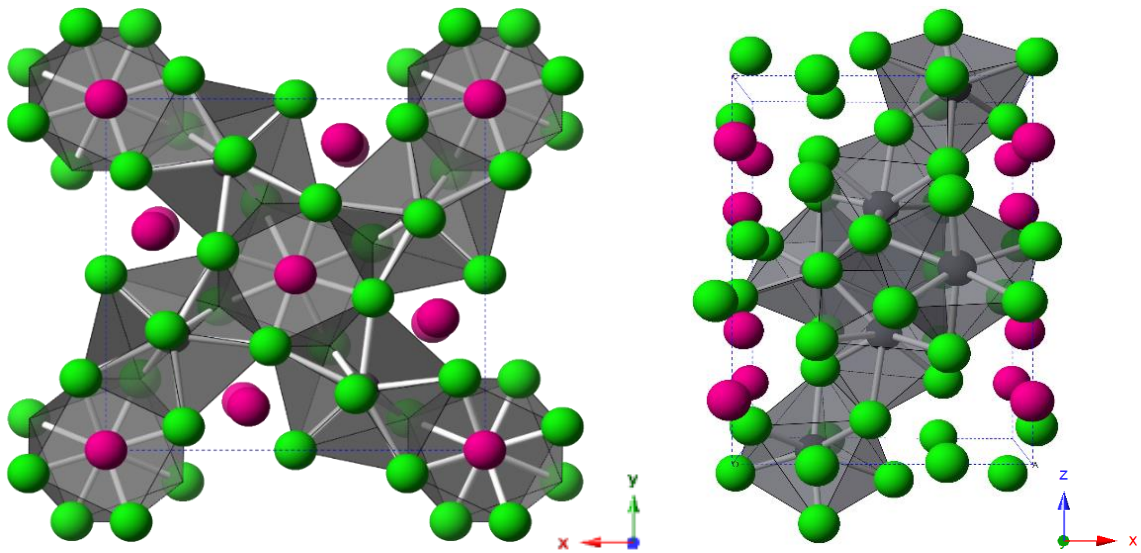


Figure 2.6: The structures of $\text{Rb}_6\text{Pb}_5\text{Cl}_{16}$ (left) and RbPb_2Cl_5 (right). The Cl^- , Pb^{2+} , and Rb^+ ions are represented with green, gray, and magenta spheres, respectively.

Upon heating, a tetragonally distorted perovskite structure (space group $P4/mbm$) begins to appear at 310 °C. This is the first identification of this particular phase which is rather short lived; existing for about 30 °C before undergoing a second phase transition. It is necessary to note that this tetragonal phase could initially originate as an orthorhombic phase quickly transitioning to a tetragonal phase, similar to the Cs^+ analog. However due to the resolution of the lab diffractometer coupled with decreased resolution that accompanies the use of the HTK-1200 high temperature stage, all resolvable reflections correspond to the tetragonal perovskite symmetry $P4/mbm$. Figure 2.7 shows the XRD of the refined tetragonal phase and a structure model as well as refined structural information can be found in Figure 2.8 and Table 2.4.

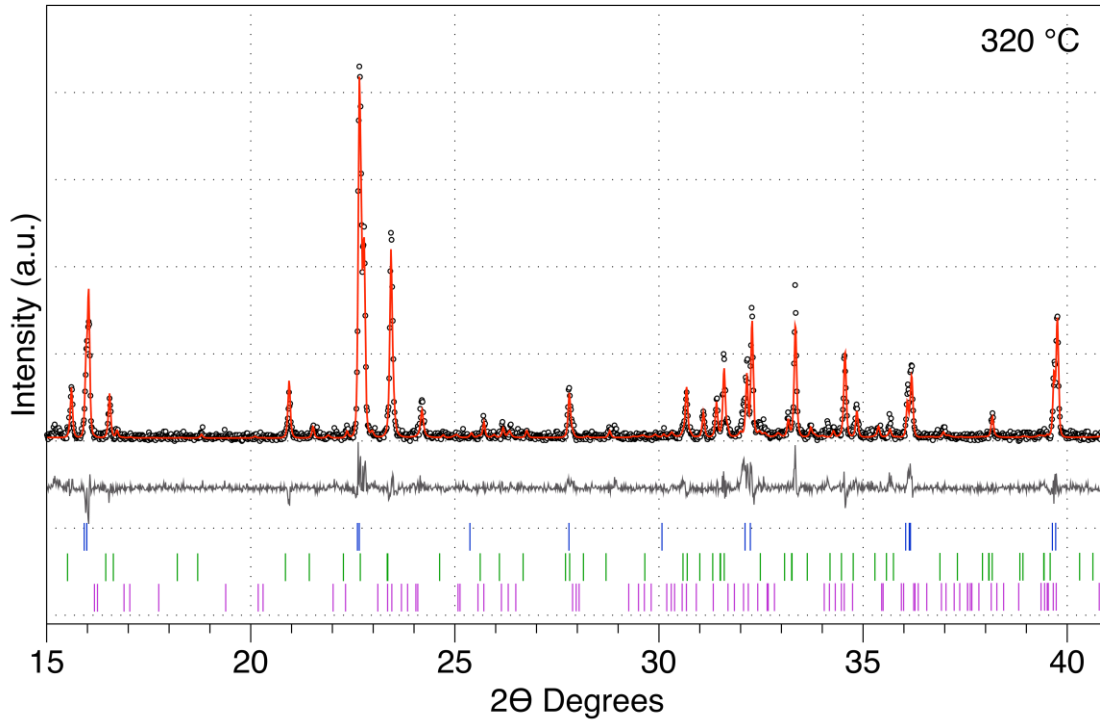


Figure 2.7: Rietveld refined XRD of tetragonal perovskite RbPbCl_3 at $320\text{ }^\circ\text{C}$. Blue markers correspond to RbPbCl_3 perovskite with $P4/\text{mbm}$ symmetry. Green markers correspond to $\text{RbPb}_2\text{Cl}_5 P2_1/\text{c}$ symmetry. Purple markers correspond to $\text{Rb}_6\text{Pb}_5\text{Cl}_{16} P4/\text{mbm}$ symmetry.

Table 2.4: Refined lattice parameters and structural information for high temp tetragonal phase RbPbCl_3

Temperature ($^\circ\text{C}$)	320				
Formula	RbPbCl_3				
Space group	$P4/\text{mbm}$				
Crystal System	Tetragonal				
Z	2				
a (\AA)	7.8590(3)				
c (\AA)	5.5788(3)				
Volume (\AA^3)	344.57(4)				
VSD (mm)	0.1398(39)				
GOF	1.191				
R_{wp}	36.798				
Site	Wyckoff	x	y	z	U_{iso}
Rb1	2c	0	0.5	0.5	0.150(9)
Pb1	2a	0	0	0	0.050(4)
Cl1	2b	0	0	0.5	0.18(4)
Cl2	4g	0.215(4)	0.715(4)	0	0.18(2)

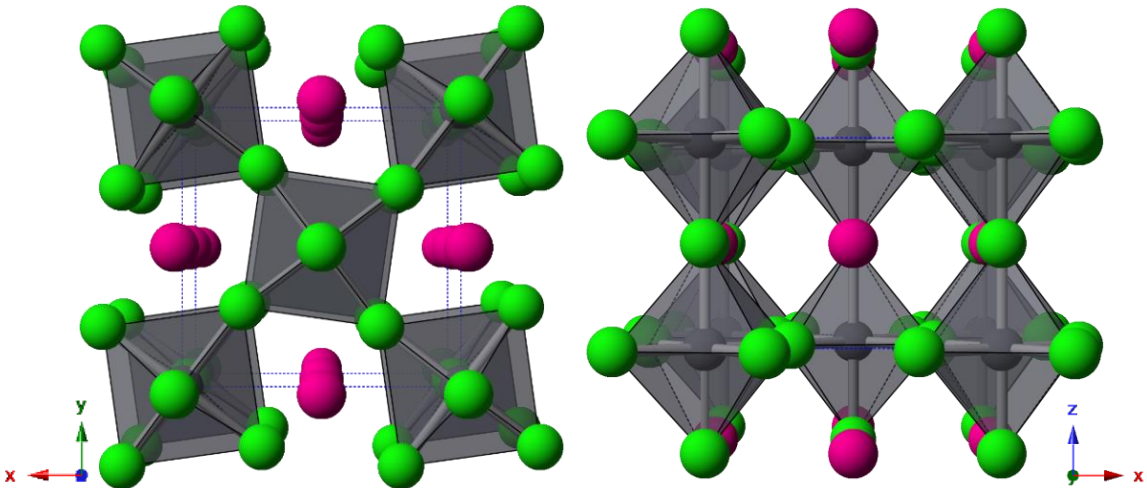


Figure 2.8: The structure of tetragonal RbPbCl_3 $P4/mbm$ orientated down the crystallographic c-axis (left) and b-axis (right). The Cl^- , Pb^{2+} , and Rb^+ ions are represented with green, gray, and magenta spheres, respectively.

Vertical sample height displacement (VSD) was reported in order to illustrate how the sample shape was changing on the sample holder as the temperature increased. With increasing temperature, the sample expanded, which is observed in the lattice parameters, leading to a larger sample height displacement. The reason for a less than optimal R_{wp} of some of the refined diffractograms can be attributed to the shape of the sample upon expansion. Refinements of high temperature RbPbCl_3 and RbPbBr_3 phases show that the calculated profile falls slightly short of the observed 2θ peak position at early 2θ values but then falls slightly after the observed 2θ peak position at higher 2θ values. This discrepancy in profile fitting is most likely due to a doming of the sample on the sample holder, which cannot be reconciled in the refinements.

RbPbCl_3 undergoes another phase change at 340°C to two separate phases, one of which is the ideal cubic perovskite ($Pm\bar{3}m$), while the other is an uncharacterized phase with a potential formula of Rb_2PbCl_4 , as predicted by H. Monzel *et al.* from the

degradation of the $\text{Rb}_6\text{Pb}_5\text{Cl}_{16}$ at 340 °C.¹⁷ Structural and lattice information has only been reported for the cubic perovskite phase while the unaccounted for peaks in the 350 °C spectra belong to an uncharacterized structure with a predicted chemical formula of Rb_2PbCl_4 .¹⁷ Characterization of the predicted Rb_2PbCl_4 phase was not performed for this research, however, the onset of its appearance is consistent with what has already been reported in literature. Shown in Figure 2.9, 2.10 and Table 2.5 are the refined XRD pattern, cubic perovskite structure and refined lattice parameters respectively for the RbPbCl_3 cubic perovskite phase. The high R_{wp} for the cubic phase is accounted for by the unidentified phase, which was not fit in the refinement.

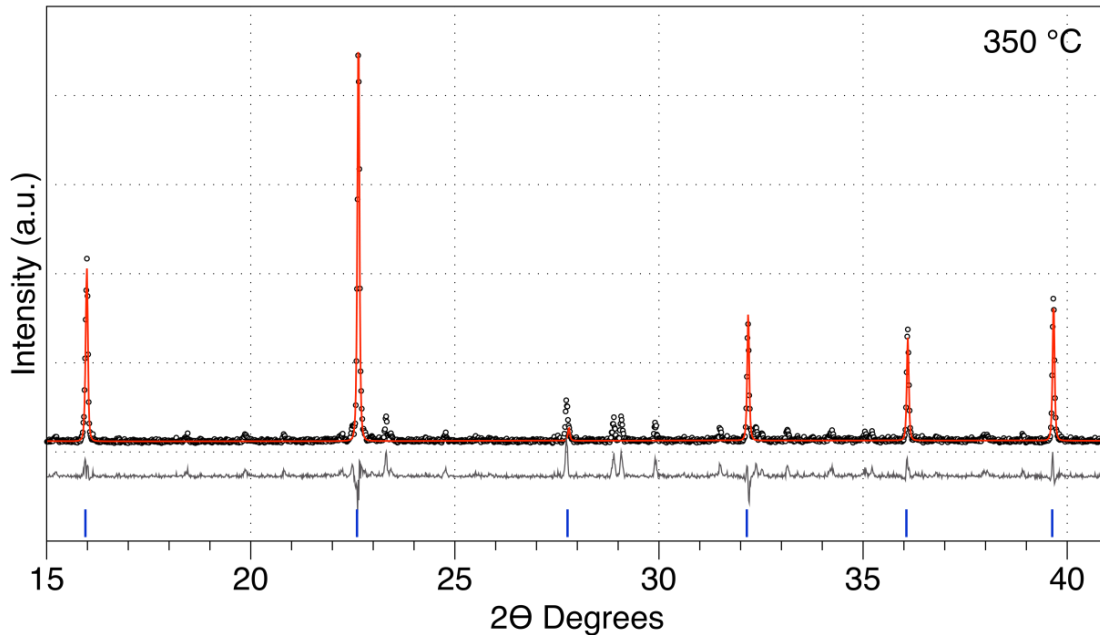


Figure 2.9: Rietveld refined XRD of tetragonal perovskite RbPbCl_3 at 350 °C. Blue markers correspond to RbPbCl_3 perovskite with $Pm\bar{3}m$ symmetry.

Table 2.5: Refined lattice parameters and structural information for high temp cubic phase RbPbCl_3

Temperature (°C)	350				
Formula	RbPbCl_3				
Space group	$Pm\bar{3}m$				
Crystal System	Cubic				
Z	1				
$a(\text{\AA})$	5.5745(2)				
Volume (\AA^3)	173.23(2)				
VSD (mm)	0.1660(25)				
GOF	1.4				
Rwp	45.693				
Site	Wyckoff	x	y	z	U_{iso}
Rb1	1b	0.5	0	0	0.25(2)
Pb1	1a	0	0	0	0.049(3)
Cl1	3d	0.5	0.5	0.5	0.21(1)

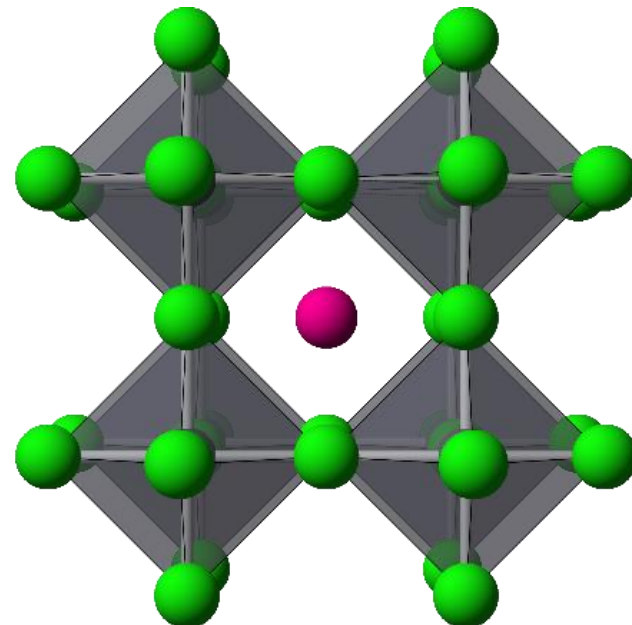


Figure 2.10: Structure of high temperature cubic perovskite (space group $Pm\bar{3}m$) RbPbCl_3 . The Cl^- , Pb^{2+} , and Rb^+ ions are represented with green, gray, and magenta spheres, respectively.

2.3.3 RbPbBr₃

Like RbPbCl₃, room temperature RbPbBr₃ also contains a two-phase mixture composed of 96.7% RbPbBr₃ (space group *Pnma*) with the NH₄CdCl₃ structure type and 3.3% RbPb₂Br₅ (space group *I4/mcm*). It also undergoes structural transitions to higher symmetry perovskite phases when heated up to 350 °C. Select variable temperature diffraction patterns for RbPbBr₃ are shown in Figure 2.11. Structural data for the RbPb₂Br₅ phase was reported at 50 °C where it appears to make up a larger fraction of the sample, allowing for a more accurate determination of its structure. At room temperature the non-perovskite *Pnma* phase dominates, however, once at 50 °C the non-perovskite tetragonal phase (space group *I4/mcm*) dominates the phase mixture. Since the compound was synthesized in a 1:1 ratio, one would expect to see 100% of the RbPbBr₃ *Pnma* non-perovskite phase. Instead, it is observed to have a small amount of the tetragonal impurity, indicating a lack of Rb⁺ which would drive the formation of the RbPb₂Br₅ tetragonal phase. It is necessary to mention that the diffractograms at 50 °C and 150 °C contain a few unaccounted peaks that do not correspond to starting materials or either of the two room temperature phases. As was the case with RbPbCl₃, it is possible that the missing Rb⁺ could be present as a poorly crystalline Rb-rich phase. We can conclude that if there is an additional phase present within this temperature region, it is not of the perovskite structure, as the few peaks present did not match those expected for a perovskite. At 250 °C, both room temperature phases as well as the orthorhombic distorted perovskite (space group *Pnma*) phase, exist as an unequilibrated mixture. The diffractogram confirms this because peaks associated with perovskite phase, which

appear at higher temperatures, are clearly present toward the end of the scan but not at the beginning. While this pattern could not be refined, it is included because it clearly shows the onset of the transformation to the perovskite form.

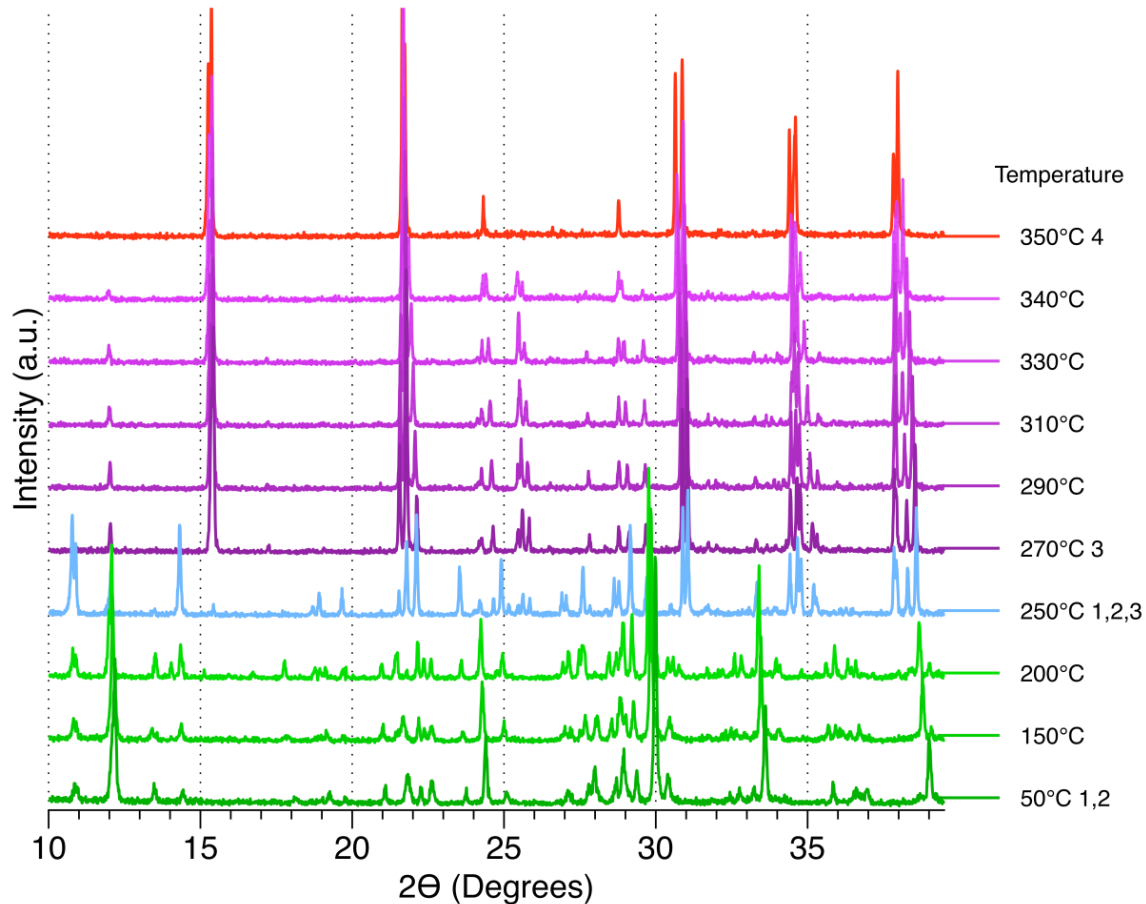


Figure 2.11: Select variable temperature diffractograms of RbPbBr₃. Numbers correspond to phases present at that temperature. 1 = RbPbBr₃ non-perovskite with NH₄CdCl₃ structure (space group *Pnma*), 2 = RbPb₂Br₅, 3 = RbPbBr₃ distorted perovskite with orthorhombic symmetry (space group *Pnma*), 4 = RbPbBr₃ distorted perovskite with tetragonal symmetry (space group *P4/mbm*).

As the temperature increases, the compound undergoes a typical thermal expansion of the lattice parameters accompanied by a decrease in the magnitude of octahedral tilting when transitioning from the orthorhombic perovskite phase to a higher symmetry perovskite. These phenomena are observed experimentally, both by a shift in the hkl reflections to lower 2 theta values, as well as a decrease in peak splitting. As previously mentioned, RbPbBr₃ is not a perovskite at room temperature and forms a two phase mixture of non-perovskite structures comprised of an orthorhombic and tetragonal phases with *Pnma* and *I4/mcm* symmetry, which can be seen in the refined room temperature XRD pattern Figure 2.12. The orthorhombic phase (Figure 2.13) is very prominent at room temperature and was discovered to be isostructural, with the room temperature phase of CsPbI₃ and RbPbI₃, adopting the structure type of NH₄CdCl₃.¹² Rietveld refined structural parameters (shown in Table 2.6) confirms the orthorhombic cell symmetry with the Pb²⁺ ions located at the center of a distorted octahedra coordinated by six bromine atoms.

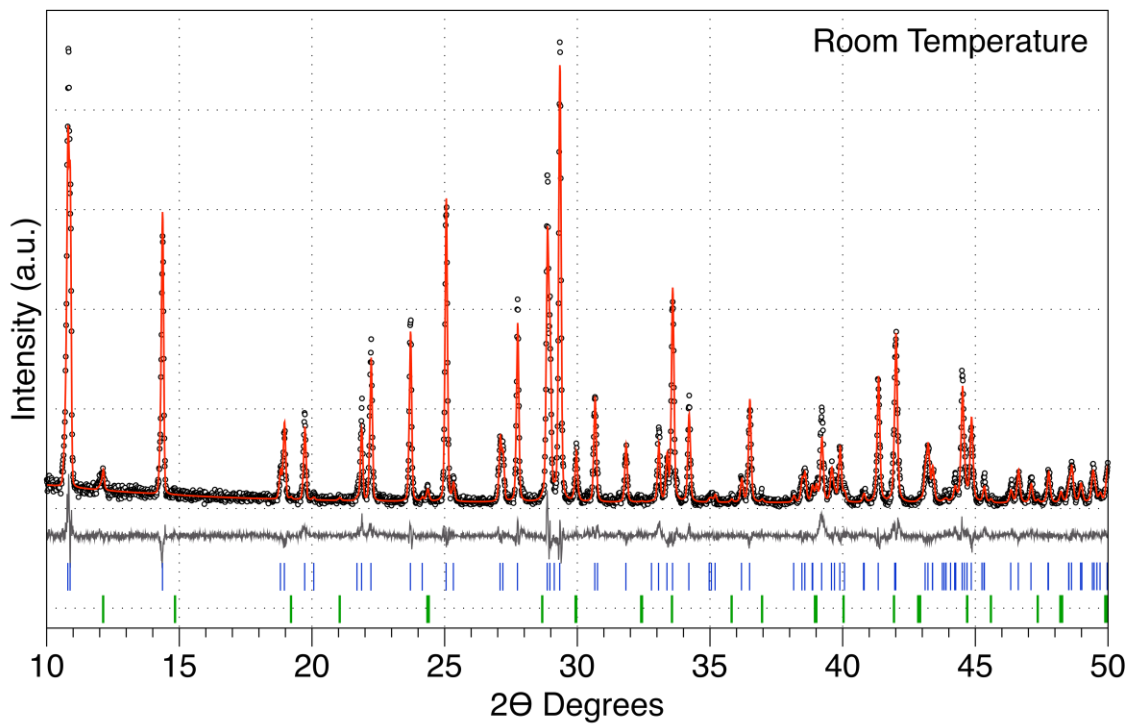


Figure 2.12: Rietveld refined XRD of RbPbBr₃ at room temperature showing the two-phase mixture. Markers at the bottom (green) correspond to RbPb₂Br₅. Top markers (blue) correspond to RbPbBr₃ with the NH₄CdCl₃ structure.

Table 2.6: Refined lattice parameters and structural information for room temp non-perovskite RbPbBr_3

Temp (°C)	25				
Formula	RbPbBr_3				
Space group	<i>Pnma</i>				
Crystal System	Orthorhombic				
<i>Z</i>	4				
<i>a</i> (Å)	9.3541(2)				
<i>b</i> (Å)	4.5918(1)				
<i>c</i> (Å)	16.3720(4)				
Volume (Å ³)	703.22(4)				
VSD (mm)	0.031(1)				
GOF	1.346				
<i>Rwp</i>	21.193				
Site	Wyckoff	<i>x</i>	<i>y</i>	<i>z</i>	<i>U_{iso}</i>
Rb1	4c	0.0939(5)	0.25	0.3252(4)	0.034(3)
Pb1	4c	0.1690(2)	0.75	0.0618(2)	0.035(2)
Br1	4c	0.3379(7)	0.25	-0.0100(4)	0.056(3)
Br2	4c	0.0284(6)	0.75	-0.1162(4)	0.028(3)
Br3	4c	0.3135(6)	0.75	0.2127(4)	0.025(3)

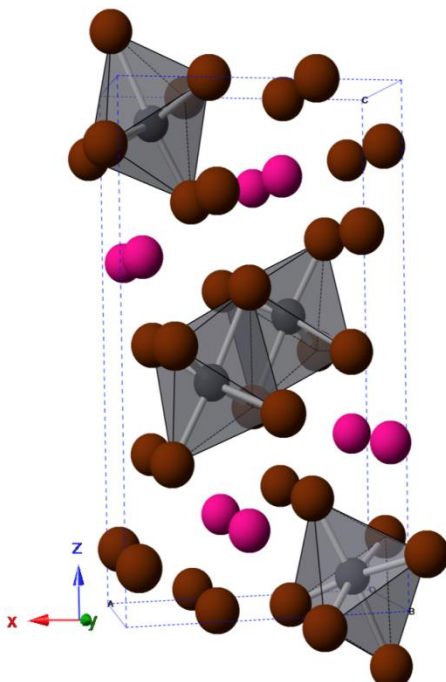


Figure 2.13: Orthorhombic non-perovskite RbPbBr_3 with *Pnma* symmetry. The Br^- , Pb^{2+} , and Rb^+ ions are represented with brown, gray, and magenta spheres, respectively.

The octahedra gets its distortion from two pairs of equatorial $\text{Pb}-\text{Br}$ distances, 3.085(4)Å and 3.019(4)Å, and two axial ones, 2.822(7)Å and 3.190(7)Å, which are consistent with values reported in literature for this structure type.¹² Refined lattice parameters of $a = 9.3542(2)$, $b = 4.5918(1)$, and $c = 16.3720(4)$ are slightly smaller than the reported values for RbPbI_3 , which is congruent with the smaller Br^- halide in the structure.

The second phase present crystallizes in the tetragonal geometry (space group $I4/mcm$) with the formula RbPb_2Br_5 (Figure 2.14). This structure was originally characterized and reported by H.M Powell in 1939 and later confirmed by Daniel Becker and Horst P. Beck in 2004. Refined structural information is shown in Table 2.7 and is in close agreement with the values previously reported.²³

Table 2.7: Refined lattice parameters and structural information for RbPb_2Br_5 50 °C

Temp (°C)	50				
Formula	RbPb_2Br_5				
Space group	$I4/mcm$				
Crystal System	Tetragonal				
Z	4				
$a(\text{\AA})$	8.4457(4)				
$b(\text{\AA})$	8.4457(4)				
$c (\text{\AA})$	14.609(1)				
Volume (\AA^3)	1042.0(1)				
VSD (mm)	0.097(3)				
GOF	1.491				
Rwp	38.956				
Site	Wyckoff	x	y	z	U_{iso}
Rb1 (4a)	4a	0	0	0.25	0.041(9)
Pb1 (8h)	8h	0.1635(9)	0.6635(9)	0	0.057(4)
Br1 (4c)	4c	0	0	0	0.04(1)
Br2 (16l)	16l	0.157(2)	0.657(2)	0.3656(7)	0.068(6)

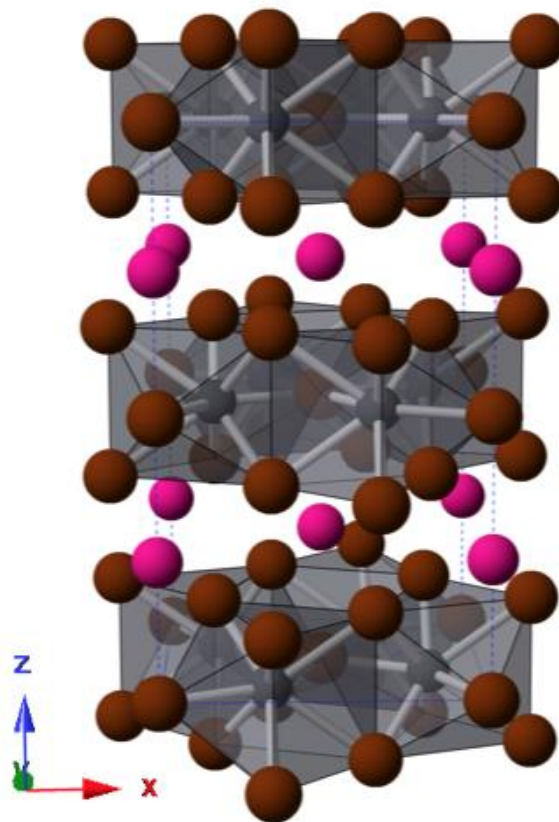


Figure 2.14: Structure of room temperature RbPb_2Br_5 non-perovskite tetragonal phase (space group $P4/mbm$). The Br^- , Pb^{2+} , and Rb^+ ions are represented with brown, gray, and magenta spheres, respectively.

The first of the phase transitions is to an orthorhombic perovskite (space group $Pnma$) consisting of a network of corner connected lead octahedra coordinated by six Br atoms. The glazer notation which describes the observed octahedral tilting in the structure is $a^-b^+a^-$, indicating the two out-of-phase tilts down the a and c crystallographic direction, and an in-phase tilt of the octahedra down the b direction or y axis. The $Pnma$ perovskite phase forms through the atomic rearrangement of the non-perovskite phase with NH_4CdCl_3 structure type. This is supported by the ingrowth of the perovskite phase accompanying the outgrowth the non-perovskite phase. Both the perovskite and non-

perovskite *Pnma* phases contain the same formula RbPbBr₃ but adopt different structure types of GdFeO₃ and NH₄CdCl₃ respectively. The XRD taken at 260 °C (Figure 2.15) shows the new structure to adopt an orthorhombic crystal system with a distorted perovskite symmetry (Figure 2.16). Due to the temperature range selected for the experiment we were unable to pinpoint the exact temperature of transition. Given the available data, we can say that the sample transforms to a *Pnma* (a⁻b⁺a⁻) perovskite somewhere close to 250 °C. The orthorhombic perovskite form of RbPbBr₃ is isostructural with the structure of RbPbCl₃ discussed earlier, and the room temperature structure of CsPbBr₃, which has been previously reported in literature.²⁴ Reported distances for the equatorial Br atoms around the Pb²⁺ octahedra are 2.955 Å and 2.984 Å, while the axial Br distance is 2.964 Å for CsPbBr₃. Refined distances for the equatorial and axial Br⁻ atoms for the Rb⁺ containing phase are, 2.981(9) Å, 3.008(9) Å, and 2.986(3) Å respectively. Close agreement in bond distances confirms a proper structural model for the RbPbBr₃ compound, in the slightly longer Pb–Br distances can be explained by the elevated temperature of the phase, which increases the overall cell volume. Table 2.8 shows the refined structural data for the orthorhombic perovskite RbPbBr₃.

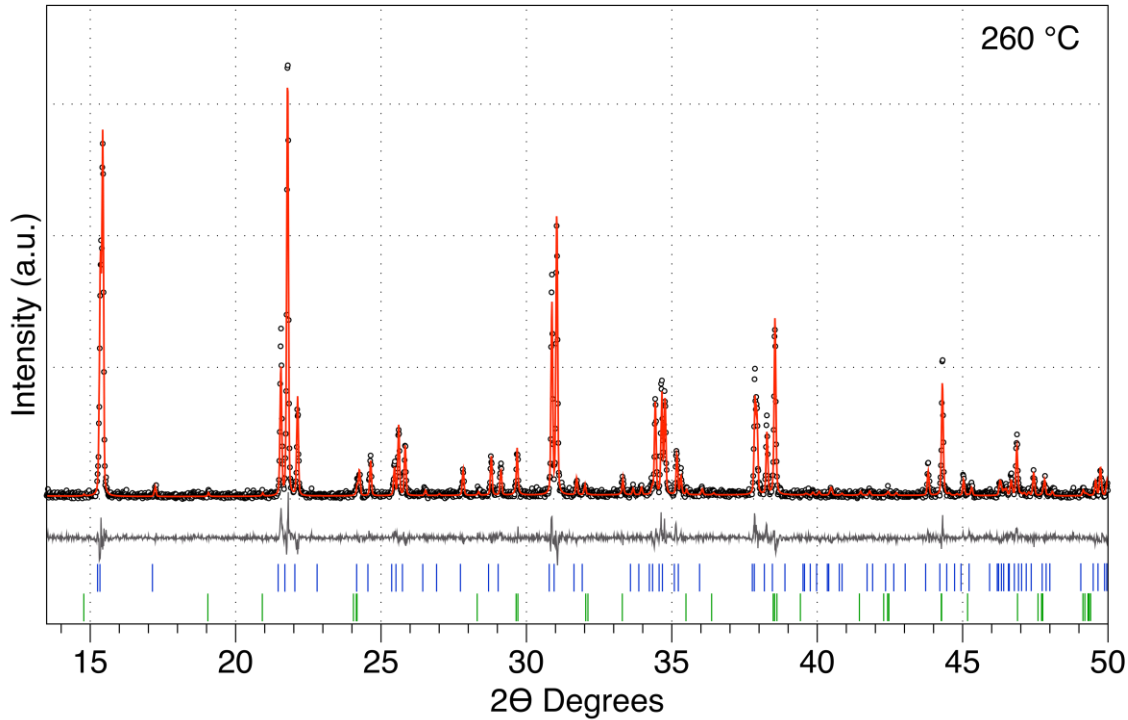


Figure 2.15: Rietveld refined XRD of tetragonal perovskite RbPbBr_3 at $260\text{ }^\circ\text{C}$. Blue markers correspond to RbPbBr_3 perovskite with $Pnma$ symmetry. Green markers (bottom) correspond to RbPb_2Br_5 with $I4/mcm$ symmetry.

Table 2.8: Refined lattice parameters and structural information for high temp orthorhombic perovskite phase RbPbBr_3

Temperature ($^\circ\text{C}$)	260				
Formula	RbPbBr_3				
Space group	$Pnma$				
Crystal System	Orthorhombic				
Z	4				
$a(\text{\AA})$	8.2756(3)				
$b(\text{\AA})$	11.6115(4)				
$c(\text{\AA})$	8.0623(3)				
Volume (\AA^3)	721.7(3)				
VSD(mm)	0.124(2)				
GOF	1.182				
Rwp	31.78				
Site	Wyckoff	x	y	z	U_{iso}
Rb1	4c	0.556(2)	0.25	0.513(2)	0.150(7)
Pb1	4b	0.5	0	0	0.066(2)
Br1	4c	-0.017(2)	0.25	0.416(2)	0.122(7)
Br2	8d	0.302(1)	0.0414(8)	0.695(1)	0.115(5)

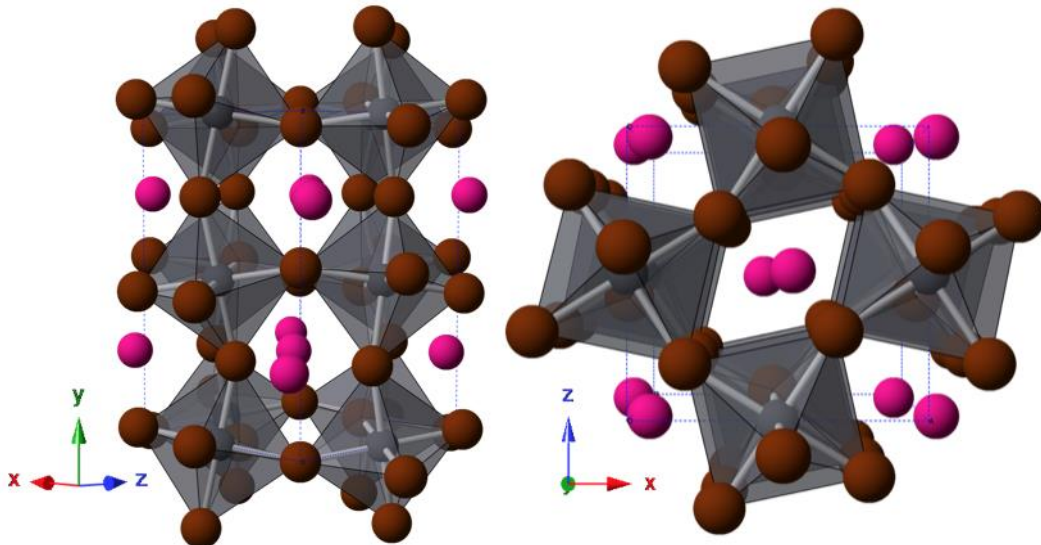


Figure 2.16: Structure of high temperature orthorhombic distorted perovskite RbPbBr_3 (space group $Pnma$). The Br^- , Pb^{2+} , and Rb^+ ions are represented with brown, gray, and magenta spheres, respectively.

The second, and final observed transition occurs around $350\text{ }^\circ\text{C}$ with the orthorhombic perovskite phase transitioning to a higher symmetry, primitive tetragonal perovskite (shown in Figure 2.18) (space group $P4/mbm$). To our knowledge this phase has not been previously described in literature and through refinement process, was discovered to be isostructural with the Cs containing analog (also adopting the $P4/mbm$ perovskite structure) which was crystallographically characterized by Rodova et al.²⁵ The refined XRD pattern at $350\text{ }^\circ\text{C}$ is shown in Figure 2.17. Issues in fitting the intensities at higher 2θ values are attributed to the doming of the sample, which is expressed in the large VSD, and thermal expansion. The only octahedral tilting that contributes to the distorted structure is an in-phase tilt about the [001] direction, tilt system $a^0a^0c^+$. Since the stability and decomposition points for the high temperature phases were unknown, the last scan taken for RbPbBr_3 was at $350\text{ }^\circ\text{C}$ in order to prevent the sample from

melting inside the diffractometer. If the temperature was increased further, it is not unreasonable for the compound to undergo one last phase transition to the ideal perovskite structure $Pm\bar{3}m$ ($a^0a^0a^0$). Structural refinement information for the tetragonal high temperature phase of RbPbBr_3 is shown in Table 2.9.

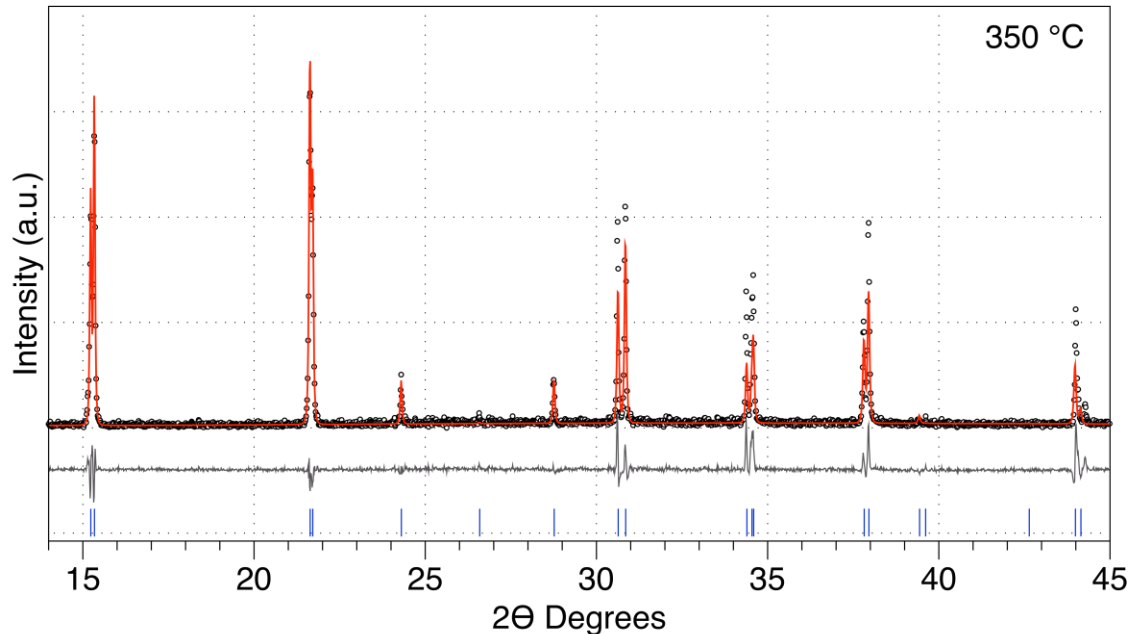


Figure 2.17: Rietveld refined XRD of tetragonal perovskite RbPbBr_3 at $350\text{ }^\circ\text{C}$. Blue markers correspond to RbPbBr_3 perovskite with $P4/mbm$ symmetry.

Table 2.9: Refined lattice parameters and structural information for high temp tetragonal perovskite phase RbPbBr_3

Temp (°C)	350				
Formula	RbPbBr_3				
Space group	$P4/mbm$				
Crystal System	Tetragonal				
Z	4				
$a(\text{\AA})$	8.2162(7)				
$c (\text{\AA})$	5.8503(5)				
Volume (\AA^3)	394.94(8)				
VSD (mm)	0.142(8)				
GOF	1.452				
Rwp	39.068				
Site	Wyckoff	x	y	z	U_{iso}
Rb1	2c	0	0.5	0.5	0.25(1)
Pb1	2a	0	0	0	0.115(4)
Br1	2b	0	0	0.5	0.25(2)
Br2	4g	0.180(3)	0.680(3)	0	0.24(2)

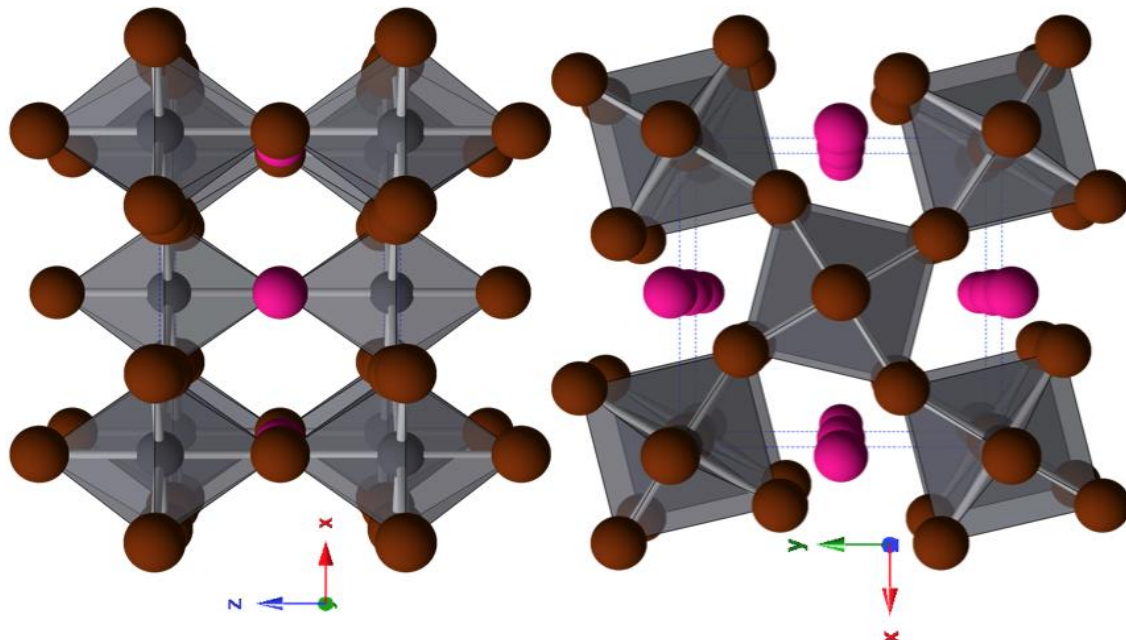


Figure 2.18: Structure of high temperature tetragonal distorted perovskite RbPbBr_3 (space group $P4/mbm$). The Br^- , Pb^{2+} , and Rb^+ ions are represented with brown, gray, and magenta spheres, respectively.

The perovskite structure is characterized by an in-phase tilting ($a^0a^0c^+$) of the Pb^{2+} octahedra in the ab plane of the unit cell. The Pb^{2+} octahedra are surrounded by four equatorial Br atoms at a distance of 3.02(2) Å and two axial atoms at a distance of 2.9252(3) Å, with a Pb–Br–Pb angle of 148.7(9) °. These values are in close relation with values reported in literature, with the exception of the bond angle which is expected to be smaller as a result of the smaller Rb^+ A-site cation.²⁵

2.3.4 RbPbI₃

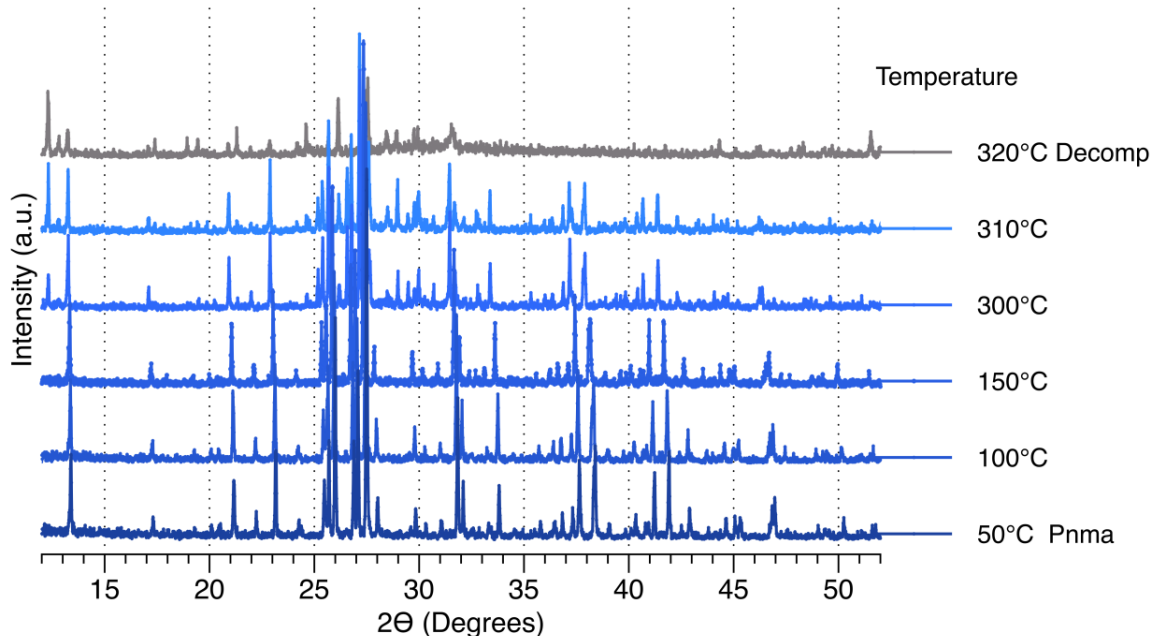


Figure 2.19: Collected diffractograms from the RbPbI₃ variable temperature experiment.

Although high-resolution variable temperature studies of RbPbI₃ had already been performed by Trots and Myagkota¹², RbPbI₃ was still included in this experiment to serve

as a means of comparison to the other rubidium lead halides. Scans from the variable temperature experiment are shown in Figure 2.19. Results and structural data obtained from the variable temperature experiment are consistent with reported literature values with no anomalous findings. It is important to note that at 300 °C the diffraction pattern changes slightly, which could indicate the start of the decomposition of the compound. Trots and Myagkota, who reported RbPbI₃ to have the same phase up until its decomposition, did not mention this change in the pattern. RbPbI₃ adopts a non-perovskite orthorhombic crystal symmetry (space group *Pnma*), NH₄CdCl₃ structure type, and does not undergo any phase transitions before it decomposes around 320 °C. Detailed, high resolution structural information can be found in literature.¹²

2.3.5 Compound Colors

During experimentation, a color change was observed when transitioning from the room temperature non-perovskite phases to the higher temperature perovskite phases. Shown in Figure 2.20 are the compound colors at room temperature and their colors at high temperature slightly above final perovskite transition temperature. All of the compounds that were a non-perovskite at room temperature and perovskite at higher temperatures were accompanied by a color and band gap change upon the transition. CsPbI₃ was included in the table to illustrate how dramatically the band gap drops once it reaches the cubic phase as well as how the larger size of the Cs⁺ A-site cation helps to

stabilize the overall structure when compared to the compositional analog RbPbI_3 , which does not undergo a phase transition when heated.

COMPOUND	COLOR AT ROOM TEMP	COLOR AT HIGH TEMP
CsPbI_3	Yellow	Black $>350\text{ }^\circ\text{C}$
RbPbCl_3	Bleach/ Crisp White	Yellow/Green $>350\text{ }^\circ\text{C}$
RbPbBr_3	White/ Cream	Bright/Canary Yellow $\sim 350\text{ }^\circ\text{C}$
RbPbI_3	Chalky Yellow	Chalky Yellow $\sim 300\text{ }^\circ\text{C}$

Figure 2.20: Observed colors at room and high temperature for halide compounds, which exist as a non-perovskite at room temperature and transition to a perovskite at high temperature. RbPbI_3 shows no phase transition.

2.4 Discussion

Goldschmidt tolerance factor (t) was used in conjunction with the appropriate Shannon ionic radii in order to predict some of the structural outcomes before experimentation. Compounds with a tolerance factor above 1.0 and below 0.9 are expected to take on a more distorted perovskite structure. Shown in Figure 2.21 is a comprehensive comparison between CsPbX_3 and RbPbX_3 ($\text{X} = \text{Cl}^-$, Br^- , I^-) tolerance factors and their phase changes through a temperature range.

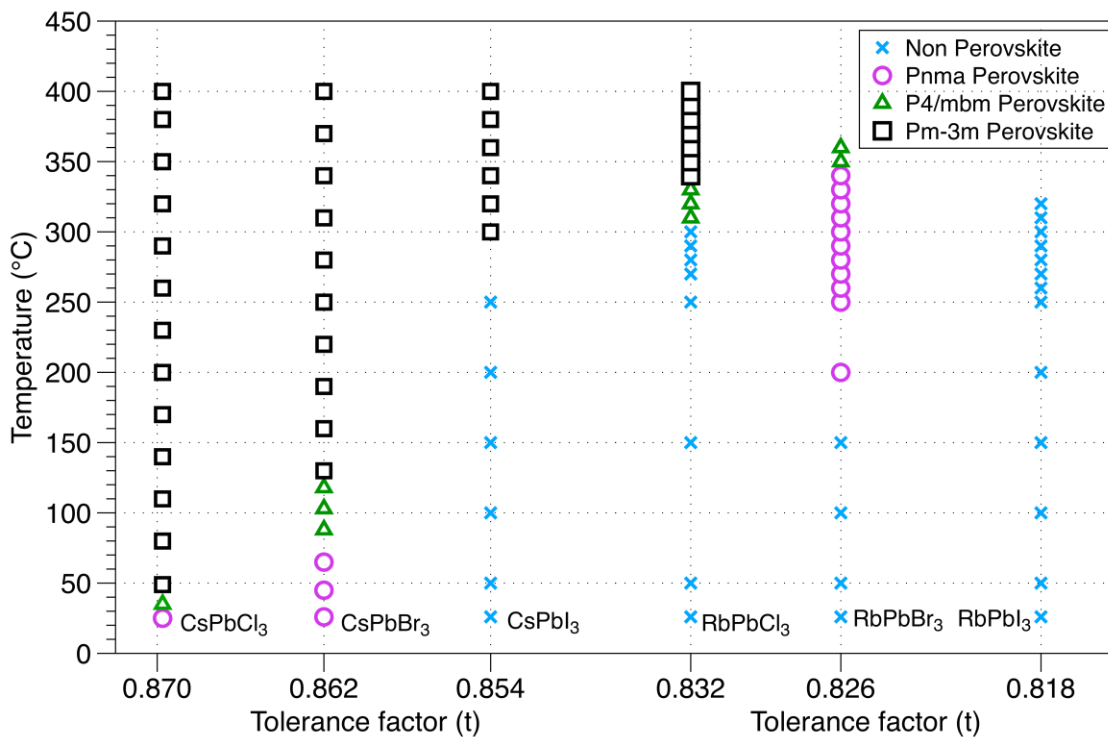


Figure 2.21: Temperature vs. Tolerance factor for compounds CsPbX_3 and RbPbX_3 ($\text{X} = \text{Cl}^-$, Br^- , I^-).

It is evident in the data that below a tolerance factor of approximately $t = 0.86$, the perovskite phase is not stable at room temperature. However, for those compounds with tolerance factors between 0.82 and 0.86, a transformation to the perovskite structure is observed on heating. With little being known about halide perovskites, understanding their structure and how it changes with substitutions is key for the informed development of functional materials. By making changes to the tolerance factor through variation of the halide and the A-site cation respectively, we were able elucidate the range of perovskite formation as well as identify factors responsible for the lack of perovskite formation as t decreases.

Strictly comparing the changes observed by changing the halides between the Cs^+ and Rb^+ derivatives, it becomes obvious that some halides favor the perovskite structure more than others. In general, it was observed that when trying to create a room temperature perovskite, Cl^- and Br^- were more favorable than I^- , which the tolerance factor predicts. It was also observed that compounds that contained Cl^- and Br^- generally had higher melting and decomposition points than did the I^- analogs. This difference in stability seen in the halides is also observed in the organic/inorganic $\text{CH}_3\text{NH}_3\text{PbX}_3$ ($\text{X} = \text{Cl}^-, \text{Br}^-, \text{I}^-$) perovskites, where I^- is the least stable of the analogs.²⁶ The compound color and its subsequent band gap are also governed, to an extent, by the halide used. As you move down the halide group, the perovskites that form have increasingly smaller band gaps.

Substituting Rb^+ for the larger Cs^+ cation results in a decrease in the tolerance factor due to the greater mismatch in size between the A-site and X-site in the AMX_3

perovskite framework. This destabilizes the perovskites structure leading to the formation of competing structure types at room temperature. At higher temperatures Rb^+ compounds containing the halide Cl^- or Br^- transform to perovskite phases, much like CsPbI_3 .

As confirmed by synchrotron diffraction measurements, room temperature CsPbCl_3 crystallizes in the distorted perovskite symmetry (space group *Pnma*) but is rather pseudosymmetric with the distorted tetragonal perovskite (space group *P4/mbm*). The high temperature phase transitions have been previously reported¹⁵ and starts at 37 °C with the transition to the tetragonal perovskite *P4/mbm* ($a^0a^0c^+$) achieving completion at 42 °C. At 47 °C the structure undergoes its second phase transition to ideal cubic perovskite *Pm\bar{3}m* ($a^0a^0a^0$).¹⁵ Our work confirms the centrosymmetric orthorhombic perovskite symmetry at room temperature, which was first reported by Hirotsu *et al.* in 1971. The work conducted here refutes the previous room temperature assignments made by Moller¹³ and Nitsch¹⁴.

During the variable temperature experiments, RbPbCl_3 transforms to a tetragonal perovskite structure, which lasted about 30 °C before the transition to the ideal cubic perovskite phase *Pm\bar{3}m*. Branching of the perovskite lattice parameters for RbPbCl_3 were determined and are plotted as a function of temperature (Figure 2.22). It is plausible that the first perovskite phase transition that appears would be of the orthorhombic symmetry based on the phase transition data for CsPbCl_3 . However, within the error bars of the experiment we were not able to distinguish the subtle difference in *a* and *b* parameters of

the orthorhombic cell, nor were we able to resolve any superstructure reflections pertaining to that symmetry.

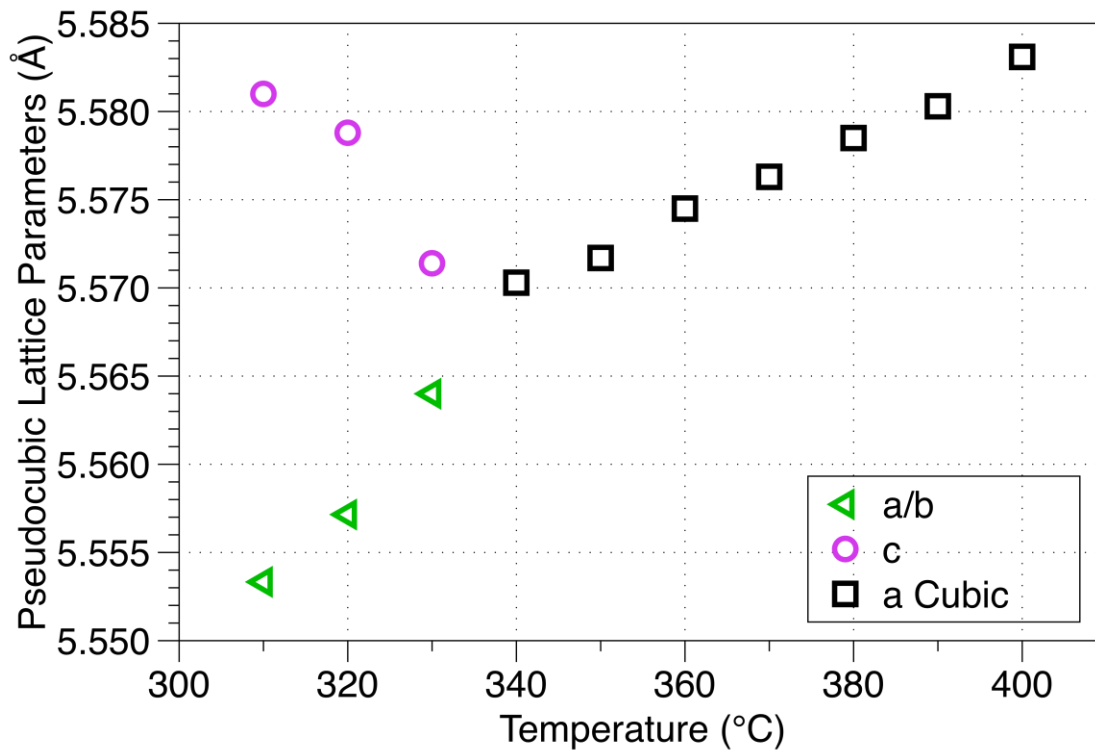


Figure 2.22: Branching of the lattice parameters for RbPbCl_3 ; observed as a function of temperature.

Like the Cl^- compounds, RbPbBr_3 undergoes the same phase transitions as observed in CsPbBr_3 through the temperature range collected. Branching of the lattice parameters for the perovskite phase transitions in RbPbBr_3 were plotted with respect to increasing temperature to further illustrate relationships within the transitions (Figure 2.23). In order to better represent the changes in the unit cell of RbPbBr_3 along the crystallographic c axis, the space group $Pnma$ was transformed to the non-standard

setting $Pbnm$, which was accomplished by a simple rearrangement of the crystallographic axis. Interestingly, RbPbBr_3 transitions to a perovskite before RbPbCl_3 , which is not consistent with a tolerance factor argument. It's worth noting that the competing phases are different in the chloride case than they are for bromide and iodide analogs. For RbPbI_3 and RbPbBr_3 (CsPbI_3) the NH_4CdCl_3 polymorph is more stable than the perovskite polymorph at room temperature, while for RbPbCl_3 no phase with that stoichiometry is stable at room temperature. Instead a two-phase mixture of $\text{Rb}_6\text{Pb}_5\text{Cl}_{16}$ and RbPb_2Cl_5 is observed. It's not unreasonable to expect that more thermal energy is needed to convert a two phase sample into a single phase perovskite in the chloride system, than it takes to trigger a rearrangement from one polymorph to the other in the bromide system.

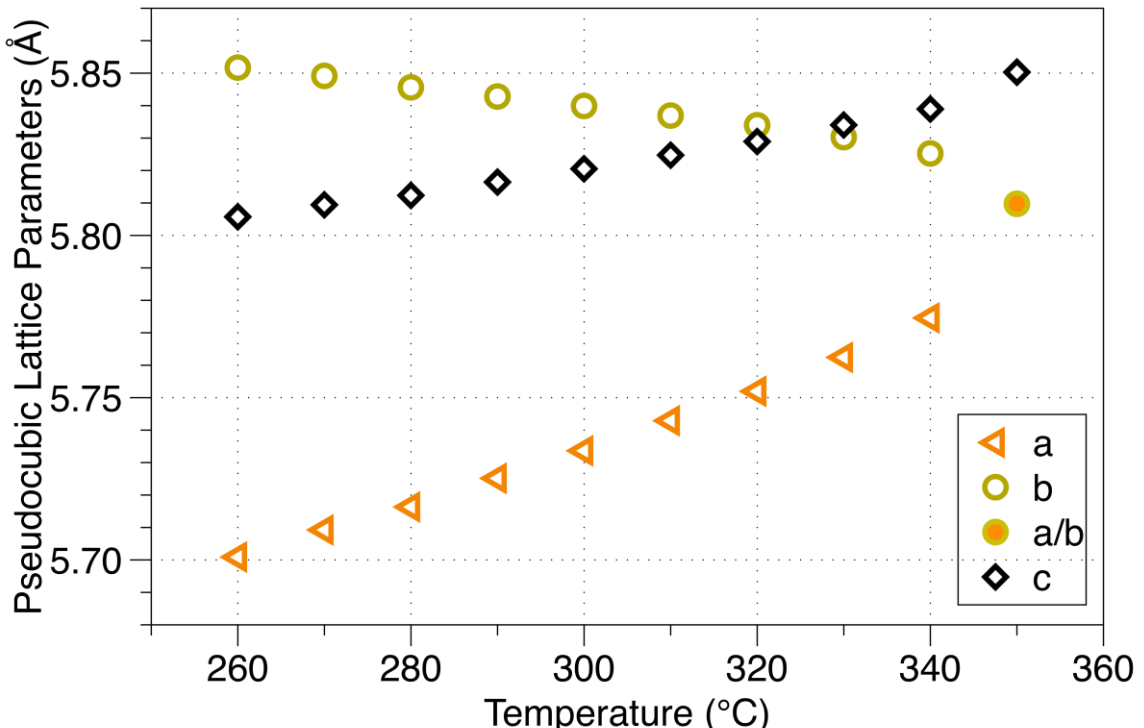


Figure 2.23: Branching of the perovskite lattice parameters for RbPbBr_3 as a function of temperature. Points at 350 °C correspond to distorted perovskite (space group $P4/\text{mbm}$) while all other points correspond to the distorted perovskite ($Pnma$).

One of the aspects of conducting the variable temperature experiments was to investigate how the Pb^{2+} octahedra rearrange themselves on a phase transition. In order to deduce whether the octahedron was acting as a rigid body and simply tilting or whether atom distances were changing, the bond distances between Pb^{2+} and the coordinating halides were calculated to see if there was any variation in distances between perovskite phase transitions.

The first phase transition in RbPbCl_3 is to a tetragonal perovskite which has a slightly distorted Pb^{2+} octahedra with four equatorial Cl^- atoms at a distance of 2.805(39) Å, and two axial Cl^- atoms at a distance of 2.7895(1) Å. In comparing that to the six Cl^-

distances at 2.7859(2) Å seen in the ideal perovskite $Pm\bar{3}m$, it is apparent that the differences in value between the tetragonal distances and the cubic distances are minor, the equatorial atoms being within error. From this, we can predict that the greatest contributing factor to the phase transitions is the tilting of rigid Pb^{2+} octahedra rather than displacements of the halide around a fixed Pb^{2+} site.

$RbPbBr_3$ undergoes a transition from the $Pnma$ perovskite structure to the tetragonal $P4/mbm$ perovskite at higher temperatures. The $Pnma$ phase has two sets of equatorial atoms at 2.981(9) Å and 3.008(9), and two axial Br^- atoms at 2.986(3) Å. The tetragonal $P4/mbm$ phase has four equatorial Br^- atoms at 2.988(14) Å, and two axial Br atoms at 2.9348(2) Å. The distances observed in the tetragonal phase are close enough and within error, that the same conclusions may be drawn as in the case with $RbPbCl_3$, in that the phase transitions are a result of the octahedron moving as a rigid body, rather than individual atoms changing their distances relative to the Pb^{2+} cation.

Once it was concluded that $RbPbCl_3$ and $RbPbBr_3$ followed the same phase transitions at elevated temperatures to high symmetry perovskite's as the Cs^+ analogs, the next step was to investigate whether it was possible to stabilize the high temperature phases at room temperature and investigate their properties. That is the topic of the next chapter.

Chapter 3

Driving Octahedral Tilting in the Perovskite Structure Through A-site Substitution Using Solid Solutions $\text{Rb}_{(y)}\text{Cs}_{(1-y)}\text{PbX}_3$ ($\text{X} = \text{Cl}^-, \text{Br}^-$)

3.1 Introduction

In order to stabilize a room temperature perovskite using Rb^+ , a substitution of the A-site or the M-site in the AMX_3 perovskite framework would have to be involved in order to increase the tolerance factor enough to favor a room temperature perovskite phase. Sn^{2+} and Ge^{2+} were entertained as possible replacements for the M-site, however, they proved to be much too air sensitive. Given the performance of the Cs^+ analogs, it was decided to investigate whether Rb^+ could be incrementally doped into the CsPbX_3 compounds while still maintaining a perovskite structure. Using solid solutions of the formula $\text{Rb}_{(y)}\text{Cs}_{(1-y)}\text{PbX}_3$ ($\text{X} = \text{Cl}^-$ and Br^-) we sought to observe where the Rb^+ substitution limit is before the structure no longer exists as a perovskite. This information will allow us to estimate the tolerance factor at which the perovskite structure is no

longer stable at room temperature. The expected room temperature phase of the solid solutions is the distorted perovskite space group *Pnma* ($a^-b^+a^-$) based on the room temperature crystal structure of CsPbBr_3 and CsPbCl_3 . By incrementally increasing the Rb^+ to Cs^+ ratio, the tolerance factor (*t*) will decrease, which should induce greater octahedral tilting in order for the compound to maintain the perovskite framework. Both CsPbBr_3 ³ and CsPbCl_3 ²⁷ have been previously identified as semiconductors with a direct band gap, the greater octahedral tilting should also have an effect on the resulting band gap, which will be measured. Using substitution of the A-site cation as a means to chemically control the compounds band gap, could have practical applications, especially in situations where a specific band gap is desired.

3.2 Experimental Section

Polycrystalline samples of $\text{Rb}_{(x)}\text{Cs}_{(1-x)}\text{PbX}_3$ (X=Cl, Br) were synthesized by solid state reaction at elevated temperatures. Reagents used were PbBr_2 (98+, Alfa Aesar), PbCl_2 (99+, J.T. Baker Chemical Co.), RbCl (99%, Alfa Aesar), RbBr (99.8%, Alfa Aesar), CsI (99.9%, Sigma Aldrich), PbI_2 (99.999+, Sigma Aldrich). Precursors CsCl and CsBr were synthesized in bulk by neutralizing concentrated HCl (concentrated, Fisher Scientific) or HBr (Purum p.a. \geq 48%, Fluka) with Cs_2CO_3 (99+, Strem Chemicals). The neutralization results in the precipitation of $\text{CsCl}_{(s)}$ / $\text{CsBr}_{(s)}$, which was

then vacuum filtered and washed thoroughly with cold ethanol. XRD was taken to confirm phase purity of precipitated precursors. Reagents were combined in stoichiometric amounts and then ground using an agate mortar and pestle. Every gram of product equates to 15 minutes of grinding and scales up 15min for every additional gram. After grinding, the mixture was transferred to a 25 ml alumina crucible and placed in a box furnace to react for 20 hours at 425 °C. If the resulting product was not phase pure at the end of the cycle, an additional cycle of grinding and second heating was employed.

UV-Vis diffuse reflectance data was collected over the spectral range of 200-1100 nm with an Ocean Optics USB4000 spectrometer equipped with a Toshiba TCD1304AP (3648-element linear silicon CCD array). The spectrometer was used in conjunction with an Ocean Optics DH-2000-BAL deuterium and halogen UV-Vis-NIR light source and a 400 μ m R400-7-ANGLE-VIS reflectance probe.

The phase purity of the samples was checked using both a Rigaku Miniflex diffractometer and Bruker D8 advance diffractometer (40 kV, 50 mA) equipped with a Lynx Eye position sensitive detector and a Ge 111 incident beam monochromator, which selects K α_1 radiation. A scan range of 8-75° 2 θ and a step size of 0.015 were used. Structure refinements were performed with the Rietveld method¹⁹ as implemented in the TOPAS software package.⁷

3.3 Results

3.3.1 Moisture Sensitivity of solid solutions with high Rb⁺ ratios

When CsPbCl₃ and CsPbBr₃ are placed in water both react and hydrolyze into their corresponding reagents. However, this is not a permanent change and can be reversed by simply reheating the compounds as you would to synthesize them. Since the Rb⁺ containing compounds do not form perovskites at room temperature, it was first speculated that the A-site was too small, and, in order to achieve a perovskite structure, the Pb²⁺ octahedra would have to tilt at such extreme angles that it would lead to the breakdown of the octahedral network and the formation of a new phase. Work with solid solutions involving Rb_(x)Cs_(1-x)PbX₃ (X = Cl⁻ and Br⁻) showed that as the Rb⁺/Cs⁺ ratio increased, the stability of the perovskite phase at room temperature decreased. This was specifically apparent in the bright canary yellow Rb_(x)Cs_(1-x)PbBr₃ compounds with higher concentrations of rubidium (x > 0.3). When left exposed to ambient air these compounds would lose their color and become white, which was accompanied by a phase transition to the non-perovskite phase. However, if the compounds were vacuum-sealed in a quartz tube or quickly transferred to a glove box this transition would not occur and the colored perovskite phase would persist. This behavior suggests that moisture catalyzes this phase transition. After the moisture-induced transition to the white non-perovskite phase, all it took to revert back to the colored perovskite was to heat the compounds above 250 °C for a few hours, which presumably drives off the water from

the compound. This air sensitivity became much more pronounced in $\text{Rb}_{(x)}\text{Cs}_{(1-x)}\text{PbX}_3$ samples as the Rb^+ content increased.

3.3.2 $Pnma$ ($a^-b^+a^-$) symmetry perovskites from solid solutions

Substitution of Rb^+ into the pure Cs^+ containing structure was successful and resulted in orthorhombically distorted perovskite structures (space group $Pnma$). Rb^+ was incrementally doped at 10% intervals into the parent structure with the formula CsPbX_3 ($X = \text{Cl}^-$ and Br^-) until the room temperature perovskite structure could no longer be stabilized at room temperature. For the Cl^- containing solutions, Rb^+ was able to be incorporated all the way through an Rb^+ concentration of $x = 0.9$. The Br compounds on the other hand, were only able to incorporate Rb^+ into the structure to a concentration of $x = 0.7$. In both cases, as the ratio of Rb^+/Cs^+ increased, the overall stability of the room temperature perovskite phase decreased. For the $\text{Rb}_{(x)}\text{Cs}_{(1-x)}\text{PbCl}_3$ series with $x = 0.8$ and $x = 0.9$ began to degrade within an hour in ambient laboratory conditions. For the $\text{Rb}_{(x)}\text{Cs}_{(1-x)}\text{PbBr}_3$ series the moisture sensitivity was heightened with Rb -rich samples where $0.7 \leq x \leq 0.9$ transforming to the non-perovskite polymorph in anywhere from a few minutes to a few seconds. As previously mentioned, moisture seems to be responsible for destabilizing the room temperature perovskite phase. If synthesized and kept in a moisture/air free environment, the perovskite phase will persist for an indefinite

amount of time. To illustrate the orthorhombic perovskite *Pnma* phase, a refined pattern from the Cl^- compounds and the Br^- compounds are shown in Figure 3.1 & 3.2 along with the refined structural data in Tables 3.1 & 3.2.

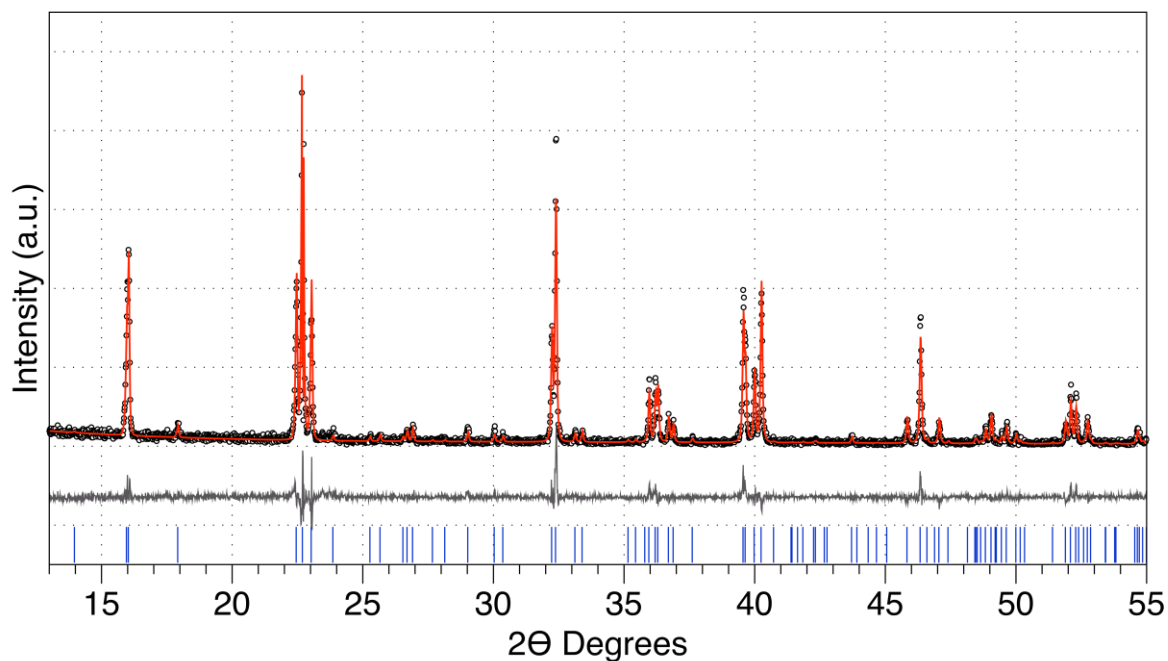


Figure 3.1: Rietveld refined XRD of the room temperature perovskite $\text{Rb}_{0.6}\text{Cs}_{0.4}\text{PbCl}_3$. Bottom tick marks correspond to the orthorhombic distorted perovskite phase, space group *Pnma* ($a^-b^+a^-$)

Table 3.1 Refined structural information and lattice parameters for room temp orthorhombic $\text{Rb}_{0.6}\text{Cs}_{0.4}\text{PbCl}_3$

Formula	$\text{Rb}_{0.6}\text{Cs}_{0.4}\text{PbCl}_3$					
Space Group	<i>Pnma</i>					
Crystal System	Orthorhombic					
<i>Z</i>	4					
<i>a</i> (Å)	7.9138(2)					
<i>b</i> (Å)	11.1017(2)					
<i>c</i> (Å)	7.71693(1)					
Volume (Å ³)	678.21(2)					
<i>GOF</i>	1.172					
<i>Rwp</i>	21.335					
Site	Wyckoff	<i>x</i>	<i>y</i>	<i>z</i>	<i>Occ</i>	<i>U_{iso}</i>
Rb1	4c	0.5462(7)	0.25	0.510(1)	0.6	0.056(3)
Cs1	4c	0.5462(7)	0.25	0.510(1)	0.4	0.056(3)
Pb1	4b	0.5	0	0	1	0.017(1)
Cl1	4c	-0.016(3)	0.25	0.429(2)	1	0.035(8)
Cl2	8d	0.296(2)	0.042(1)	0.700(2)	1	0.041(6)

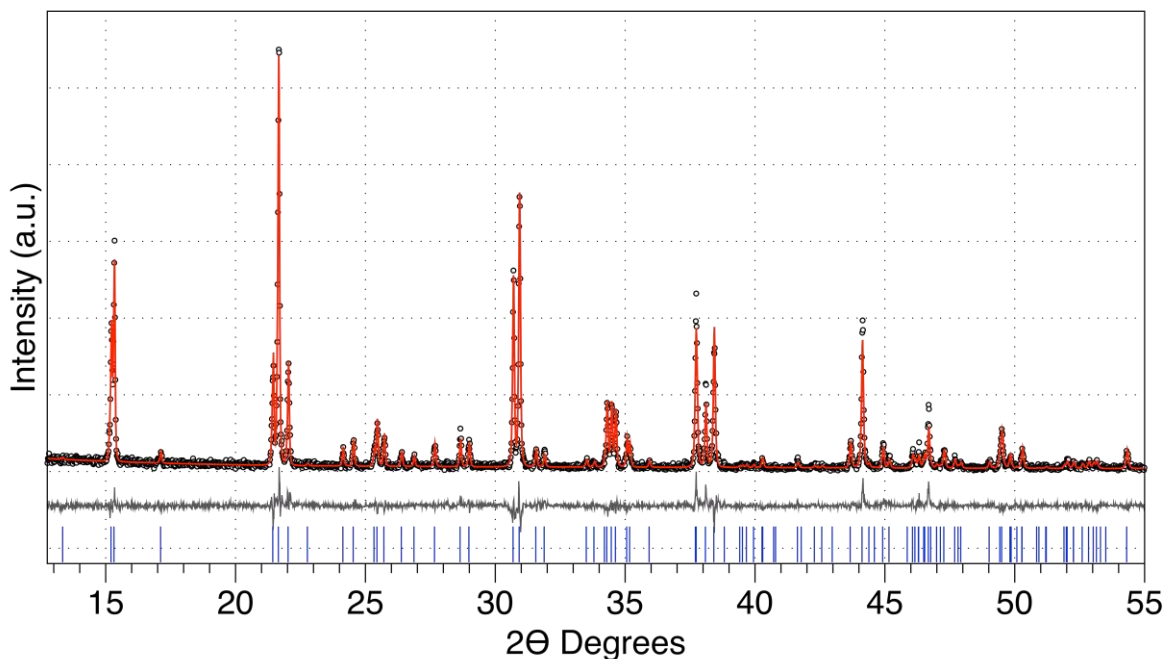


Figure 3.2: Rietveld refined XRD of the room temperature perovskite $\text{Rb}_{0.6}\text{Cs}_{0.4}\text{PbBr}_3$. Bottom tick marks correspond to the orthorhombic distorted perovskite phase, space group *Pnma* ($a^-b^+a^-$).

Table 3.2 Refined structural information and lattice parameters for room temp orthorhombic $\text{Rb}_{0.4}\text{Cs}_{0.6}\text{PbBr}_3$

Formula	$\text{Rb}_{0.4}\text{Cs}_{0.6}\text{PbBr}_3$					
Space group	<i>Pnma</i>					
Crystal System	Orthorhombic					
<i>Z</i>	4					
<i>a</i> (Å)	8.2854(2)					
<i>b</i> (Å)	11.6460(2)					
<i>c</i> (Å)	8.0662(2)					
<i>GOF</i>	1.128					
<i>Rwp</i>	20.915					
Site	Wyckoff	<i>x</i>	<i>y</i>	<i>z</i>	<i>Occ</i>	<i>U_{iso}</i>
Rb1	4c	0.5500(8)	0.25	0.512(1)	0.4	0.079(3)
Cs1	4c	0.5500(8)	0.25	0.512(1)	0.6	0.079(3)
Pb1	4b	0.5	0	0	1	0.027(2)
Br1	4c	-0.013(1)	0.25	0.432(1)	1	0.081(5)
Br2	8d	0.2990(8)	0.0390(6)	0.6974(8)	1	0.059(3)

As was the case with the room temperature phases of compounds CsPbX_3 ($\text{X} = \text{Cl}^-$ and Br^-), the solid solutions adopt an orthorhombic perovskite structure with *Pnma* symmetry. Atomic positions were obtained from the refined parameters of the CsPbBr_3 structure already reported in literature.³ Patterns from solid solutions containing a Br halide show a peak shift to lower 2θ values when compared to the pattern of a Cl^- containing compound; illustrating the increase in d-spacing from the larger Br atom. This type of lattice peak shift is also observed when substituting other atoms in the perovskite structure, and will serve as a means to quantify the extent of Rb^+ substitution from one solid solution to the next.

When dealing with solid solutions there is always question as to the absolute composition of the product. Common indexing and refinement programs such as GSAS

and TOPAS will allow you to refine occupancy of Wyckoff sites in a crystal structure that share different atoms. Since all of the reported compounds underwent refinement of atomic positions, so did the occupancy for the Rb^+/Cs^+ site. While these programs are generally quite accurate in their calculations, there are other ways to confirm proper diffusion of Rb^+ throughout the structure by comparing properties like cell volume and lattice parameters. Shown in Figure 3.3 are the pseudocubic cell volumes for both Cl^- and Br^- solid solutions, both of which follow Vegard's Law.

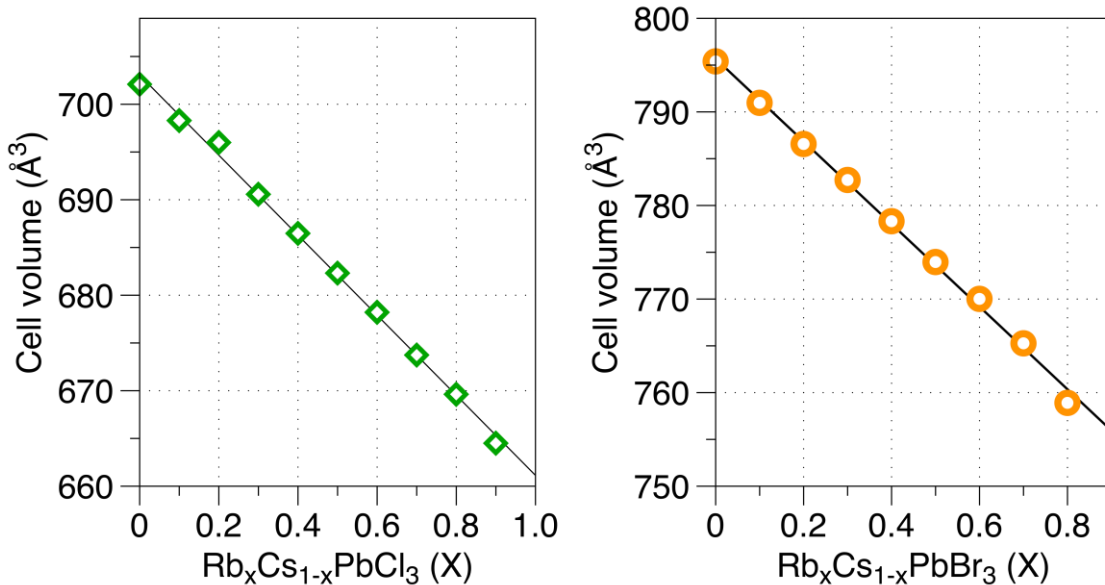


Figure 3.3: Cell volume vs. solid solution for $\text{Rb}_{(x)}\text{Cs}_{(1-x)}\text{PbCl}_3$ (left) and $\text{Rb}_{(x)}\text{Cs}_{(1-x)}\text{PbBr}_3$ (right). Error bars are too small to be observed on the graphs.

If the volume of the unit cell is changing, so are the lattice parameters. Changes in these parameters may yield information on the octahedral tilting as well as help to

identify relative Rb^+ amounts. Shown in Figures 3.4 & 3.5 are the lattice parameters as a function of increasing Rb^+/Cs^+ ratio in the solid solutions for compounds containing Cl^- and Br^- .

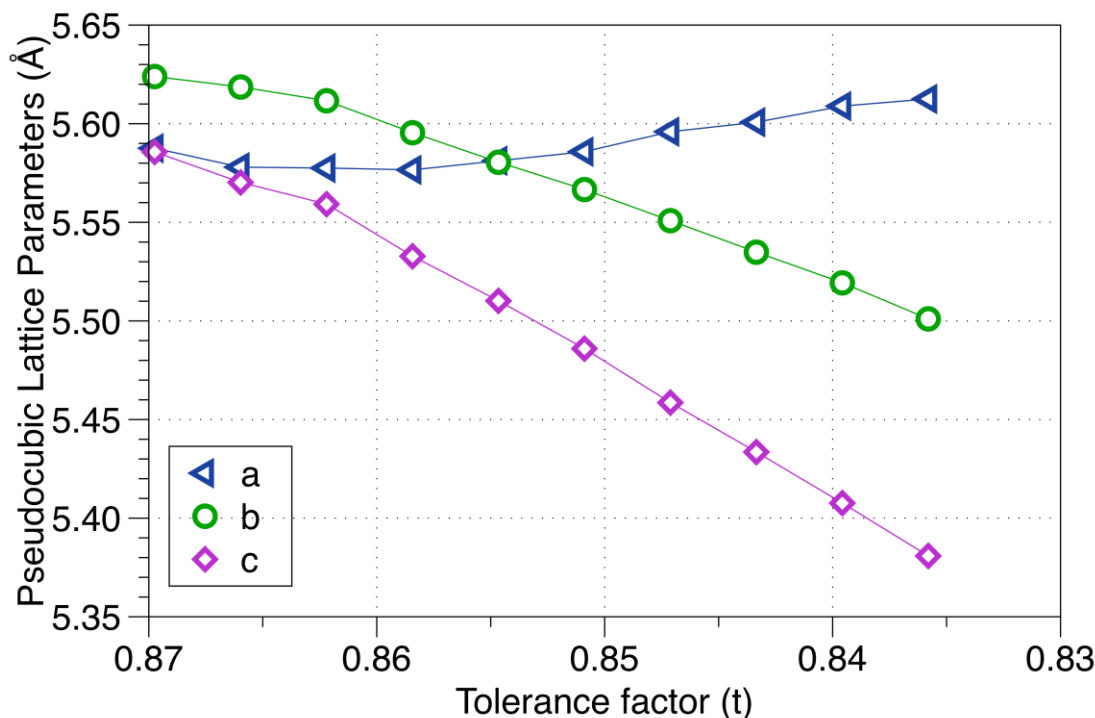


Figure 3.4: Pseudocubic lattice parameters vs. tolerance factor (t) for $\text{Rb}_x\text{Cs}_{(1-x)}\text{PbCl}_3$ $x = 0$ to 0.9 in 0.1 intervals.

A clear trend is observed in that as more Rb^+ is placed into the compound there is a clear splitting of the lattice parameters. This splitting is a direct result of increased octahedral tilting. There are many similarities found in the branching of the lattice parameters between the Cl^- and Br^- containing compounds. In both cases, as more Rb^+ is

added, the magnitude of octahedron tilting increases, this leads to two observable quantities; the a and c parameters ($\sqrt{2}a_p$) begin to diverge with the a axis expanding slightly, while the b and c axes contract. The divergence of a and c marks the separation from a tetragonal symmetry, and a decrease in the b parameter again proves that the incremental additions of Rb^+ are being properly incorporated into the structure. As a result, the overall cell volume is decreasing while the magnitude of octahedral tilting is increasing.

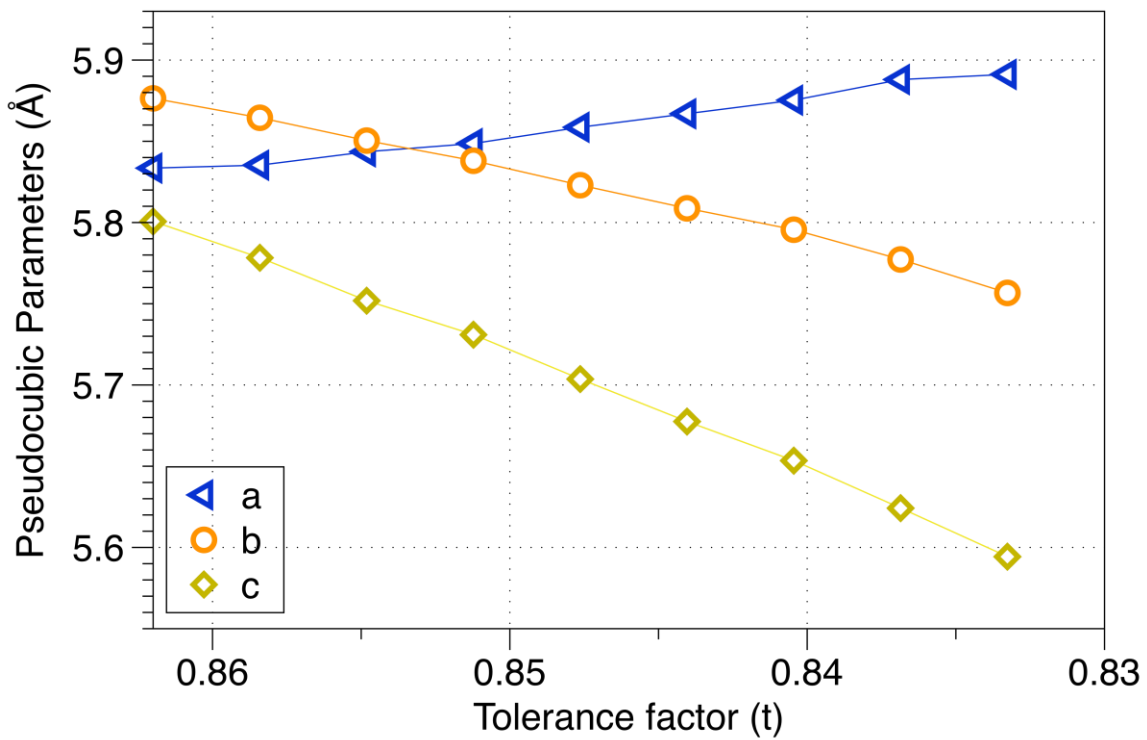


Figure 3.5: Pseudocubic lattice parameters vs. tolerance factor (t) for $\text{Rb}_x\text{Cs}_{(1-x)}\text{PbBr}_3$ $x = 0$ to 0.6 in 0.1 intervals.

3.3.3 Octahedral tilting with increased Rb⁺ substitution

As previously described in Chapter 1, tilting of the octahedra within the perovskite is a means for the structure to distort itself in order to accommodate atomic size mismatches while still maintaining the connected network of corner sharing octahedra. As the octahedral tilting increases so does the splitting of the main diffraction peaks, as described in Chapter 1. Figures 3.6 & 3.7, as well as Figures 3.8 & 3.9 serve to illustrate the increased octahedral tilting as more Rb⁺ is substituted into the structure for Cl⁻ and Br⁻ containing solid solutions.

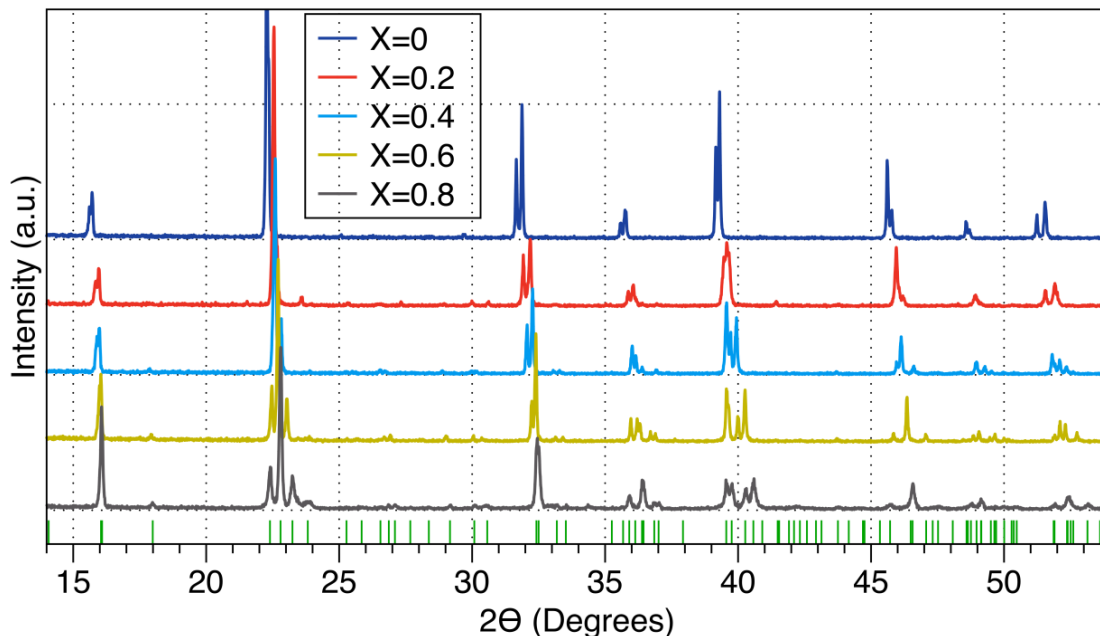


Figure 3.6: X-ray powder diffraction patterns of samples in the $\text{Rb}_{(x)}\text{Cs}_{(1-x)}\text{PbCl}_3$ solid solution. The green markers indicate the reflection positions for the $x = 0.8$ phase.

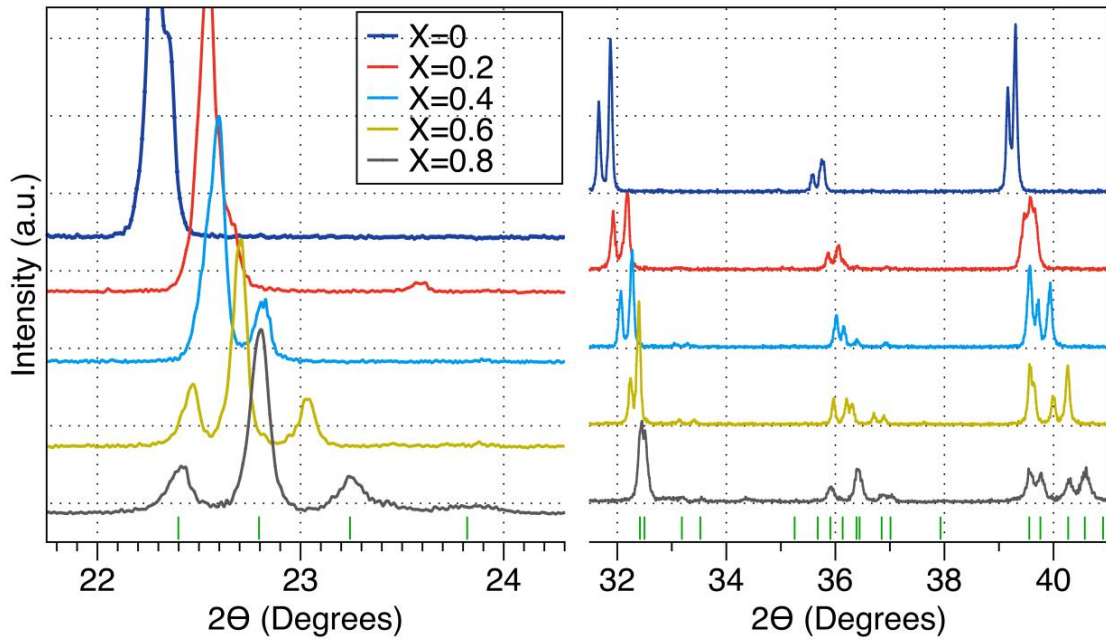


Figure 3.7: Select 2θ ranges from $\text{Rb}_{(x)}\text{Cs}_{(1-x)}\text{PbCl}_3$ diffraction patterns to better illustrate octahedral tilting and subsequent peak splitting as the Rb^+ content increases.

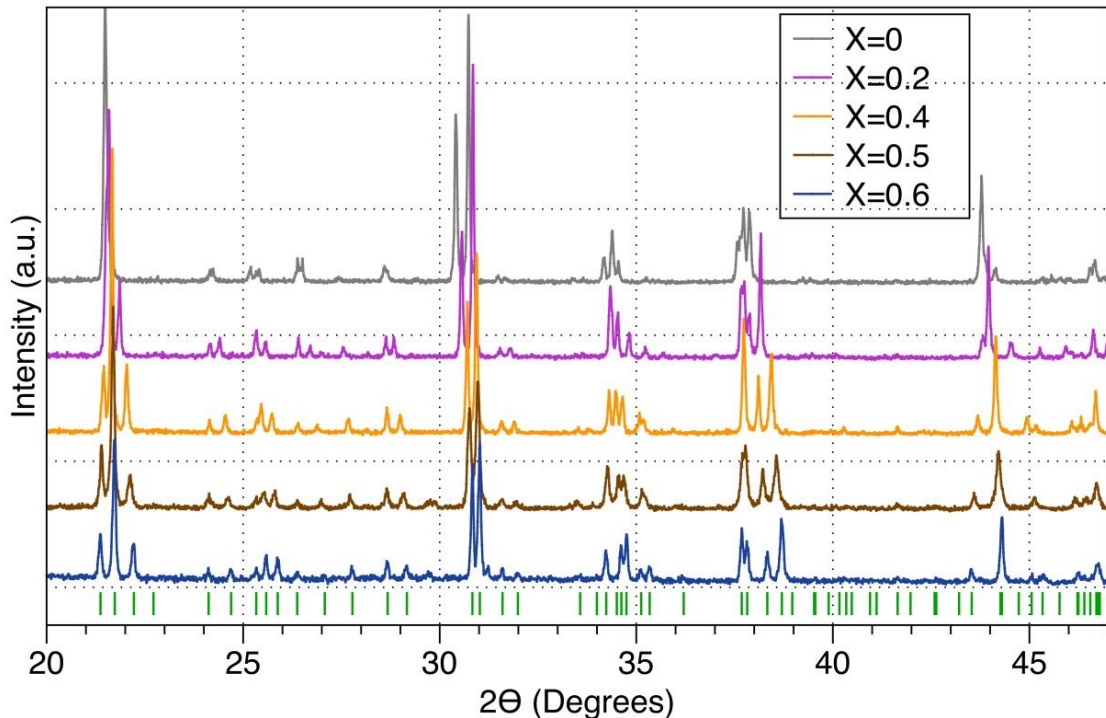


Figure 3.8: X-ray powder diffraction patterns of samples in the $\text{Rb}_{(x)}\text{Cs}_{(1-x)}\text{PbBr}_3$ solid solution. The green markers indicate the reflection positions for the $x = 0.6$ phase.

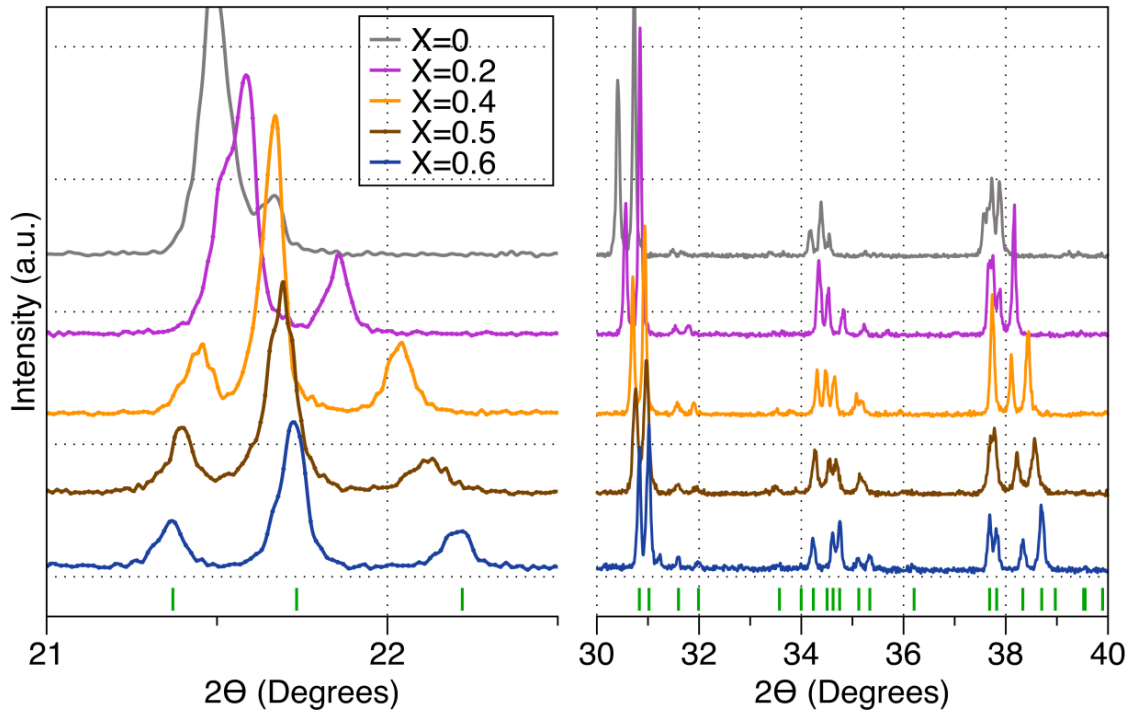


Figure 3.9: Select 2θ ranges from $\text{Rb}_{(x)}\text{Cs}_{(1-x)}\text{PbBr}_3$ diffraction patterns to better illustrate octahedral tilting and subsequent peak splitting as the Rb^+ content increases.

In the above figures, specific 2θ ranges have been enhanced to show the extent of octahedral tilting with increased Rb^+ substitution. What can simply be observed is that as x becomes larger, so does the distances between split peaks. For the solid solutions containing the Cl^- halide, the specific ranges that truly illustrate the difference in splitting are $22-24^\circ$ and $32-41^\circ$. Focusing on the first 2θ range and looking down the graph from $x = 0$ to $x = 0.8$, what appears as a single, shouldered peak at $x = 0$ can be seen to split into three different reflections that follow the characteristic splitting pattern and relative peak intensity for an orthorhombic perovskite described in Chapter 1. The same increase in relative splitting can be seen for the peaks located around $40^\circ 2\theta$, where what appears to be two peaks at $x = 0$ splits further to a point where all four reflections are easily resolved

at $x = 0.8$. This trend in splitting is also observed in the $\text{Rb}_{(x)}\text{Cs}_{(1-x)}\text{PbBr}_3$ solid solutions at slightly lower 2θ values.

3.3.4 Pb–X–Pb ($X = \text{Cl}^-$ and Br^-) bond angles

One of the best ways to quantify the distortion seen in the octahedra is to measure the Pb–X–Pb bond angle as well as the Pb–X distance. The average bond angles obtained from the Rietveld refinements are shown in Figure 3.10 for Cl^- and Br^- solid solutions and Figure 3.11 shows the average bond distances for both solid solutions. All of the bond angles and bond distances in the structure were averaged and error bars calculated accordingly in order to better represent the overall change in the octahedral environment as the level of Rb^+ was increased.

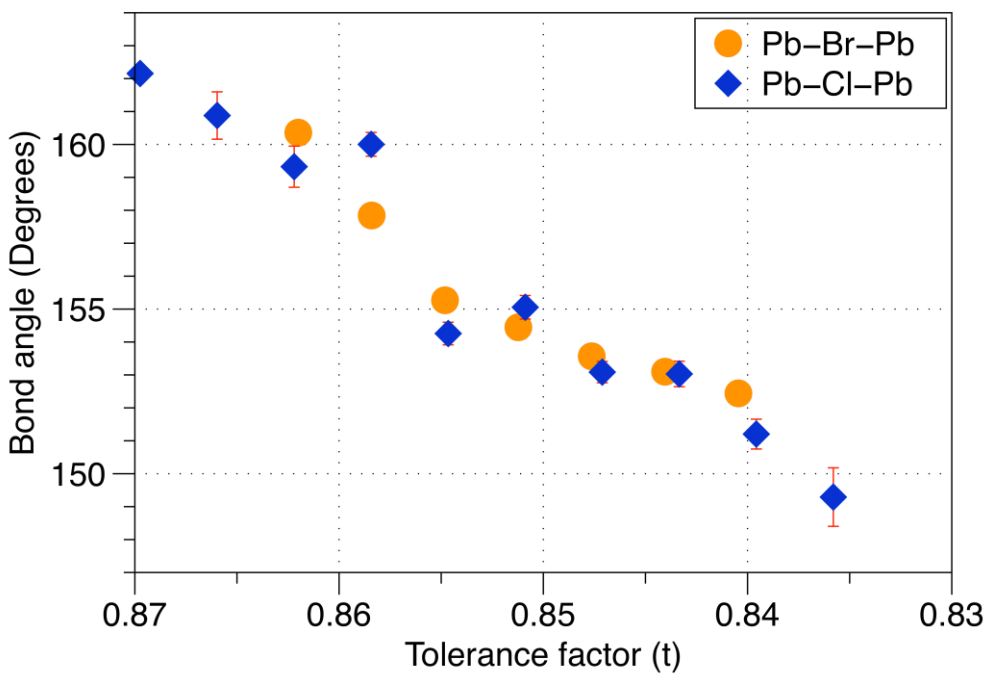


Figure 3.10: Average bond angle vs. Tolerance factor for $\text{Rb}_{(x)}\text{Cs}_{(1-x)}\text{PbX}_3$ ($\text{X} = \text{Cl}^-$ and Br^-) solid solution. $x = 0$ to 0.9 for Cl^- and $x = 0$ to 0.6 for Br^- . Some error bars are smaller than symbols.

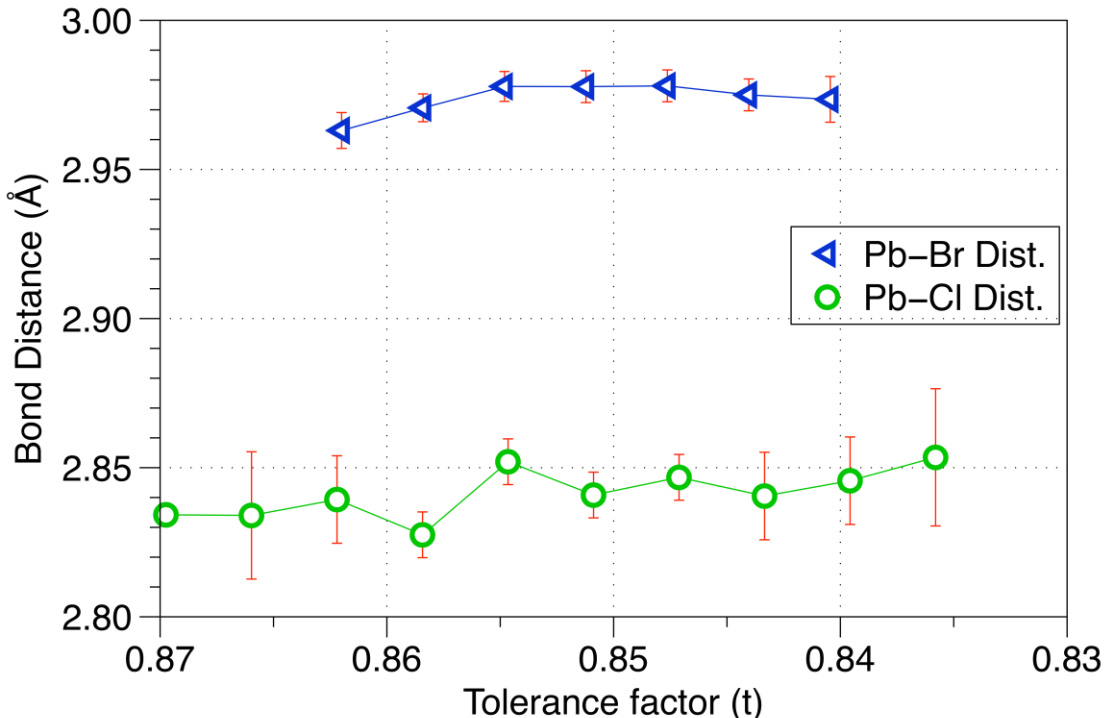


Figure 3.11: Average $\text{Pb}-\text{X}$ bond distance vs. Tolerance factor for $\text{Rb}_{(x)}\text{Cs}_{(1-x)}\text{PbX}_3$ ($\text{X} = \text{Cl}^-$ and Br^-) solid solution. $x = 0$ to 0.9 for Cl^- and $x = 0$ to 0.6 for Br^- . Some error bars are smaller than symbols.

What is observed in the Cl^- and Br^- solid solutions is with increased Rb^+ substitution both the tolerance factor and observed bond angles are decreasing. Since both of the bond angles decrease by about the same value from $x = 0$ to the last synthesized perovskite compound, it appears that the octahedra are tilting in a fairly rigid and uniform manner. Within error of the bond distance graph, the overall change in the $\text{Pb}-\text{X}$ distance is negligible, suggesting that the octahedra distort the structure by tilting in a rigid manner. The bond angles for both Br^- and Cl^- show a relationship with the tolerance factor. As observed on the graph, for any given tolerance factor where both halide perovskites exist their bond angles are extremely close in value. The relationship with bond angle, tolerance factor, and the unchanging bond distances further illustrate that the stability of the solid solution perovskite is dependent on both the tolerance factor and choice of halide. As the size of the halide increases (Cl^- , Br^- , Γ), the tolerance factor decreases as does the amount of Rb^+ that can be substituted into the solid solution.

3.3.5 Band gaps of $\text{Rb}_{(x)}\text{Cs}_{(1-x)}\text{PbX}_3$ compounds ($\text{X} = \text{Cl}^-$ and Br^-)

Once tiling was confirmed in the perovskite structure, attention was turned to investigating how the band gap of the compounds change with greater octahedral tilting distortion. Diffuse reflectance measurements were taken from powdered crystalline samples of the solid solutions, followed by a transformation of the reflectance data using the Tauc method for a direct gap compound to construct a Tauc plot.²⁸ A direct band gap

was selected for the solid solutions based on the sharpness of the reflectance onset and from previous reports confirming CsPbBr_3 as a direct band gap.³ From the plot, a compound's band gap can be determined by applying a linear fit tangent to the inflection point of the curve and then extrapolating the line to the x -axis. Diffuse reflectance and Tauc plots for the $\text{Rb}_{(x)}\text{Cs}_{(1-x)}\text{PbCl}_3$ solid solutions are shown in Figures 3.12 & 3.13, experimentally derived band gaps are shown in Table 3.3. Two features are observed on each of the graphs, one stronger than the other. The first, smaller feature, which occurs at a higher energy, is actually the compounds band gap and the second, stronger feature, is believed to be as a result of a strongly bound exiton which was first reported by C. Stoumpos *et al.* from their experiments with the photoluminescence of CsPbBr_3 .³ Band gap for the $x = 0.6$ sample was unable to be determined due to the large exitonic feature as well as degradation of sample when exposed to the incident light of the spectrometer.

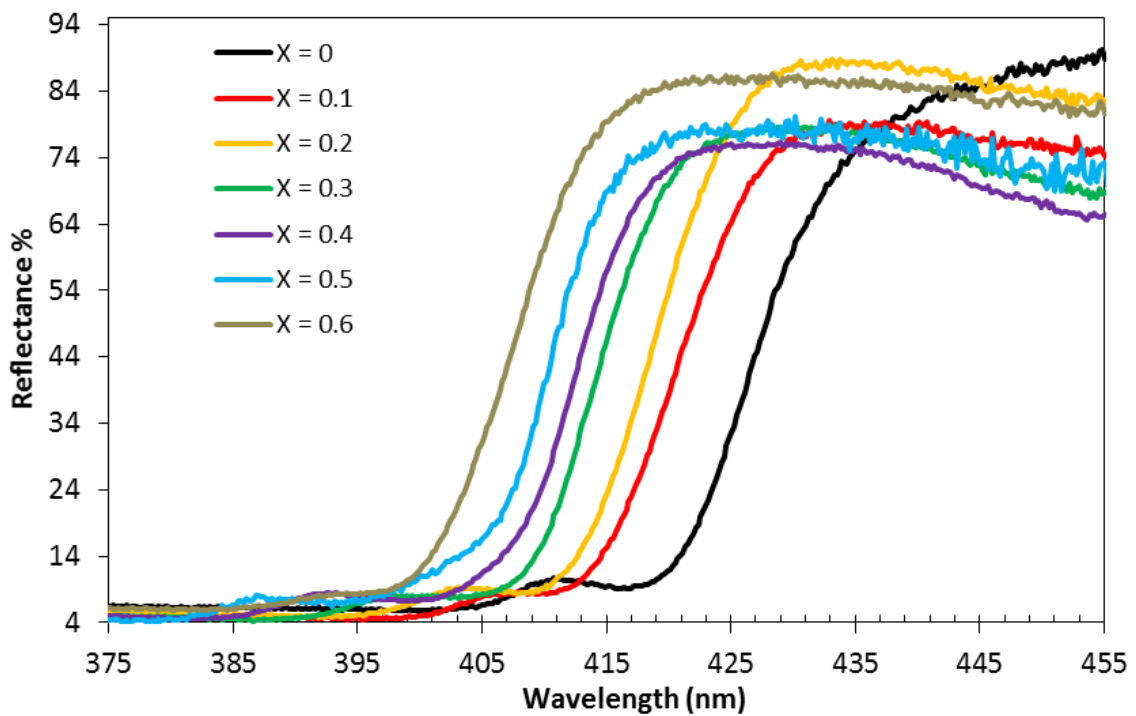


Figure 3.12: Diffuse reflectance overlay for the $\text{Rb}_{(x)}\text{Cs}_{(1-x)}\text{PbCl}_3$ series.

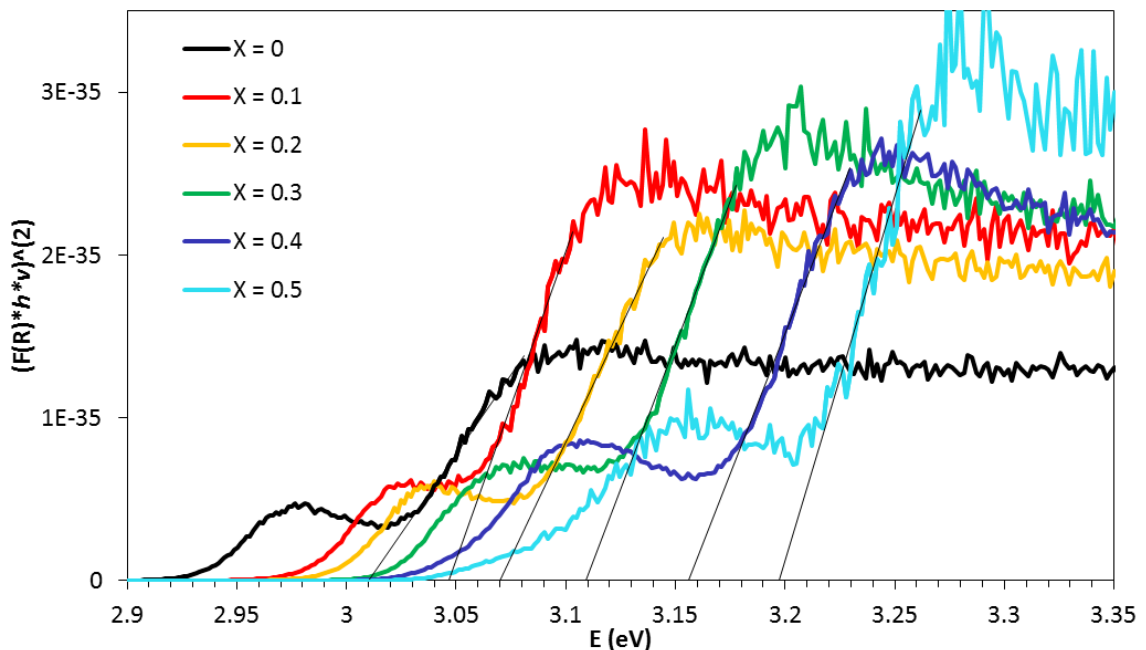


Figure 3.13: $\text{Rb}_{(x)}\text{Cs}_{(1-x)}\text{PbCl}_3$ Tauc Plot. Diffuse reflectance data for the solid solution Cl^- series treated with the Tauc method. A linear fit was applied and extrapolated to the x -axis to elucidate the compounds band gap.

Table 3.3: Derived band gaps using the Tauc method for $\text{Rb}_{(x)}\text{Cs}_{(1-x)}\text{PbCl}_3$ solid solutions

Compound	x = 0	x = 0.1	x = 0.2	x = 0.3	x = 0.4	x = 0.5
eV	3.01(11)	3.05(12)	3.07(6)	3.11(9)	3.16(8)	3.20(12)

As a point of comparison for obtained values, reported literature values for CsPbBr_3 and CsPbCl_3 are 2.25 eV³ and 2.97 eV²⁷. As evidenced by the delayed onset of reflectance in successive solid solutions, the band gap could be tuned by increasing the level of Rb^+ substitution. In the Cl^- containing solid solutions there was a total band gap increase of 0.19 eV. While this value is small, it does illustrate the A-site's ability to alter a given compound's band gap. Results for the $\text{Rb}_{(x)}\text{Cs}_{(1-x)}\text{PbBr}_3$ series of compounds shows very close behavior to that of the Cl^- containing series. Diffuse reflectance and Tauc plots for the $\text{Rb}_{(x)}\text{Cs}_{(1-x)}\text{PbBr}_3$ solid solutions are shown in Figures 3.14 & 3.15, and the experimentally derived band gaps are shown in Table 3.4.

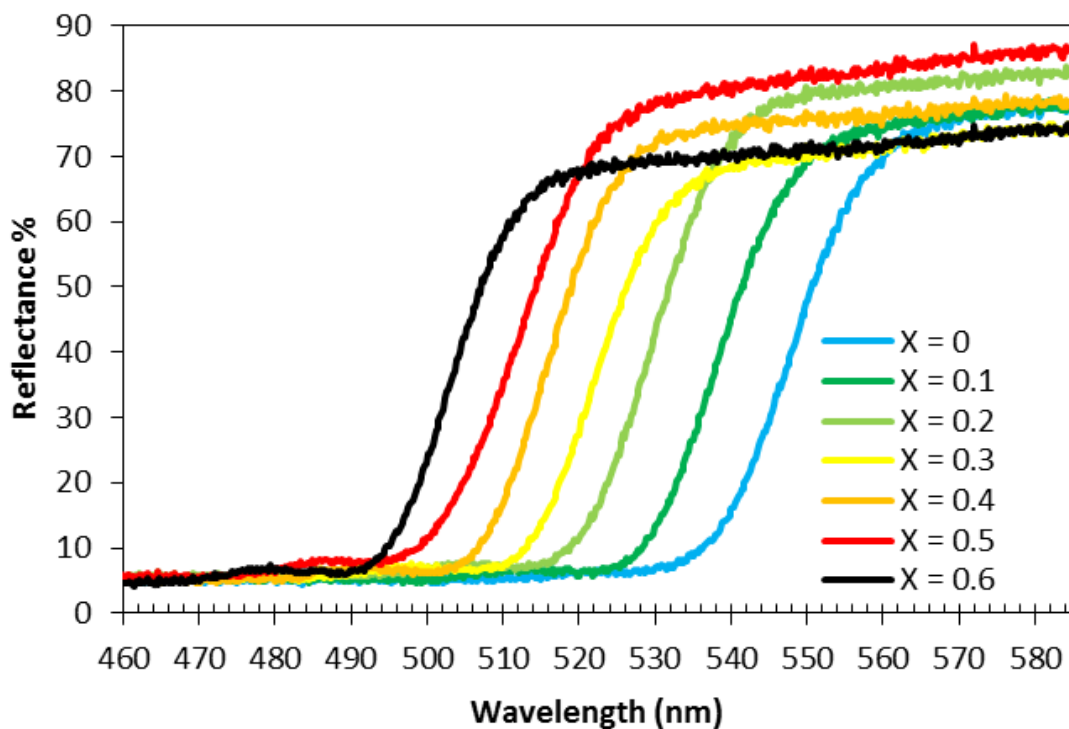


Figure 3.14: Diffuse reflectance overlay for the $\text{Rb}_{(x)}\text{Cs}_{(1-x)}\text{PbBr}_3$ series.

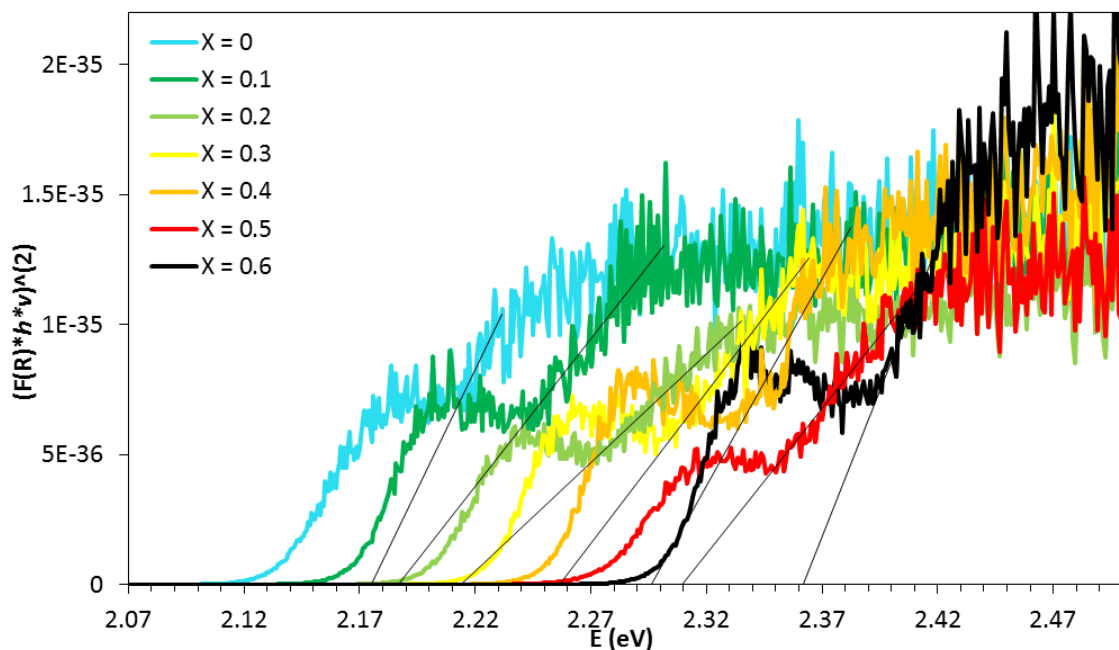


Figure 3.15: $\text{Rb}_{(x)}\text{Cs}_{(1-x)}\text{PbBr}_3$ Tauc Plot Diffuse reflectance data for the solid solution Br^- series treated with the Tauc method. A linear fit was applied and extrapolated to the x -axis to elucidate the compounds band gap.

Table 3.4: Derived band gaps using the Tauc method for $\text{Rb}_{(x)}\text{Cs}_{(1-x)}\text{PbBr}_3$ solid solutions

Compound	x = 0	x = 0.1	x = 0.2	x = 0.3	x = 0.4	x = 0.5	x = 0.6
eV	2.18(23)	2.19(18)	2.21(13)	2.26(20)	2.29(20)	2.31(12)	2.36(15)

The $\text{Rb}_{(x)}\text{Cs}_{(1-x)}\text{PbBr}_3$ series exhibited a similar increase in band gap with a total difference of 0.18 eV. This value is within the calculated error of the Cl^- compounds and concludes that the increase in band gap is about the same in both series. Band gaps for solid solutions that contained an Rb^+ concentration above $x = 0.6$ could not be measured due to the extreme air/moisture sensitivity of the samples. While XRD and structural refinement were able to be performed on $\text{Rb}_{(x)}\text{Cs}_{(1-x)}\text{PbCl}_3$ ($x = 0.6 - 0.9$), diffuse reflectance measurements were not. These compounds showed stability when interacting with the X-rays from the XRD scans, but upon irradiation from the UV-Vis spectrophotometer, the samples would immediately degrade leading to an unreliable diffuse reflectance spectra. As previously mentioned, $\text{Rb}_{(x)}\text{Cs}_{(1-x)}\text{PbBr}_3$ compounds that contained a Rb^+ concentration greater than $x = 0.6$ proved to be too air/moisture sensitive to exist in ambient conditions long enough for a scan to be obtained.

3.4 Discussion

For both solid solutions $\text{Rb}_{(x)}\text{Cs}_{(1-x)}\text{PbCl}_3$ and $\text{Rb}_{(x)}\text{Cs}_{(1-x)}\text{PbBr}_3$, the band gap increases as the degree of octahedral tilting increases. This trend between band gap and

octahedral tilting distortion is also seen in d⁰ transition metal oxide perovskites like SrTiO₃/CaTiO₃ and KTaO₃/NaTaO₃.⁵ In the proceeding section we will compare our results to other oxide perovskite and organic A-site perovskite compounds with similar structure and band gap. In order to better illustrate the degree of octahedral tilting, structural representations of the crystal structures for select solid solutions are shown in Figures 3.16 & 3.17.

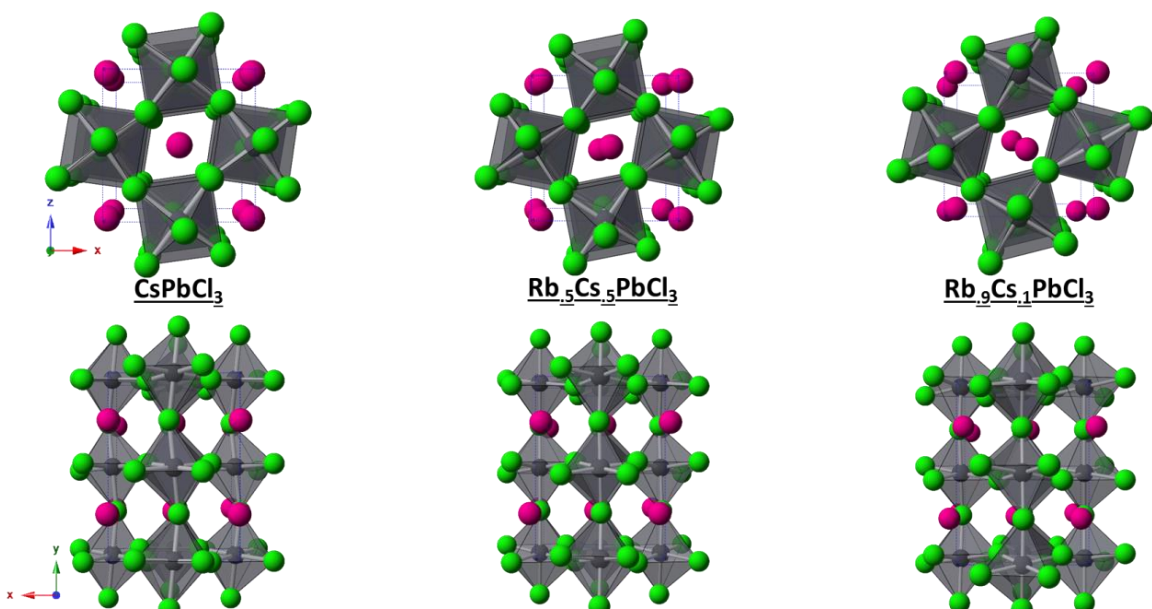


Figure 3.16: Structural representations of the crystal structures of select $\text{Rb}_{(x)}\text{Cs}_{(1-x)}\text{PbCl}_3$ solid solutions to illustrate increased octahedral distortion with increased Rb^+ substitution.

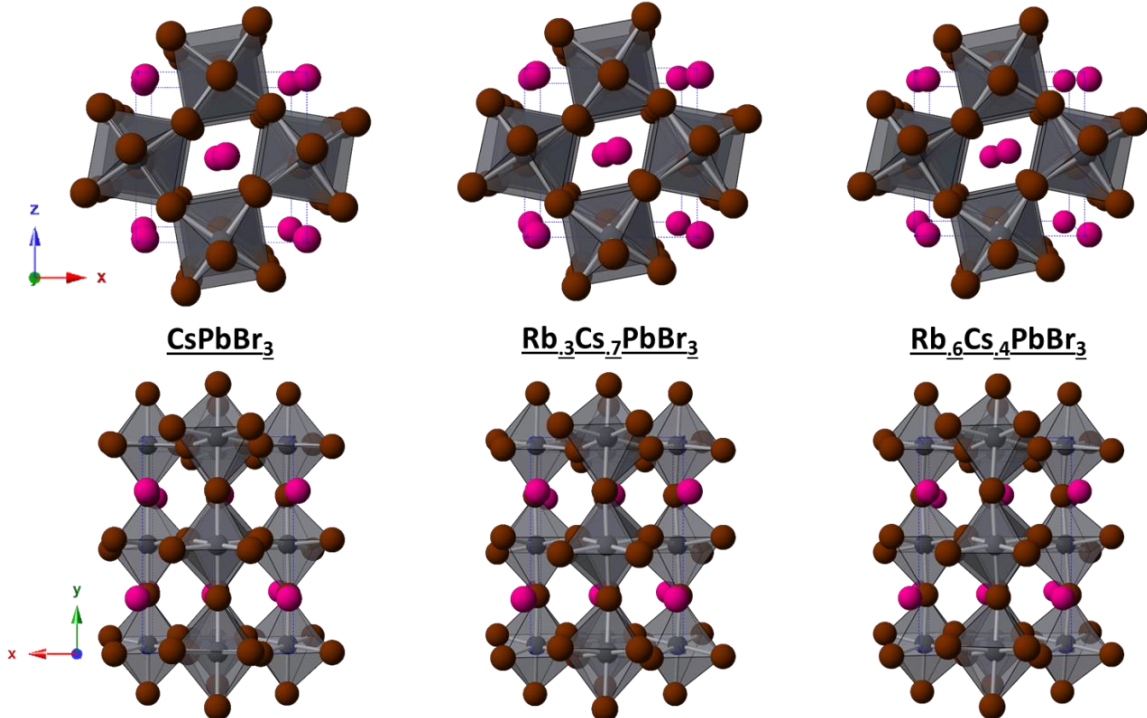


Figure 3.17: Structural representations of the crystal structures of select $\text{Rb}_{(x)}\text{Cs}_{(1-x)}\text{PbBr}_3$ solid solutions to illustrate increased octahedral distortion with increased Rb^+ substitution.

The magnitude of the tilting distortion is viewed best down the y -axis by observing the displacement of the A-site cation through the cell, which correlates directly with the octahedral tilting. The octahedral tilting as well as the band gaps have been characterized for similar perovskite structures. Ternary stannate perovskites ASnO_3 ($\text{A} = \text{Ba, Sr, and Ca}$) crystallize in both $Pm\bar{3}m$ and $Pnma$ perovskite symmetry, and observe octahedral tilting as the A-site becomes smaller. The Sn–O–Sn bond angles, as well as band gap, have been previously reported in literature and are shown in Table 3.4 alongside results from the Rb^+/Cs^+ solid solutions. Also included in the discussion and in Table 3.4 are the methyl ammonium lead halides which typically adopt the ideal perovskite structure $Pm\bar{3}m$ but have been discovered to have similar band gaps to the

distorted perovskites CsPbX_3 ($\text{X} = \text{Cl}^-$ and Br^-) and solid solutions containing Rb^+ . By comparing the tilting and subsequent band gaps of these compounds in relation to the research conducted herein, we hope to gain a greater understanding of how the atoms and their arrangement in the structure affect the electronic and optical properties of the compounds.

Table 3.5: Band gaps and bond angles for $x = 0$ and $x = 0.6$, Cl^- and Br^- solid solutions compared to the same properties of similar perovskite structures with different formulas. (*t*) is absent for the methyl ammonium perovskites as an accurate value cannot be obtained due to the organic A-site cation.

Phase (<i>t</i>)	Symmetry	M–X–M angle (deg)	Band gap (eV)
		Exp	Lit
BaSnO_3^{29} (1.018)	<i>Pm</i> $\bar{3}m$	180	---
SrSnO_3^{30} (0.961)	<i>Pnma</i>	160.5	---
		159.6	4.1 ⁵
CaSnO_3^{31} (0.927)	<i>Pnma</i>	146.7	---
		148.2	4.4 ⁵
CsPbCl_3 (0.870)	<i>Pnma</i>	164.86	3.01(11)
		160.8(2)	2.97 ²⁷
$\text{Rb}_{0.5}\text{Cs}_{0.5}\text{PbCl}_3$ (0.851)	<i>Pnma</i>	157.9	3.20(12)
		153.5(5)	---
CsPbBr_3 (0.862)	<i>Pnma</i>	164.87	2.18(23)
		158.0(3)	2.25 ³
$\text{Rb}_{0.6}\text{Cs}_{0.4}\text{PbBr}_3$ (0.840)	<i>Pnma</i>	154.9	2.36(15)
		151.2(4)	---
$\text{CH}_3\text{NH}_3\text{PbCl}_3$ (n/a)	<i>Pm</i> $\bar{3}m$	180	3.0 ³²
$\text{CH}_3\text{NH}_3\text{PbBr}_3$ (n/a)	<i>Pm</i> $\bar{3}m$	180	2.23 ³³

A trend that is observed across all of the compounds shown in the above table is that as the tolerance factor (t) decreases as the perovskite octahedral network becomes increasingly more distorted. Also, with increased octahedral tilting, evidenced by the decreasing M–X–M bond angles, the band gap of the compound also increases. Since the ASnO_3 perovskites do not have any of the same atoms in the structure, we can expect different contributing orbitals to the valence and conduction bands of these compounds, leading to a different band structure than is observed in the solid solutions of $\text{Rb}_{(x)}\text{Cs}_{(1-x)}\text{PbX}_3$ and methyl ammonium perovskites. Substituting the A-site of the ASnO_3 perovskites from Ba^{2+} to Sr^{2+} initially leads to a fairly large increase of 1 eV in the band gap, but, upon another substitution, the band gap only increases by 0.3 eV. The same trend that was observed in the band gap is also observed in the bond angles, with the first substitution resulting in the largest decrease in the bond angles. In both the Cl^- and Br^- solid solutions the bond angles were in close agreement with each other for solid solutions with similar tolerance factors but the resulting band gap differed based on the halide species. Each substitution of the ASnO_3 perovskites resulted in a tolerance factor drop of about $(t) = 0.05$ which seems to be disconnected slightly from the bond angles, as they do not decrease in a uniform manner. The increase in band gap, however, does follow the magnitude in tilting distortion from the cubic BaSnO_3 to the distorted CaSnO_3 . The second A-site substitution is a more realistic comparison to the halide compounds because the bond angles are going from a bent to a more severely bent position. In the oxide perovskites a $\sim 12^\circ$ decrease in bonding angle was accompanied by a 0.3 eV increase in the band gap where in the inorganic halide containing compounds an average

decrease in bond angle by $\sim 8.4^\circ$ is accompanied by a 0.185 eV increase in band gap. In both cases when the starting compound already had bent bond angles further substitution to decrease the angles resulted in a very small increase in band gap. The largest spike in band gap is observed in the first substitution of the oxide perovskites where the bond angle changes from a straight 180° to about 160° .

In the $\text{Rb}_{(x)}\text{Cs}_{(1-x)}\text{PbX}_3$ compounds the tolerance factor drops by about 0.023 between $x = 0$ and $x = 0.6$ and the bond angles drop by roughly 8.4° . Based on experimental results, for a given tolerance factor where both Cl^- and Br^- solid solutions exist we can expect the M–X–M bond angles to be about the same value but the band gaps differ as a result of the slightly elevated valence band when going from the Cl^- to Br^- halide. This elevation in the valence band increases as you travel down the halide group and is a direct result of increasing energy in the p-orbital valence electrons which comprise most of the valence band in the perovskite band structure. Here exists a disconnect in the trend between tolerance factor, M–X–M bond angles, and resulting band gap between the oxide perovskites and the halide perovskites. The oxide perovskite band structure behaves differently than the halide containing compounds when they undergo tilting distortions of the octahedra. Knowing and understanding this difference will prove valuable in the synthesis and construction of optimized functional materials employing the perovskite framework for its band gap and electron transport properties.

Another interesting comparison we will make is the similarity in band gaps between the methyl ammonium lead halides and the $\text{Rb}_{(x)}\text{Cs}_{(1-x)}\text{PbX}_3$ solid solutions. The only real difference between these compounds is their symmetry and A-site cation. There

has been some work in regards to identifying an absolute radius for the organic A-site in the methyl ammonium perovskites, but results are highly inconclusive, therefore tolerance factors cannot be precisely calculated, but rather, can be roughly estimated based on the resulting symmetry of the compound. Since both methyl ammonium lead halides adopt a cubic perovskite structure, it is assumed that the effective radius of the methyl ammonium cation is similar to the Cs^+ cation, but slightly larger. The similarities in the band gap could be a direct result of the A-site organic cation and the manner by which it coordinates to other ions in the crystal structure. Since the methyl ammonium cation is a molecule with a small dipole moment it is unreasonable to suggest that it will have cuboctahedral coordination environment where it can equally share its charge with all twelve halides. Instead, the methyl ammonium cation will bond more strongly to some halides than others, thus changing its position from being centered in the cell to being dislocated slightly in any of the directional axis. Since powder diffraction essentially takes an average of many cells, the observed crystal structure is the ideal cubic perovskite structure, when in reality the crystal structure is more fluid, changing from cell to cell.

3.5 Conclusion

The results presented in this chapter show that the band gaps of the lead halide perovskites and solid solutions depend on the degree of distortion brought about by the substitution of a smaller A-site cation (reducing the tolerance factor) as well as choice of

halide. Shown in Figure 3.18 is an extension of Figure 2.14 that includes the room temperature stabilized solid solution perovskites. As evidenced in the figure it becomes clear that the stability of the perovskite structure isn't completely dependent on tolerance factor otherwise CsPbI_3 would exist as a perovskite at room temperature. In addition to the tolerance factor, the size of the halide also plays a role in the overall stability of the structure with larger halides contributing to a less stable structure. Further investigation is needed to better understand why the larger halide ion destabilizes the perovskite structure when tolerance factor suggests perovskite formation.

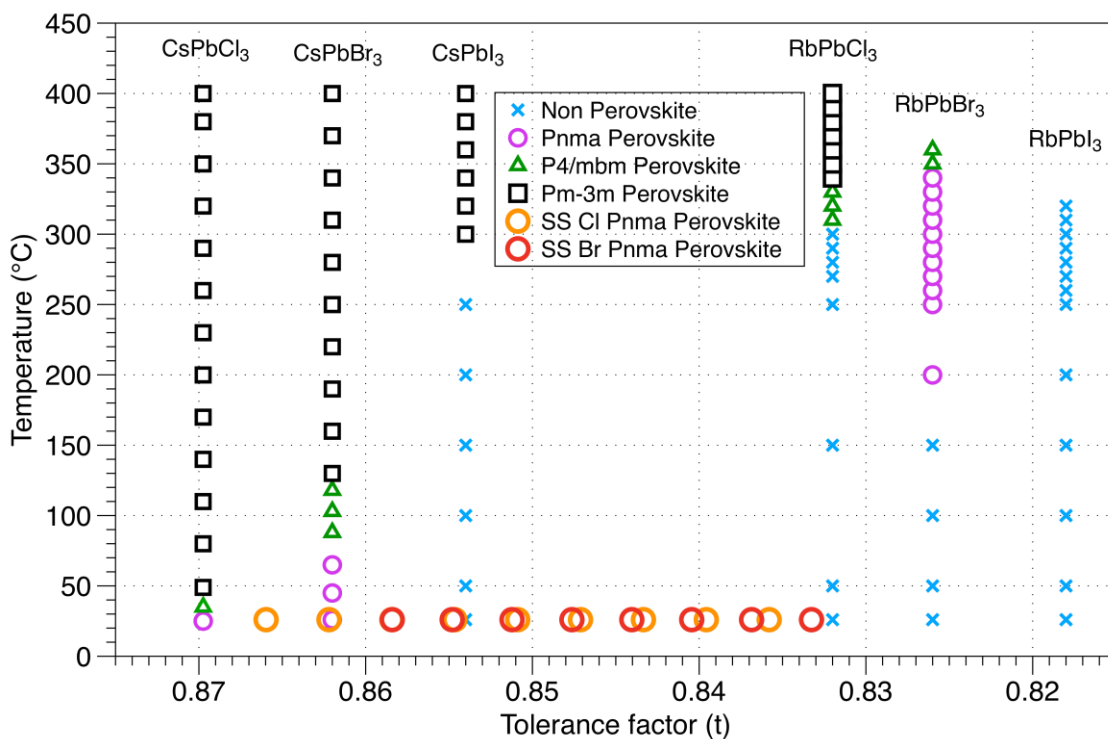


Figure 3.18: Temperature vs. Tolerance factor for compounds CsPbX_3 and RbPbX_3 ($\text{X}=\text{Cl}^-$, Br^- , Γ). Markers were added for all of the room temperature perovskites formed from solid solutions of Cl^- and Br^- . Last two points in the Br^- solid solution series ($x = 0.7$ and 0.8) are unstable and only exist in ambient conditions for about a minute.

While the magnitude of band gap tuning was quite small for the solid solutions (~0.17 eV for each halide), it does not come as much of a surprise given the small change in the Pb–X–Pb bond angles as Rb⁺ was incrementally doped into the structure. The largest change of the compound's band gap came as a result of changing the X-site halide. In order to gain larger control over the band gap in these compounds, one could employ A-site and X-site substitution to move almost anywhere in the 2.18 - 3.20 eV region.

Variable temperature experiments for RbPbCl₃ and RbPbBr₃ proved the existence of high temperature perovskite phases. Through creating solid solutions by incorporating Rb⁺ into the CsPbX₃ (X= Cl⁻ and Br⁻) structure, we were able to successfully stabilize room temperature perovskites at lower tolerance factors. XRD and refinement of the powder patterns confirmed that Rb⁺ was incorporating properly into the perovskite structure. Commenting on the stability of the Rb_(x)Cs_(1-x)PbX₃ solid solutions, Rb⁺ was able to be incorporated up to a concentration of x= 0.9 for Cl⁻, and x= 0.6 for Br⁻. Past these concentrations the perovskite structure was unable to be stabilized at room temperature.

Through the experiments conducted herein, the lower limit of perovskite formation in the lead halide perovskite systems was elucidated as well as the degree of octahedral distortion with A-site substitution. More clearly evidenced in the last section in Table 3.4, ambient condition stabilized perovskites will not form below a tolerance factor of 0.84. If kept in a completely inert atmosphere with no moisture these structures may be stabilized to a slightly lower tolerance factor before ceasing to exist anywhere below (t) = 0.832.

Bibliography

- (1) Howard, C. J.; Stokes, H. T. Group-Theoretical Analysis of Octahedral Tilting in Perovskites. **1998**.
- (2) Choi, H.; Jeong, J.; Kim, H. B.; Kim, S.; Walker, B.; Kim, G. H.; Kim, J. Y. Cesium-Doped Methylammonium Lead Iodide Perovskite Light Absorber for Hybrid Solar Cells. *Nano Energy* **2014**, 7, 80–85.
- (3) Stoumpos, C. C. et al. Crystal Growth of the Perovskite Semiconductor CsPbBr₃: A New Material for High-Energy Radiation Detection. *Cryst. Growth Des.* **2013**, 13 (7), 2722–2727.
- (4) Glazer, a. M. The Classification of Tilted Octahedra in Perovskites. *Acta Crystallogr. Sect. B Struct. Crystallogr. Cryst. Chem.* **1972**, 28 (11), 3384–3392.
- (5) Mizoguchi, H.; Eng, H. W.; Woodward, P. M. Probing the Electronic Structures of Ternary Perovskite and Pyrochlore Oxides Containing Sn⁴⁺ or Sb⁵⁺. *Inorg. Chem.* **2004**, 43 (5), 1667–1680.
- (6) Mitchell, R. *Perovskites: Modern and Ancient*; Almaz Press, Thunder Bay, **2002**.
- (7) Cheary, R. W.; Coelho, A. Fundamental Parameters Approach to X-Ray Line-Profile Fitting. *J. Appl. Crystallogr.* **1992**, 25 (pt 2), 109–121.
- (8) Shannon, R. D. Revised Effective Ionic Radii and Systematic Studies of Interatomic Distances in Halides and Chalcogenides. *Acta Crystallographica Section A* **1976**, pp 751–767.
- (9) Randall, C. a.; Bhalla, a. S.; Shrout, T. R.; Cross, L. E. Classification and

- Consequences of Complex Lead Perovskite Ferroelectrics with Regard to B-Site Cation Order. *J. Mater. Res.* **1990**, *5* (04), 829–834.
- (10) Woodward, P. M. Octahedral Tilting in Perovskites. II. Structure Stabilizing Forces. *Acta Crystallogr. Sect. B Struct. Sci.* **1997**, *53* (1), 44–66.
- (11) Lufaso, M. W.; Woodward, P. M. Research Papers Prediction of the Crystal Structures of Perovskites Using the Software Program SPuDS Research Papers. **2001**, 725–738.
- (12) Trots, D. M.; Myagkota, S. V. High-Temperature Structural Evolution of Caesium and Rubidium Triiodoplumbates. *J. Phys. Chem. Solids* **2008**, *69* (10), 2520–2526.
- (13) Moller, C. K. Crystal Structure and Photoconductivity of Caesium Plumbohalides. *Nature*. **1958**, p 1436.
- (14) Nitsch, K.; Dusek, M.; Nikl, M.; Polak, K.; Rodova, M. Ternary Alkali Lead Chlorides: Crystal Growth, Crystal Structure, Absorption and Emission Properties. *Cryst. Growth Charact.* **1995**, *30*, 1–22.
- (15) Hirotsu, S. Experimental Studies of Structural Phase Transitions in CsPbCl₃. *Journal of the Physical Society of Japan*. **1971**, pp 552–560.
- (16) Baikie, T.; Fang, Y.; Kadro, J. M.; Schreyer, M.; Wei, F.; Mhaisalkar, S. G.; Gratzel, M.; White, T. J. Synthesis and Crystal Chemistry of the Hybrid Perovskite (CH₃NH₃)PbI₃ for Solid-State Sensitised Solar Cell Applications. *J. Mater. Chem. A* **2013**, *1* (18), 5628.
- (17) Monzel, H.; Schramm, M.; Sto, K.; Beck, È. H. P. Zur Neuuntersuchung Des Phasendiagramms RbCl / PbCl₂ Redetermination of the Phase Diagram RbCl / PbCl₂. **2000**, 0–3.
- (18) Powell, H. M. The VaZency Angle of Bivalent Lead,. **1893**.
- (19) Young, R. A. *The Rietveld Method*; Oxford University Press, **1993**.
- (20) Barnes, P. W.; Lufaso, M. W.; Woodward, P. M. Structure Determination of

- A₂M₃+TaO₆ and A₂M₃+NbO₆ Ordered Perovskites: Octahedral Tilting and Pseudosymmetry. *Acta Crystallogr. Sect. B Struct. Sci.* **2006**, *62* (3), 384–396.
- (21) Abakumov, a. M.; Shpanchenko, R. V; Antipov, E. V. Zeitschrift für Anorganische Und Allgemeine Chemie Synthesis and Structure of the Double Oxide Pb₆Re₆O₁₉. *Zeitschrift für Anorg. und Allg. Chemie* **1998**, *624*, 750–753.
- (22) Ras, F. G.; Ijdo, D. J. W.; Verschoor, G. C. Ammonium Dilead Chloride. *Acta Crystallogr. Sect. B Struct. Crystallogr. Cryst. Chem.* **1977**, *33* (1), 259–260.
- (23) Becker, D.; Beck, H. P. High Pressure Study of NH₄Pb₂Br₅ Type Compounds. I Structural Parameters and Their Evolution under High Pressure. *Zeitschrift für Anorg. und Allg. Chemie* **2004**, *630* (12), 1924–1932.
- (24) Rodová, M.; Brožek, J. Phase Transitions in Ternary Caesium Lead Bromide. *J. Therm. Anal. ...* **2003**, *71* (62), 667–673.
- (25) Rodová, M.; Brožek, J. Phase Transitions in Ternary Caesium Lead Bromide. *J. Therm. Anal. ...* **2003**, *71* (62), 667–673.
- (26) Yin, W.-J.; Yang, J.-H.; Kang, J.; Yan, Y.; Wei, S.-H. Halide Perovskite Materials for Solar Cells: A Theoretical Review. *J. Mater. Chem. A* **2014**, *00*, 1–17.
- (27) Myagkota, S. .; Voloshinovskii, a. .; Stefanskii, I. .; Mikhailik, M. .; Pashuk, I. . Reflection and Emission Properties of Lead-Based Perovskite-like Crystals. *Radiat. Meas.* **1998**, *29* (3-4), 273–277.
- (28) Tauc, J.; Grigorovic, R.; Vancu, a. Optical Properties and Electronic Structure of Amorphous Germanium. *Phys. Status Solidi* **1966**, *15* (2), 627–637.
- (29) Smith, a. J.; Welch, a. J. E. Some Mixed Metal Oxides of Perovskite Structure. *Acta Crystallogr.* **1960**, *13* (8), 653–656.
- (30) Green, M. a; Prassides, K.; Day, P.; Neumann, D. a. Structure of the N₅2 and N₅ Member of the Ruddlesden-Popper. *2000*, *2*, 35–41.

- (31) Vegas, a. The ASnO₃ (A=Ca, Sr) Perovskites. **1986**.
- (32) Jang, D. M.; Park, K.; Kim, D. H.; Park, J.; Shojaei, F.; Kang, H. S.; Ahn, J.-P.; Lee, J. W.; Song, J. K. Reversible Halide Exchange Reaction of Organometal Trihalide Perovskite Colloidal Nanocrystals for Full-Range Band Gap Tuning. *Nano Lett.* **2015**, 150710151810003.
- (33) Kulkarni, S. a.; Baikie, T.; Boix, P. P.; Yantara, N.; Mathews, N.; Mhaisalkar, S. Band-Gap Tuning of Lead Halide Perovskites Using a Sequential Deposition Process. *J. Mater. Chem. A* **2014**, 2 (24), 9221.